

Spectroscopic Signatures of Multiple Populations in Globular Clusters

By

James T Banister



A thesis submitted in partial fulfilment
for the requirements for the degree of

MSc (by Research)

at the University of Central Lancashire
& The Jeremiah Horrocks Institute

September 2020

STUDENT DECLARATION FORM

Type of Award MSc (By Research)

School Natural Sciences

*Sections marked * delete as appropriate*

1. Concurrent registration for two or more academic awards

Either *I declare that while registered as a candidate for the research degree, I have not been a registered candidate or enrolled student for another award of the University or other academic or professional institution

2. Material submitted for another award

Either *I declare that no material contained in the thesis has been used in any other submission for an academic award and is solely my own work

3. Collaboration

Where a candidate's research programme is part of a collaborative project, the thesis must indicate in addition clearly the candidate's individual contribution and the extent of the collaboration. Please state below:

4. Use of a Proof-reader

or *No proof-reading service was used in the compilation of this thesis.

Signature of Candidate 

Print name: James Thomas Banister

Spectroscopic Signatures of Multiple Populations in Globular Clusters

James T Banister

Abstract

This thesis presents a study of the integrated light spectra of local globular clusters, looking for chemical enhancements which could be the signatures of multiple populations. Using data from the WiFeS Atlas of Galactic Globular cluster Spectra: the spectra are fit to SSP models via penalised pixel fitting techniques looking for poor fitting regions which could signify chemical enhancements. Line indices of key regions are measured, and nitrogen enhancements are found in the CN region $\sim 4100 \text{ \AA}$ for almost all globular clusters with evidence for elemental abundance variations in other regions. Also, nitrogen enhancement is found in other compact stellar systems (UCDs and some cEs) and the inner light of high mass galaxies, suggesting a possible relation between high stellar density and nitrogen enhancement.

September, 2020

Supervisors: Mark Norris, Ph.D. and Joanne Pledger, Ph.D.

University of Central Lancashire

Jeremiah Horrocks Institute

Contents

Declaration	i
List of Figures	vii
List of Tables	ix
1 Introduction	1
1.1 Globular Clusters	1
1.2 Multiple Populations	2
1.3 Integrated Light Observation	3
1.4 A Brief Preamble to Available Globular Cluster Data	4
2 Theory	5
2.1 Globular Clusters	5
2.1.1 Milky Way Globular Clusters & Halo Enrichment Via Tidal Effects	7
2.1.2 Magellanic Cloud and Fornax DSG Globular Clusters	9
2.1.3 Extragalactic Globular Clusters	12
2.2 Multiple Populations	13
2.2.1 Chemical Abundance Variations & Correlations	15
2.2.2 Single Population Globular Clusters	19
2.3 Formation Theories of Multiple Populations	20
2.3.1 AGB Stars	21
2.3.2 Fast Rotating Massive Stars (FRMS)	22
2.3.3 Binary Interactions	23
2.3.4 Black Hole Accretion Disk Nucleosynthesis	24
3 Data & Data Reduction	26
3.1 WAGGS	26
3.1.1 Globular Cluster Selection	27

3.1.2	Observations	28
3.1.3	Equipment & Data	31
3.2	Reduction	32
3.2.1	Redshift	33
3.2.2	Combination	36
3.2.3	Error Spectra	38
3.2.4	Omitted Globular Clusters	39
3.3	Additional Data	39
3.3.1	Galaxies -Trager	40
3.3.2	M31 GCs -Schiavon	40
3.3.3	M87 GCs and UCDS	40
3.3.4	MODS Objects	41
3.3.5	SDSS Galaxy Bins	41
4	Fitting to SSP Models	43
4.1	pPXF	43
4.2	Single Stellar Population Models	44
4.2.1	MILES SSPs	44
4.2.2	Conroy	46
4.3	Fitting Procedure	46
4.3.1	Example Fitting Procedure	48
4.3.2	Regions of interest	48
4.3.3	Fit Comparison	50
4.3.4	Error calculations	50
5	Measuring Indices	52
5.1	Line Index Systems	52
5.1.1	LICK/IDS & LIS	52
5.2	Measurements	54
5.3	Offsets from Literature	54
5.3.1	Current Published Works	54
5.3.2	Offset Calculation	55
5.3.3	Thomas SSP Models	57
6	Signatures of Multiple Populations	59
6.1	Single Stellar Population Fitting	59
6.1.1	Other Poor Fitting Regions	61

6.2	Line Index systems	64
6.2.1	Alpha Insensitive Metallicity Index	64
6.2.2	Globular Clusters	64
6.2.3	Extragalactic Stellar Systems	67
6.2.4	Uncertainty Calculations	70
7	Conclusions and Discussion of Future Work	73
7.1	Evidence of Multiple Populations	73
7.1.1	N enhancement in Dense Stellar Systems	75
7.2	Age Estimation Problem	76
7.3	Conclusion	78
7.4	Future Research	79
	Bibliography	81
8	APPENDIX	86

Acknowledgements

Firstly I would like to thank Dr Mark Norris for continued support and advice on the research, without which I would undoubtedly not be here, and thanks for providing additional stellar system data and for prompt replies to any question regardless of time or day. I would also like to thank Dr Chris Usher for providing extra information on the WAGGS survey and data set. Thanks to Thomas Davison and David Glass for advice on the proper use of pPXF and thanks again to Thomas Davison for providing binned SDSS galaxy spectra. For all of the support from the people who shared an office with me before Covid-19 forced us out, I would like to give my thanks. I would also like to thank Covid-19 for giving me no choice but to stay inside these last few months giving me more time to work on the thesis.

List of Figures

2.1	The CMD of NGC 2808	7
2.2	Position of the Sagittarius Dwarf Galaxy relative to the Milky Way	8
2.3	Age metallicity plot of globular clusters in the Magellanic Clouds	10
2.4	The positions of globular clusters in the Fornax dwarf spheroidal galaxy	11
2.5	The CMD of NGC 5139 showing multiple main sequence turn off points	14
2.6	The first detection of multiple populations in globular clusters	15
2.7	The elemental correlations present in globular clusters due to multiple populations, here plotted over photometric data of NGC 6752	16
2.8	A plot of the split main sequence, multiple turn off points of NGC 5139 with isochrones plotted over the top	18
2.9	A plot showing how the split main sequence of a globular cluster is detected	20
3.1	[Fe/H] against Age for the globular clusters in the WAGGS sample	26
3.2	Field-of-view of the WAGGS observations for 3 GCs	30
3.3	The fraction of the V-band luminosity in the WiFeS field-of-view compared to the full v-band luminosity of the GC	31
3.4	The grating efficiencies of the WiFeS gratings at the most efficient angle of incidence	32
3.5	The redshift adjusted B7000 grating spectra for the majority of the globular clusters separated according to [Fe/H] into 8 bins	33
3.6	A diagram of the spectra of NGC 2808 during the redshift adjusting and regridding process	35
3.7	A diagram of the grating combination process used for the WAGGS spectra	37
3.8	A full WAGGS spectrum with associated 1σ errors for NGC 5694	38
3.9	The Voronoi diagram describing the bins of the SDSS galaxy spectra	42
4.1	An example of the new linearly combined SSP models	45
4.2	pPXF fit and mass fraction plot of NGC 104 with no regions omitted	48
4.3	pPXF fit and mass fraction plot of NGC 104 with omitted regions	49

4.4	A comparison between the mass fraction plots in literature and those found in this project for NGC 6715	51
5.1	Example of Lick indices, CN_1 and CN_2 over the spectra of NGC 104	53
5.2	The Offsets between WAGGS line indices and those of literature	56
6.1	pPXF fit of NGC 104 with omitted regions	60
6.2	Conroy models showing where C and N effect a stellar spectrum between 3800 and 4600 Å	60
6.3	pPXF fit and mass fraction plot of NGC 104 with omitted regions	62
6.4	Spectral indices plot of CN_1 against metallicity showing WAGGS GCs and SSP models with a colour bar of age for the WAGGS globular clusters	65
6.5	Spectral indices plot of CN_2 against metallicity showing WAGGS and M31 GCs and SSP models with a colour bar of age for the WAGGS globular clusters	66
6.6	Spectral indices plot of CN_1 against metallicity showing WAGGS and M31 GCs and enhanced SSP models with a colour bar of age for the WAGGS globular clusters	67
6.7	Spectral indices plot of CN_1 against metallicity showing GCs, UCDs, cEs and enhanced SSP models with a colour bar of age for the globular clusters	68
6.8	Spectral indices plot of CN_1 against metallicity showing GCs, UCDs, enhanced SSP models, SDSS binned galaxies and galactic core spectral indices, with a colour bar of age for the globular clusters	70
6.9	Spectral indices plot of CN_1 against metallicity showing GCs, UCDs, cEs, enhanced SSP models and SDSS binned galaxies with a colour bar of mass in the galaxies	72
7.1	Spectral indices plot of CN_1 against metallicity showing GCs, UCDs, enhanced SSP models and SDSS binned galaxies with a colour bar of stellar density in the galaxies	76

List of Tables

3.1 Signal to noise ratios of the WAGGS data.	29
5.1 Table of Indices Offsets.	57
8.1 Table of Omitted Regions.	86
8.2 Table of the globular clusters used in this project.	86
8.3 Table of LICK Indices.	89

1|Introduction

Globular clusters (GCs) were long thought to be single stellar populations i.e. one population of chemically identical stars of the same age (e.g. Peebles and Dicke [1968](#)). Recently, through photometric and spectroscopic studies of the constituent stars of globular clusters, spread over the last 50 years (an early example being Osborn [1971](#)), GCs have been observed to contain secondary chemically enriched populations of stars. These star-to-star abundance variations in the GCs are known as multiple populations (MPs), although the name may prove to be misleading as it is currently unknown if they are the result of a secondary round of star formation or not.

The standard procedure for identifying multiple populations in globular clusters is photometrically through colour-magnitude diagrams (CMDs) for wavelengths dominated by elements commonly known to be enhanced in a secondary population. This however does not work for GCs at greater distance because the method requires the measurement of individual resolved stars. In this thesis, the integrated light of GCs is studied looking for discrepancies between globular cluster spectra and spectra predicted by theoretically true single stellar population models in order to determine if it is feasible too spectroscopically detect MPs in unresolved GCs.

1.1 Globular Clusters

Globular clusters are densely packed stellar systems containing thousands to millions of constituent stars believed to be formed in a single star formation period from the same interstellar gas cloud. Almost all Milky Way (MW) globular clusters are incredibly old (the oldest often being in excess of 12.5 Gyr e.g. Forbes et al. [2018](#)). The oldest clusters formed before the end of reionization (Forbes et al. [2018](#)), and as such are key probes into

understanding the early universe and galaxy formation. The Milky Way is known to have a dominant population of very old metal poor GCs in the galactic halo as well as a relatively metal rich population in the galactic bulge (Forbes and Bridges 2010). Globular clusters in the Milky Way’s companion dwarf galaxies, the Small and Large Magellanic Clouds (SMC & LMC), are often much younger with some GCs potentially being as young as 30 Myrs old i.e. the SMC globular cluster NGC 330 (Sirianni et al. 2002).

Because GCs in general formed when the universe was still very young, almost all MW globular clusters are relatively metal poor (compared to solar levels) containing mostly population II stars. They were formed from clouds primarily consisting of hydrogen and helium with very little metal contamination as significant quantities of heavier metals had not been formed yet. The theory that all GCs are examples of single stellar populations was initially thought to be well founded. Globular clusters are much smaller than galaxies and dwarf galaxies and it is predicted that stars will continue to form in the system until one massive star uses up all of its fuel in nuclear fusion, completing its life cycle, and goes supernovae (SN) becoming a white dwarf, neutron star or a black hole. The resulting blast of the supernovae provides a shock wave which is strong enough to disrupt the gas and dust in the system. For all but the most massive globular clusters (i.e. ω Cen), SN shock waves eject all the gas and dust remaining from the initial bout of star formation out of the system putting an end to any further star formation (Tenorio-Tagle et al. 2015). Supernovae are usually one of the leading causes of chemical enrichment to a stellar system (Zijlstra 2004 & Wise et al. 2012). In the case of globular clusters though, they are too small for the system’s gravity to contain the ejecta within the cluster (Dopita and Smith 1986). In the largest globular clusters Tenorio-Tagle et al. (2015) state that only ejecta from “well centred” SNe would be retained, which could cause a population of stars to show “Fe contamination” in secondary populations if the ejecta evolves into a high-density medium mixing with any remaining primordial gas. But for most globular clusters, no secondary enrichment of stars from accretion can occur further leading to the theory that GC should be single stellar populations. So therefore the separate populations of stars with light element variations that are seen must come from other mechanisms (see Section 2.3).

1.2 Multiple Populations

The definition of multiple populations in globular clusters, as defined by Bastian and Lardo (2018), is the presence of star-to-star variations in chemical abundances, not expected from

stellar evolutionary processes. The star-to-star variations are called secondary populations (or secondary generations) due to there being commonality between the chemically enriched stars indicating they are all part of the same stellar group, separate to that of the “main” stellar group (first population/generation) of the cluster. Multiple populations are commonly detected via space and ground based spectroscopy and photometry of individual stars. Advances in observational techniques since the discovery of these secondary populations, and almost half a century of research (starting with Osborn [1971](#)) has led to many theories as to why multiple populations exist which can provide testable predictions (see e.g. Bastian and Lardo [2018](#)). An overview of the many theories for the existence of multiple populations is given in Section [2.3](#). However these theories all have their flaws and as such, the origin of the multiple populations seen in GCs is one of the major unsolved problems in compact stellar system research.

Almost all galactic GCs are observed to show at least some abundance variation in Helium, Nitrogen, Sodium, Carbon and Oxygen. The individual abundance variation ratios are different for each globular cluster, and many are enriched/depleted in other elements causing the secondary (or even tertiary and further) populations to be distinctly unique. More than this there are many correlations between certain chemical enrichments such as a the Na-O anti correlation which is discussed in a greater detail in Section [2.2.1](#). The presence of MPs in integrated light may be the key to studying the phenomenon in extragalactic globular clusters. But, satisfactorily detailed integrated light spectroscopic data and stellar population models are needed to give accurate predictions and recognise the signatures given by extragalactic clusters.

1.3 Integrated Light Observation

The goal in this project was to try and identify the signatures of secondary populations in integrated light where before it has generally only ever been achieved using individual star-to-star comparison. Star-to-star comparison, as stated earlier however, does not work for non-local group clusters because the constituent stars needed for photometric star-to-star comparison are not individually resolvable. Integrated light, examined spectroscopically, could overcome this problem. Integrated light takes the full light of a group of objects (i.e. stars in a cluster) and combines it all into a single light source where the effects of each star contributes to the total spectrum based on its luminosity. The goal of this project was to look at the integrated light spectrum of local globular clusters with the aim of attempting

to define how integrated light spectra behaves for GCs with multiple populations. The developed techniques can then be used to probe whether extragalactic GCs display the same behaviour i.e. multiple populations, age, metallicity and alpha abundances.

1.4 A Brief Preamble to Available Globular Cluster Data

Not until the last decade has there been significant samples of high quality integrated light spectra for galactic globular clusters from which predictions for the effects of MPs could be reliably measured. Prior to 2016 the best existing spectral library was by Schiavon et al. [2005]. This only covered a range of $\sim 3350 - 6430\text{\AA}$ so did not cover key regions for detecting metallicity and making initial mass function (IMF) studies such as the Ca triplet at $8498 - 8662\text{\AA}$ and Na doublet at $\sim 8190\text{\AA}$. The 2005 library also had a relatively low spectral resolution of $\text{FWHM} = 3.0\text{\AA}$ compared to more recent studies. Kim et al. [2016] (“Kim” hereafter) used a combination of the line index measurements from Schiavon et al. [2005], another study (Puzia et al. [2002] which had a larger spectral range of $\sim 3400 - 7300\text{\AA}$ but a lower spectral resolution of $\text{FWHM} \approx 6.7\text{\AA}$) and data from their own study to create a new library of indices measurements in both the older LICK/IDS (Gorgas et al. [1993]; Worthey et al. [1994]; Worthey and Ottaviani [1997]) and a newer LIS index system (Vazdekis et al. [2010]). Kim’s own data, while having a higher resolution than both previous studies (2.0\AA), had a low signal to noise level compared to that of the study from which data for this project is primarily used.

The WiFeS Atlas of Galactic Globular cluster Spectra (WAGGS) (Usher et al. [2017]), which is covered comprehensively in Section [3.1], has a much higher resolution ($\text{FWHM} = 0.8\text{\AA}$) and gives good signal to noise of $\sim 600\text{\AA}^{-1}$ (which is the mean value from Table 2 of Usher et al. [2017], see Table [3.1] for more on the S/N for individual gratings) for a larger selection of globular clusters than those in the Kim library. For that reason and for the reasons stated in Section [3.1], WAGGS is used in this project as the primary source of galactic globular cluster data and offers reliable detailed spectra compared to that of previous integrated spectra studies. The full table of globular clusters from the WAGGS survey used in this project are available in the Appendix: Table [8.2]. Much of the data in this table is taken from the supplementary files of Usher et al. [2019] or otherwise cited where necessary.

2|Theory

In order to study the effects of multiple populations in globular clusters (local and extragalactic), one must first understand globular clusters: how they formed and evolved, and also know the key signatures of which multiple populations are defined.

2.1 Globular Clusters

The first globular cluster to be discovered was M22 (NGC 6656) in 1665, it was not known at the time that it was a globular cluster and in fact the term globular cluster would not be coined for another 124 years.

The discovery of M22 was made by an amateur German astronomer, Abraham Ihle, and was later officially published by Kirch (1681). But due to the technological abilities of telescopes at the time, individual stars were not resolved in this first discovery. Because of this, it was not known to be a star cluster. The constituent stars were not officially resolved in globular clusters until 1764 by Charles Messier who published a library of nebulae and star clusters outlining his discovery in 1771 (Messier 1771). The name “globular cluster” however was not used to describe them until 1789 when William Herschel coined the term in the “Catalogue of Second Thousand New Nebulae and Clusters of Stars” (Herschel 1789), in this same catalogue he more than doubled the list of known globular clusters at the time (from 34 to 70). Since then, steadily more and more globular clusters have been discovered and the current total of discovered Milky Way globular clusters is around 164 according to the database of Milky Way GCs (Kronberg and Frommert 2019) although more GCs are still being discovered (e.g. Garro et al. 2020). Surdin (1994) states that there are an estimated 170 ± 8 globular clusters in the Galaxy, they suggested that many have horizontal branches with a magnitude dimmer than $V=25$. So the undiscovered GCs are most likely too dim and

their positions in the Galaxy cause them to be obscured by gas and dust clouds. Modern techniques, such as those presented in Garro et al. (2020) (using infrared data), are now showing that objects that were previously obscured to us (by gas or dust) or were too dim are now observable.

Historically, globular clusters were used for many studies of the formation of our Galaxy. None could have more of an effect on the understanding of our solar system's place in the Galaxy than a discovery made in 1918 by Harlow Shapley. By measuring the positions of globular clusters in our Galaxy, he concluded that the Sun was not at the centre of the Milky Way. But more than that he discovered that the Sun was not even near it (Shapley 1918). In this same work, he discovered that unlike other stellar systems in the Galaxy, globular clusters did not concentrate near the galactic plane but did the opposite. He noted that the known globular clusters formed a 'halo' around the Galaxy. It was from the dimensions of this 'halo' of globular clusters that he concluded that the earth was not at the centre of the Galaxy. The discovery of this globular cluster halo showed that study of globular clusters would play a key part in probing the formation and evolution of the Milky Way and, perhaps even more interestingly, other galaxies.

Globular clusters have long been known to be very old stellar systems. The most common way of measuring a cluster's age is by fitting an isochrone model to a colour-magnitude diagram (CMD). The typical rule for age calculation is that the main sequence turnoff point (MSTO) defines the age of the globular cluster. According to general understanding, stars within a cluster all formed in the same star-formation period making them the same age. CMDs are therefore a good tool for showing the age and other properties of a cluster, as this way you can do star-to-star comparison and find overall trends for the full cluster. Where the stars in a cluster turn off their main sequence (MS) and the proportion of post MS stars to active MS stars defines the age of the cluster. Fitting to isochrones for different ages can provide highly accurate measurements of age. In Figure 2.1 of NGC 2808 the MSTO is clearly visible and there is a large proportion of post-MS stars, indicating a very old age. The literature age for NGC 2808 is calculated to be 11.5 Gyr (Milone et al. 2014) which confirms this age estimation.

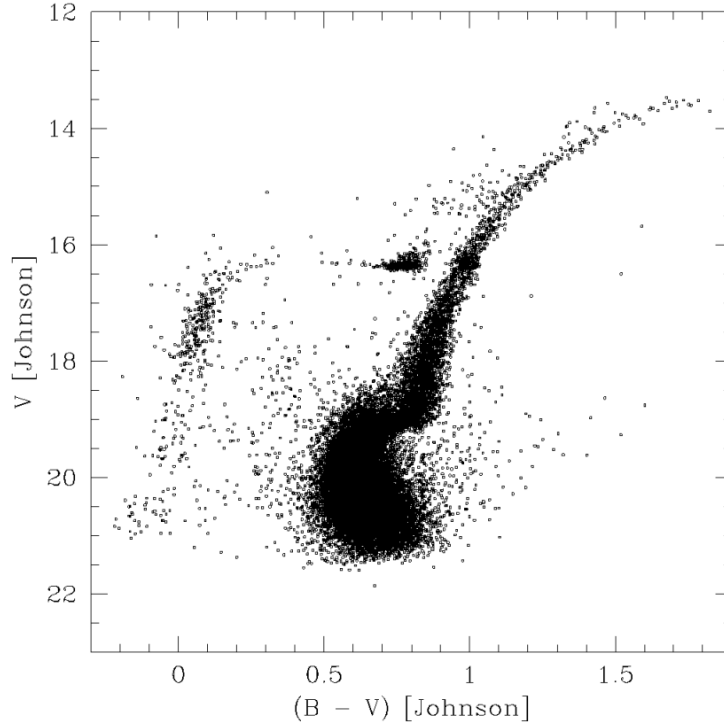


Figure 2.1: The CMD of 27,286 stars in NGC 2808. Prominent are the MSTO with some blue stragglers. A dominant red giant branch (RGB) followed by a few asymptotic giant branch (AGB) stars and the Horizontal branch (Figure 1 of Sosin et al. 1997).

2.1.1 Milky Way Globular Clusters & Halo Enrichment Via Tidal Effects

According to Λ cold dark matter universe (Λ CDM) theory, a large fraction of the halo in Milky Way like galaxies is thought to be made up of material and objects from accreted smaller dwarf galaxies (Abadi, Navarro and Steinmetz 2006; Font et al. 2006). For the case of the Milky Way, we know dwarf galaxy accretion is a contributor to the galactic halo as our Galaxy is currently in the process of subsuming the Sagittarius Dwarf Elliptical Galaxy (SagDEG) (Lynden-Bell and Lynden-Bell 1995; Newberg et al. 2002; Majewski et al. 2003) and many globular clusters have been suggested to be originally from SagDEG (Bellazzini et al. 2003).

Figure 2.2 shows how the core of SagDEG has been tidally stretched into arc-like arms by the gravitational force of the Milky Way. These tidal forces rip apart smaller galaxies over several orbits, until the dwarf galaxy is completely consumed by the parent galaxy. In the process of subsuming a smaller galaxy the larger galaxy, will also take the globular

clusters from that galaxy. This indicates that many globular clusters that we today consider to be part of the Milky Way GC system may have been accreted from these smaller dwarf galaxies. While smaller galaxies will be completely disrupted by tidal stripping, globular clusters survive the effects due to their immense density (Forbes and Bridges 2010) keeping the constituent stars gravitationally bound together.

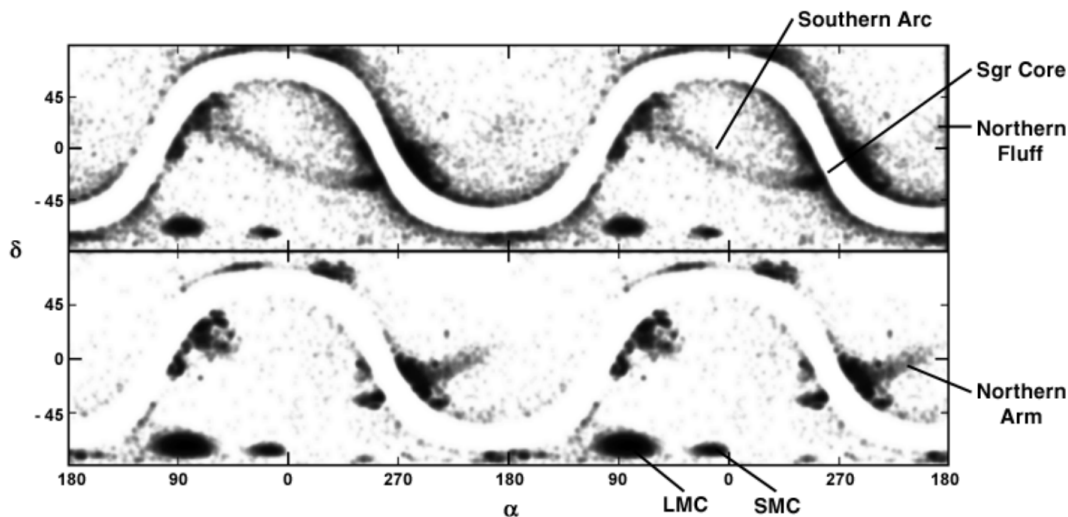


Figure 2.2: This plot is Figure 3 of Majewski et al. (2003). They state these are two plots: one emphasising the northern arc of the Sagittarius Dwarf Galaxy the other showing the southern. They showed two cycles of the sky demonstrating the continuity of the features.

It is known via studies of the age-metallicity relation (AMR) of globular clusters (Forbes and Bridges 2010) that in more than one instance the Milky Way has disrupted a dwarf galaxy. SagDEG and the Canis Major Dwarf Galaxy (CMa Dwarf) are attributed to being the major contributors of globular clusters. Although, it has been recently suggested that the CMa Dwarf galaxy is actually a warp of the MW disc, not an accreted dwarf galaxy (e.g. Carballo-Bello et al. 2020). There is evidence for the existence of globular clusters from other dwarf galaxies present in the halo. Estimates suggest that the Milky Way has undergone around 15 merger events with smaller dwarf galaxies (Kruijssen et al. 2020) with the suggested value of non Milky Way originating globular clusters to be between 24 and 47 (Forbes and Bridges 2010) with the rest being *in-situ* globular clusters formed in the Milky Way. Therefore it is reasonable to expect that some if not many of the globular clusters used in this project are *ex-situ* globular clusters. Fortunately, this situation is preferable as it will give a broader sample of globular clusters which can be analysed.

2.1.2 Magellanic Cloud and Fornax DSG Globular Clusters

As well as Milky Way globular clusters, this thesis uses data from both the Magellanic Clouds and the Fornax Dwarf Spheroidal Galaxy (Fornax dSph). This data (as well as the Milky Way GC data) comes from the Usher et al. (2017) (see Section 3.1). The use of non MW globular clusters both increases the sample size and gives a broader representation of globular clusters that were not formed in the Milky Way. This is important as the method used in this project could be used to assess extragalactic GCs which may have different characteristics to MW globular clusters.

The Milky Way has several satellite galaxies. The most prominent of which are the two Magellanic clouds. The Small and Large Magellanic Clouds (SMC and LMC respectively) are both located in the southern galactic hemisphere and are the two most massive and, coincidentally, closest companion dwarf galaxies (the SMC being 62.1 ± 1.9 kpc, (Graczyk et al. 2013) and the LMC being 49.59 ± 0.09 [statistical] ± 0.54 [systematic] kpc, (Pietrzyński et al. 2019)). Their positions are indicated in Figure 2.2

The Magellanic Clouds contain many star clusters. While both have some classically old and metal poor globular clusters, they also contain large populations of young and relatively metal rich GCs (Mackey 2009). There is a key difference between the the two dwarf galaxies though. While the Small Magellanic Cloud has clusters both old and young ($< 1 - 11$; Gyr, the youngest of which is NGC 330 at ~ 30 Myr Sirianni et al. 2002), there is a large gap between the ages of the clusters within the Large Magellanic Cloud as is shown in Figure 2.3 and in Table 8.2 (for data used in this project).

The Large Magellanic Cloud has globular clusters of ages ~ 13 Gyr (e.g. NGC 1916 with an age of ~ 12.9 Gyr; (Mackey and Gilmore 2003) and NGC 2019 with an age of ~ 12.5 Gyr; (Olsen et al. 1998)) and globular clusters of incredibly young ages such as NGC 2004 whose age is ~ 20 Myr (Niederhofer et al. 2015). There does not seem to be, however, any middle aged ($\sim 3 - 10$ Gyr) clusters (Mackey 2009). This “age gap” is shown as a clear gap between two groups of clusters in the upper left panel of Figure 2.3 (and in Figure 3.1 for the GCs used in this project). The reasons behind this are unknown since the star formation rate for the LMC is known to be non-zero during this time (e.g. Smecker-Hane et al. 2002 & Carrera et al. 2008). It has been suggested that the first tidal interactions between the LMC and SMC happened about 4 Gyr ago (Bekki et al. 2004) and subsequent repeated tidal interactions may have transferred many globular clusters from the LMC to the SMC in stellar mixing (Bekki et al. 2004) but it is unknown how the models put forward in Bekki

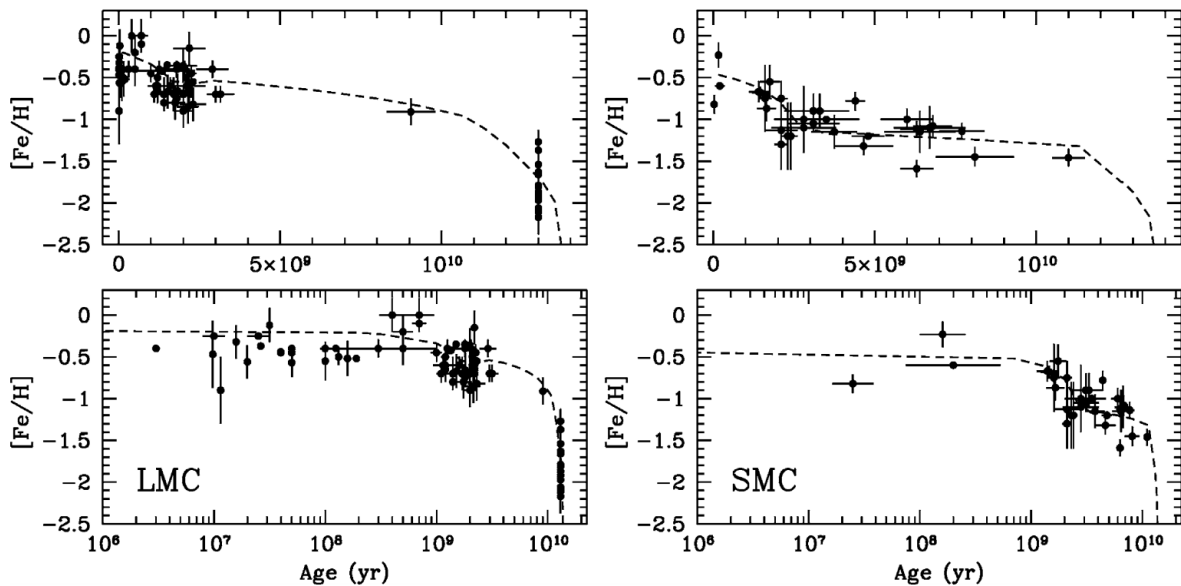


Figure 2.3: This plot is Figure 2 of Mackey (2009). It shows the ages against metallicity values for several clusters in the Small (right panels) and Large (left panels) Magellanic Clouds. The dashed lines are “chemical enrichment models by Pagel and Tautvaišienė (1998) for bursting star-formation histories.”

et al. (2004) agree with LMC and SMC proper motions, measured with the Hubble Space Telescope (HST). Růžička, Theis and Palouš (2009) suggest that “the dynamical evolution of the Magellanic System with the currently accepted total mass of the MW cannot be explained in the framework of pure tidal models”. So clearly the “age gap” is an unexplained phenomenon. A full summary of the globular cluster age gap is available at Mackey (2009), from which information for this section was taken.

Many globular clusters from the Magellanic clouds are used in this project (see Table 8.2). Their extreme age and metallicity range greatly increase the variation of parameters for the sample of globular clusters. The fact that these globular clusters developed in a completely different stellar environment to the Milky Way also leads to probes of galactic evolution in galaxies distinct to our own.

The Fornax Dwarf Spheroidal Galaxy was discovered in 1938 by Harlow Shapley (Shapley 1938). It is a dwarf spheroidal galaxy in the constellation of Fornax around 146 ± 9 kpc away (Karczmarek et al. 2017). There are 5 known globular clusters within the Fornax dSph which are all old and metal poor (Larsen, Brodie and Strader 2012). There is a supposed sixth cluster which has been under debate as to whether or not it is a true globular cluster (e.g. Wang et al. 2019).

Fornax 4 is more metal rich (by ~ 0.8 dex; Larsen, Brodie and Strader 2012) and is a few Gyr younger (de Boer and Fraser 2016) than its other globular cluster companions despite their similar masses. It is suggested that this globular cluster could have experienced a different formation than the other clusters in the system. It has been suggested in a very recent paper (published after the majority of work for this project was completed) that via photometric evidence and other “peculiarities characterising the system” (such as the location shown to be near the core in Figure 2.4), Fornax 4 could in fact be the nuclear star cluster for the Fornax dSph (Martocchia et al. 2020). They state a spectroscopic study for a large number of resolved member stars is needed to followup their assumption so that a more detailed understanding of the formation and early evolution of the cluster and Fornax dSph in general can be gathered. In this thesis Fornax 4 will still be treated as a globular cluster but this development is definitely a point of interest and more research could help spread further light on the topic. The globular clusters from Fornax dSph used in this project are Fornax 3, 4 and 5 and are shown in Table 8.2

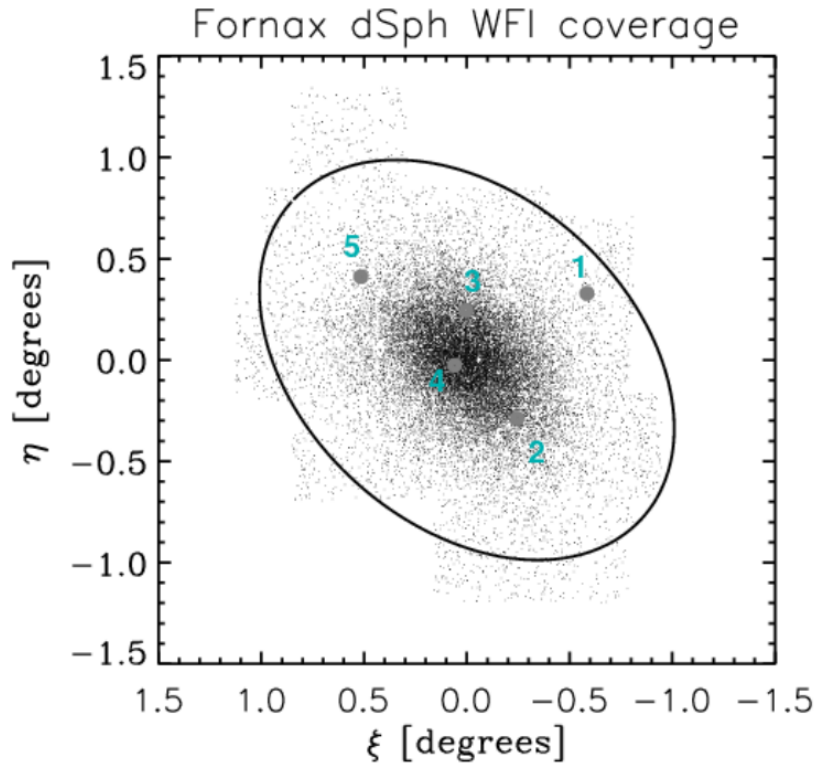


Figure 2.4: This plot is Figure 1 of Battaglia et al. (2006) (using the ESO Wide Field Imager (WFI)). It shows the locations of all 5 confirmed globular clusters within the Fornax Dwarf Spheroidal Galaxy.

2.1.3 Extragalactic Globular Clusters

Globular clusters have been observed in every type of galaxy across the full Hubble sequence of morphological types (Brodie and Strader 2006). It is safe to assume that globular clusters form in all galaxies and, given their great age, play a part in the formation and evolution of their host galaxy and potentially play a part in the enrichment of other galaxies due to tidal interactions (Forbes and Bridges 2010). As has been stated previously, it is hoped that the methods used in this project can be used to assess extragalactic GCs

Our closest neighbour galaxy Andromeda (M31) has comparable mass to our Galaxy (e.g. Evans and Wilkinson 2000 & Reid et al. 2009) although it has been suggested by Pillastrini (2009) that the Milky Way and M31 have a mass ratio of two to three implying a “massive predominance of M31”. The current best estimate of globular clusters in Andromeda is that the galaxy contains 441 GCs (Caldwell and Romanowsky 2016a). This is vastly more globular clusters than the Milky Way contains, so M31 is naturally a start for the study of extragalactic globular clusters.

As well as there being more of them, the globular clusters of M31 are generally more metal rich despite having similar ages to Milky Way globular clusters (Cezario et al. 2012). They display a ‘trimodal’ metallicity distribution, with a groups in the metallicity range $[\text{Fe}/\text{H}] \geq -0.4$ & ≈ -1 & ≤ -1.5 (Caldwell and Romanowsky 2016b) with the majority ($\sim 2/3$) belonging to more metal poor populations (Rich 2003). It has been known for a while that bimodality (or separation of metallicity distributions) among globular clusters is common in the most massive galaxies (Zepf and Ashman 1993). The radial distribution of the globular clusters show that the more metal rich population lies nearer the core while the metal poor globular clusters lie in the galactic halo (Caldwell and Romanowsky 2016b) which is a distribution similar to the globular clusters of our Galaxy (Burkert and Smith 1997). This distribution is strong evidence that globular clusters in both the Milky Way and M31 have similar formation and evolution paths so comparisons made between the two can be assumed to be reliable.

Many globular clusters in M31 contain stars resolvable to current observation techniques and technologies, so star-to-star comparison and photometry can be used. However, not all globular clusters have this, and when one observes galaxies at greater distances the constituent stars of their globular clusters are progressively less well resolved so the techniques used are not viable anymore. Thus for most extragalactic globular clusters integrated light is used to obtain information about them (because the light coming from them is automatically

integrated).

A section about extragalactic globular clusters is not complete without at least mentioning the SAGES (Study of the Astrophysics of Globular clusters in Extragalactic Systems) Legacy Unifying Globulars and Galaxies Survey (SLUGGS, Brodie et al. 2014). They observed a sample of 25 early type galaxies in the local universe and their globular cluster systems. The data from this survey has been used in a number of papers, notable for this thesis is the discovery of evidence that shows metallicity bimodality of globular clusters (Brodie et al. 2014) similar to the bimodality of globular cluster systems of the Milky Way and Andromeda. The observation of metallicity bimodality is significant as it is commonly assumed that major star formation epochs in a galaxy's past are accompanied by the formation of globular clusters. Thus the presence of bimodality suggests multiple events of galaxy formation for a galaxy. This is an interesting point but is, however, beyond the scope of this project.

Comparison of local globular clusters to extragalactic ones can help us understand their formation and to see if properties seen in Milky Way globular clusters, such as multiple populations, are also present.

2.2 Multiple Populations

Much of the information presented in this section was gathered from Bastian and Lardo (2018) (which is recommend to the interested reader). Bastian and Lardo have collated a full history and a substantial list of properties and theories for multiple stellar populations of globular clusters, from which a selection of relevant material is used in this thesis along with many other sources and more recent publications.

Observational evidence (such as the CMD) in Figure 2.5 for the globular cluster NGC 5139) shows that almost all Milky Way globular clusters contain multiple populations i.e. a secondary population which appears to have a different evolutionary track evidenced by different chemical abundances shown in the spectra of the stars or by photometric methods e.g. Gratton, R. G. et al. (2011) & Gruyters et al. (2017) and others mentioned in this section. The origin for these populations remains one of compact stellar system physics' most prominent problems and is, as yet, unsolved. There are many theories as to their existence which offer testable predictions (i.e. Gratton, Sneden and Carretta 2004; D'Ercole, D'Antona and Vesperini 2016; Breen 2018) a few of which are covered in Section 2.3, but all

have faced criticism and/or do not offer a fully satisfactory explanation for the existence of multiple populations. While the goal of this project is not to probe an explanation for the existence of globular clusters it is hoped that the research done here may aid future works on the topic.

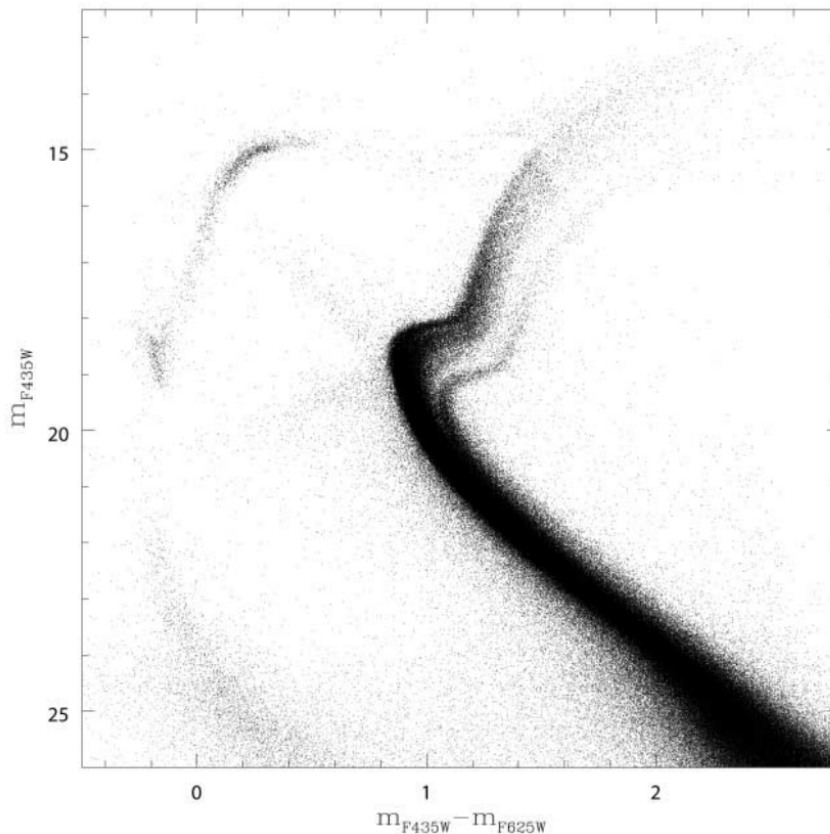


Figure 2.5: This is Figure 1 of Villanova et al. (2007), it shows the CMD of NGC 5139 (ω Cen) where the multiple Red Giant Branches (RGBs) are direct results of multiple populations. Not shown well here are the multiple Main Sequences also present in NGC 5139 which are show in Figure 2.8 from King et al. (2012).

Through photometric studies of galactic globular clusters such as Milone et al. (2018b) & Monelli et al. (2013) it can be assumed that nearly all Milky Way globular clusters contain multiple populations to varying extents. But not all globular clusters in the Magellanic clouds contain them (Milone et al. 2019). Particularly young globular clusters in the Small and Large Magellanic Clouds such as the SMC cluster NGC 419 (age: 1.45 ± 0.05 Gyr; Goudfrooij et al. 2014) which has been shown to posses no significant chemical abundance variations. While other globular clusters in the SMC, such as NGC 416 (age: 6.0 ± 0.5 Gyr; Glatt et al. 2008), do show multiple populations (Milone et al. 2019). This indicates that the younger globular clusters have not yet had time to develop chemically enriched stars

and Bastian and Lardo (2018) states that multiple populations have not been found in any globular clusters younger than 2 Gyr.

2.2.1 Chemical Abundance Variations & Correlations

Star-to-star chemical variations are typically reserved to light elements, but some globular clusters show heavier metal variations which implies that for these clusters a unique enrichment process is happening. Star-to-star variations are most prominent in the bright RGB and Asymptotic Giant Branch (AGB) stars and this has been known since the first discovery of chemical inhomogeneties (e.g. Osborn (1971)). In Osborn (1971), via photometric studies, two stars were found to show significant enhancement in a CN band (Figure 2.6) he calls “C(41–42)” which is a measurement around the 4150Å CN band and the band “C(45–48)” which is a “relatively abundance-insensitive surface-gravity indicator”.

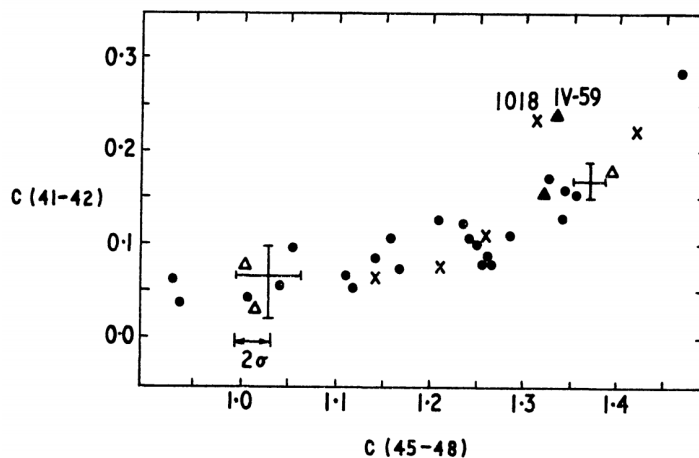


Figure 2.6: This plot is Figure 1 of Osborn (1971) shows C(41-42) against C(45-48) for bright stars in M5 (triangles), M10 (crosses), while other clusters are circles. Stars 1018 (M10) and IV-59 (M5) show significant enhancements in C(41-42).

The first elements known to show abundance variations were nitrogen and carbon but several more light elements have since been discovered to show variations. In a 1980 paper RGB stars were found to show abundance variations for CH, CN, and NH (Bell and Dickens (1980)) it is stated in Bastian and Lardo (2018) that the CH 4300Å is a carbon sensitive region while CN and NH at 3839 & 3360Å are more nitrogen sensitive. In Bell and Dickens (1980) it was shown that nitrogen anti-correlates to carbon, meaning as the nitrogen is enriched carbon is depleted. This is the first case of chemical abundance correlations in the multiple populations of globular clusters.

From the early nineties, higher resolution spectra of individual stars of globular clusters (such as Sneden et al. 1992 & Brown and Wallerstein 1992) were more accessible and as such, direct spectroscopic measurements for particular chemical abundance regions were available. These studies find that most stars in globular clusters were enhanced in alpha elements i.e. Mg, Si, Ca and Ti (Brown and Wallerstein 1992). This is not a sign of multiple populations, however, as the alpha enhancements are almost universal for all stars in a cluster and do not show trends of a secondary “more” enhanced population.

From the higher resolution spectra, however, it was discovered via measurement of sodium and oxygen in stars which already possessed evidence for C and N enhancement that the enhanced N abundance was associated with enhanced Na and depleted O abundances (Sneden et al. 1992). From this, these light element correlations can be described as: N-C anti-correlation, N-Na correlation, Na-O anti-correlation, C-O correlation and therefore N-O anti-correlation. These correlations are shown in Figure 2.7. The figure also shows an anti-correlation involving aluminium and magnesium.

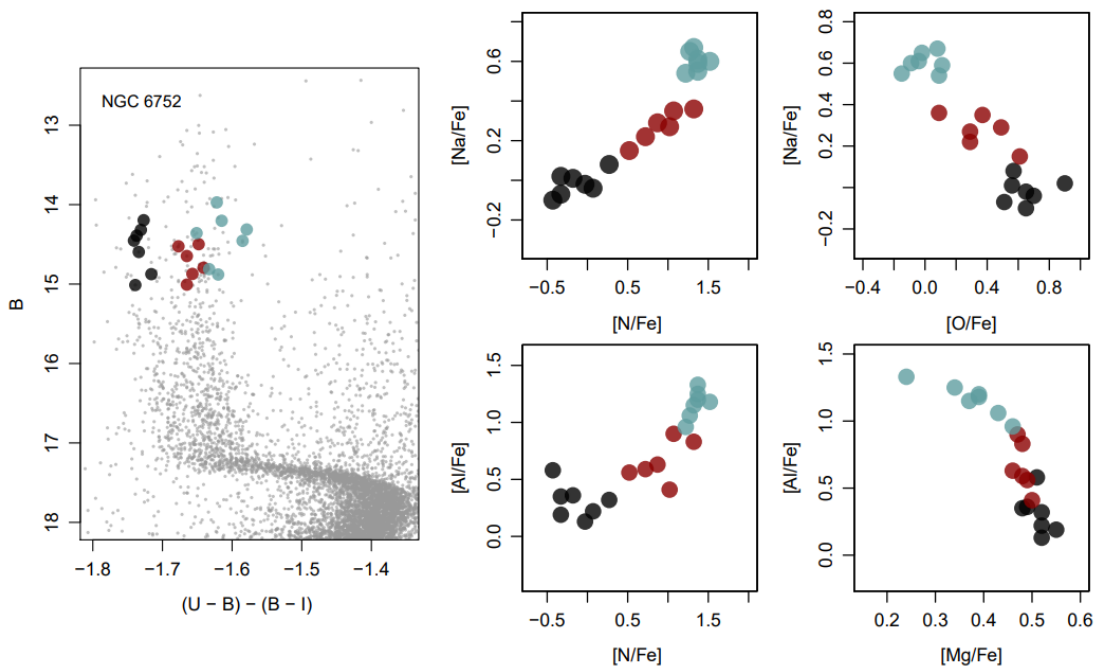


Figure 2.7: This plot is Figure 1 of Bastian and Lardo (2018), shows a CMD for NGC 6752 using photometry for the CMD and spectroscopy from Yong et al. (2005) & Yong et al. (2008) for the four plots on the right hand side. These plots show the correlations and anti-correlations discussed and how the stars selected can be split into three separate populations; a high (blue), moderate (red) and base “primordial” (black) Na enhancement. On the CMD plot the 3 separate populations clearly occupy separate red giant branches indicating, again, distinct populations.

The anti-correlation between aluminium and magnesium is not present in all globular clusters which contain Na-O and N-C variations (Bastian and Lardo 2018). Some clusters have a single Al abundance while others contain a wide range of Al (Mészáros et al. 2015). In this same paper they state the Al and Mg drive the populations in all of the clusters in their sample except for the two most metal rich globular clusters (M107 and M71) where the “grouping is more sensitive to nitrogen”. The Al spreads increase as metallicity decreases for globular clusters (Mészáros et al. 2015). If Al spreads were present in all globular clusters Al-Mg could be used as a potential identifier for multiple populations. But it is clear that since Al abundance spreads are relatively strong at extreme low metallicities, Al could still be used as a potential indicator (although there are no significant Al features in low/medium resolution spectra in visible light so it is not used in this thesis). CN abundance variations are also present in mid-low metallicity globular clusters (Smith and Norris 1993), although at lower metallicities the variations are not strongly defined (Martell, Smith and Briley 2008).

To back up this theory it has been suggested that the presence of (anti-)correlations of C, N, O, Na, and Al abundances are the distinguishing feature of globular clusters compared to other dense stellar systems such as open clusters (OCs) and dwarf galaxies (Carretta et al. 2010a). These chemical variations are so archetypal for globular clusters through photometric observations, if a star in the field of a potential cluster shows N, Na, or Al enhancement as well as either C or O depletion that star is considered to have originated from a globular cluster (Bastian and Lardo 2018) (with the possible exception of binary systems which undergo mass transfer i.e. Fernández-Trincado et al. 2019 & Wei et al. 2020). The assumption that all stars chemically enhanced in those elements are formed in globular clusters, however, indicates that $\sim 3\%$ of all metal poor stars in the local field are originally from globular clusters (Carretta et al. 2010a & Martell et al. 2011).

Spreads in the helium abundances are another key indicator of multiple populations. It has been shown for many clusters, not just in the Milky Way but intermediate age Magellanic Cloud clusters, that they possess clear He spreads (e.g. Chantreau et al. 2019 & Milone 2014). For massive globular clusters the helium enhancements cause spreads in the main sequence (Milone 2014) (shown in Figure 2.8a for ω Cen and in Figure 2.9 for NGC 2164), where the other signatures of multiple populations are dominant in the RGB and AGB branches. This is because the production of He is a direct result of H burning in the main sequence and is expected. While C, N, O and Al are a result of the CNO cycle and other pathways for Al and heavier elements which are dominant in the red giant branch (Figure 2.8b).

Between different populations in globular clusters Fe and metallicity in general do not

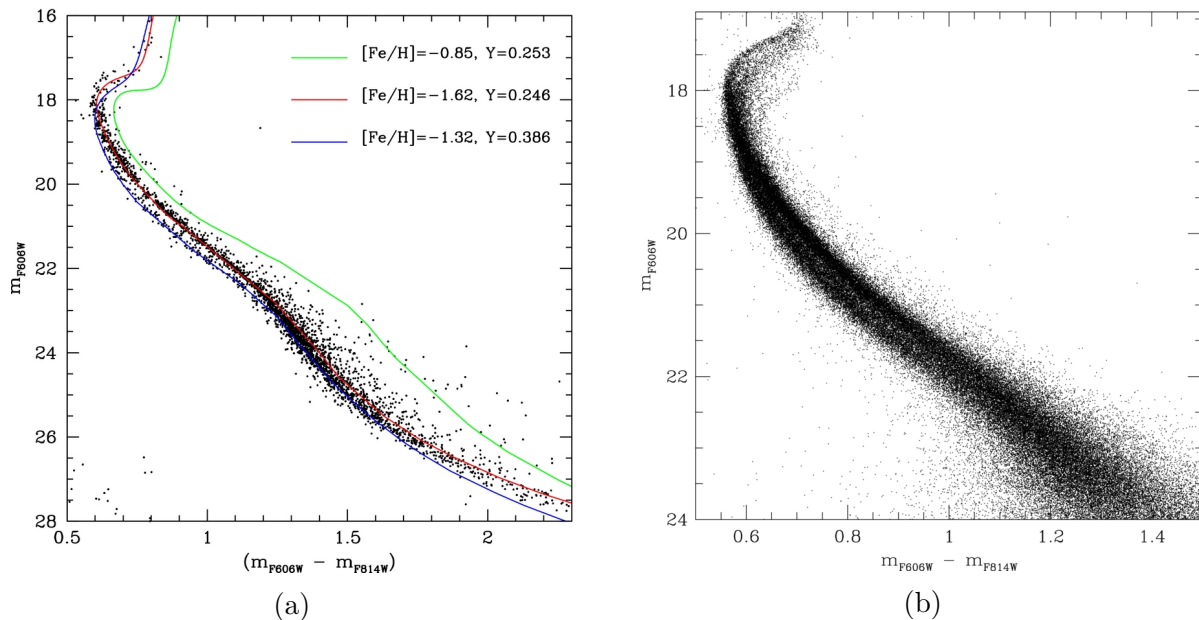


Figure 2.8: Both plots are of NGC 5139 (ω Cen) and are originally from King et al. (2012) of which plot (a) is Figure 5 and plot (b) is Figure 7. Plot (a) shows the CMD for a section of the outer field of the globular cluster where clear different populations can be seen along the main sequence over plotted by isochrones of $[\text{Fe}/\text{H}]$ and He abundances. Plot (b) The CMD of the central field for NGC 5139 after “quality selection and reddening correction”. This plot shows both the separate MS spreads shown in (a) and the multiple RGBs seen in Figure 2.5.

vary except for a few rare circumstances (Bastian and Lardo 2018). Exceptionally large GCs such as NGC 5139 and NGC 6715 display abundance variations in heavier elements not seen in the majority of globular clusters (Johnson and Pilachowski 2010 & Carretta et al. 2010b) where light element abundance variations are the norm. The Fe variation (Johnson states as $-2.2 \leq [\text{Fe}/\text{H}] \leq -0.6$ for NGC 5139) is generally attributed to ejecta from Type I and Type II supernova being contained within the cluster by its own gravity. This then pollutes stars directly via accretion or pollutes the pristine primordial gas still in the system affecting secondary rounds of stellar formation. Fe variations can also be due to accretion of gas from the Interstellar Medium (ISM) outside of the cluster over long periods of time (Bastian and Lardo 2018). The effects of Fe abundance variations can also be seen in some CMDs (see Figure 2.8a) where isochrones with varying $[\text{Fe}/\text{H}]$ (as well as He) fit well to the perceived separate main sequences.

2.2.2 Single Population Globular Clusters

There are very few globular clusters which do not present some evidence of secondary stellar populations (Bastian and Lardo 2018). Out of the 86 globular clusters used in this project only a few do not currently have detected multiple populations (Table 8.2). Although it is important to know which GCs do not possess MPs so a clearer definition of the signatures of MPs may be defined.

Bastian and Lardo (2018) states there are four globular clusters in the Milky Way which do not contain MPs: Terzan 7 (Ter 7), Palomar 12 (Pal 12), Pal 3, and Ruprecht 106 (Rup 106). Ter 7 and Pal 12 are both thought to be ex situ GCs that were originally formed in SagDEG (Cohen 2004 & Tautvaišienė et al. 2004) and both have young ages compared to the majority of Milky Way globular clusters and are very low mass (Bastian and Lardo 2018). Pal 3 is a very distant GC in the galactic halo and as such does not have enough photometric evidence to show abundance spreads of elemental (anti)correlations (Bastian and Lardo 2018). The globular cluster E3 has also been found to contain no evidence for multiple populations from low resolution spectroscopy (Salinas and Strader 2015). E3 is metal rich but has a very low mass ($\sim 1.4 \times 10^4 M_{\odot}$; Salinas and Strader 2015). MPs have been found in some low mass globular clusters, the lowest being NGC 6535 ($M = 10^{3.58} M_{\odot}$; Milone et al. 2017). However, it has been shown in the UV GC Legacy survey (Milone et al. 2017) that there is a strong correlation between cluster mass and the percentage of a secondary population. This, in combination with known low mass GCs having no MPs, indicates that there may be a lower limit to mass of a cluster able to show multiple populations.

The Magellanic Clouds (MCs) are host to both very young and old globular clusters. It has been shown that a few (~ 6 Milone et al. 2019) of these young GCs contain no evidence for secondary populations. The possession of no secondary populations is only apparent for the very young globular clusters of the MCs, mid to old age ($\sim > 2$ Gyr) globular clusters all show similar abundance variations in secondary populations to those in the Milky Way (e.g. Mackey 2009; Chantreau et al. 2019; Milone et al. 2019). Lack of MPs in young globular clusters (that share similar properties to larger GCs that do possess MPs) suggests they have not had time to develop secondary populations yet. This could indicate that MPs are the result of a second phase of star formation or strong pollution of a fraction of its stars (among other formation theories, see Section 2.3) the effects of which do not come into effect until a few Gyr after GC formation. In the Magellanic clouds however, some very young globular clusters such as NGC 330 (~ 30 Myr; Sirianni et al. 2002) and NGC 2164

(~ 100 Myr; Milone et al. 2018a) have been found to possess split main sequences (Figure 2.9) proposed to be due to some bright and large ($\sim > 1.6M_{\odot}$) MS stars rapidly rotating (red-MS) while others slowly rotate (blue-MS), meaning they cannot be comparable to single stellar populations (Milone et al. 2018a). This phenomenon of a split main sequence in young LMC GCs does not occur in NGC 1868 which has a relatively low mass compared to other young LMC clusters indicating that mass may be the attributing factor to the split MS.

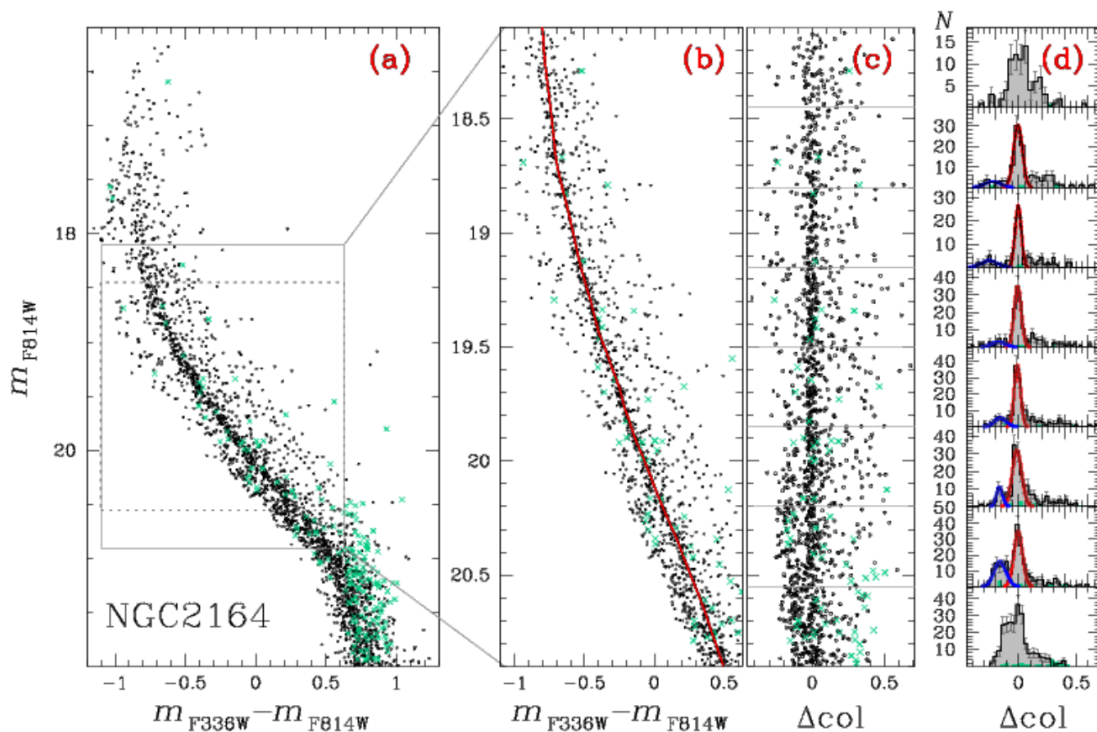


Figure 2.9: This plot is Figure 13 of Milone et al. (2018a), it shows the process that they used to separate the estimated blue MS from the red MS. Plot (a) shows the m_{F814W} vs. $m_{F336W} - m_{F814W}$ CMD, and plot (b) is a zoomed in region of plot (a). plot (c) shows the “verticalised m_{F814W} vs. Δcol diagram for the stars plotted in plot (b)”, while plot (d) shows the histogram of the separate blue and red main sequences separated into 8 intervals with best-fit bi-Gaussian functions overlaid onto each interval.

2.3 Formation Theories of Multiple Populations

While not essential for this thesis, an understanding the possible formation methods of multiple populations may increase insight of the signatures that this thesis is attempting to detect.

The mechanism which drives the C, N and O abundances is fairly well explained through the CNO cycle which becomes more dominant as stars transition from the main sequence to the red giant branch (and is dominant in stars of mass $\geq 1.3M_{\odot}$). In very hot stars the Triple-alpha process produces $^{12}_6\text{C}$ and also produces a stable oxygen isotope ($^{16}_8\text{O}$). Sodium, Magnesium and Aluminium are made via the Ne-Na and Mg-Al chains (Rolfs and Rodney 1988 & Arnould, Goriely and Jorissen 1999) which is a somewhat complex process of proton and alpha particle capture and the decays of unstable isotopes such as silicon 27. As was stated in the previous sections Fe and heavier elements are created during SN events and via the s-process but since heavy elements generally do not vary from star-to-star in globular clusters (except the very largest) these processes are not as relevant to multiple population formation.

The processes above explain the presence of these light elements but they do not explain the variation in star-to-star abundances seen. Since it is accepted that all of the stars in a GC formed from the same gas cloud the ratios of elements involved in the cycles and chains which create the elements should be the same resulting in similar abundances for each elements for different stars of the same age, metallicity and evolutionary stage. Bastian and Lardo (2018) states “The evidence that each GC has its own specific pattern of MPs calls for a high degree of variety (or stochasticity) that must be taken into account when proposing MP formation mechanisms”. Because of this it is often suggested (Gratton, Carretta and Bragaglia 2012 Bastian and Lardo 2018) that the presence of multiple populations is not reliant on one mechanism but multiple, whose contribution to the ratio of secondary populations is directly proportional to the properties of the original gas cloud and IMF of the GC.

2.3.1 AGB Stars

There have been many attempts to explain the abundance variations seen in GCs. AGB stars have been subject to the highest amount of attention due to their mass-loss by radiation pressure.

AGB stars are first formed in a stellar system at around ~ 30 Myr (Bastian and Lardo 2018). They produce slow velocity ($\sim 10 - 30 \text{ kms}^{-1}$; Loup et al. 1993) stellar winds which are slow enough to be contained by the system’s gravity. They work by large-scale convection cells bringing newly-formed elements to the stellar surface and due to the stars instability, pulsations can cause shock waves in the stellar atmosphere which eject large amounts of gas and dust into the local interstellar medium (Höfner and Olofsson 2018). For multiple

populations to form, this Intra-cluster Medium (ICM) material would cool and sink to the centre of the cluster where, when the critical point is reached, star formation of a secondary population would start (e.g. D’Ercole et al. 2008 & Bekki 2017). AGB stars can burn hydrogen at higher temperatures than other stars which gives access to the Mg-Al chain which can explain the Mg depletions from the Mg-Al anti-correlation shown in Figure 2.7.

There are several problems with using purely AGB stars to explain multiple populations. Bastian and Lardo (2018) states that all models using purely AGB stars do not create a Na-O anti-correlation seen in all multiple populations. The only way these models can produce Na-O anti-correlations is via mixing of the ejected material with pristine gas which formed the first generation of stars. Another problem is that for many of the models, the amount of enhancement needed to match observations is not reached for many elements such as Na and N (Bastian and Lardo 2018), this indicates that the AGB method alone does not produce enough mass to get the fraction of secondary population stars seen. This is due to the IMF of globular clusters, which have only a small amount of stars in the correct mass range to produce the polluting gas and dust needed for a secondary population.

This whole theory, though, is relying on the gas and dust getting cold enough for star formation. This may not be possible in globular clusters. Conroy and Spergel (2011) have shown in their models that Lyman-Werner photon flux of stars from the first population is high enough that the gas is unable to cool and sink to the core until the system is 200 - 300 Myr which delays the formation of a secondary population considerably. There are also many other methods of heating ICM material which would delay or outright stop secondary star formation periods. Applying a population of heating x-ray binaries to the D’Ercole et al. (2008) model, for example, would cause the ICM to flow out of the system entirely (Bastian and Lardo 2018). However, Bastian and Lardo (2018) state that the sum of C, N and O would not match observed levels for AGB stars of certain masses if there were a delay in formation of the period stated in Conroy and Spergel (2011).

2.3.2 Fast Rotating Massive Stars (FRMS)

This theory works much in the same way as that of using AGB stars. Material is ejected from stars which then subsequently cools and sinks to the core of the cluster where formation of a secondary population can take place. This then therefore suffers from the same problem of gas cooling as the AGB based theories.

Massive stars burn very hot and therefore can produce the elements that are seen to be enriched during the MS. Massive stars that rapidly rotate undergo rotationally induced mixing that in some cases for the most rapidly rotating FRMS can be almost fully mixed. The (now) mixed matter on the surface can then be released into the ICM. As shown in Figure 2.9 split main sequences can be due to the light emitted by rapidly rotating stars where the material on the surface is mixed and so the light emitted from the star is affected. Milone et al. (2018a) state that the red-MS is made up of fast rotating $H\alpha$ emitting stars which causes the MS split (and extended MS).

This theory, as was explained, is not exempt from its flaws. FRMS cannot explain Mg spreads present in some globular clusters as they are not able to activate the Al-Mg chain before the end of the MS (Bastian and Lardo 2018).

2.3.3 Binary Interactions

Binary system interactions have been suggested to be a solution to the MPs problem. de Mink et al. (2009) created a model binary system with a $20 M_{\odot}$ star and a $15 M_{\odot}$ star. They noted that the $20 M_{\odot}$ star shed $10 M_{\odot}$ of material. This material was strongly enhanced in He, N, Na and Al while depleted in C and O in similar amounts to the abundances seen in multiple populations. They also estimate that the mass contributed via slow gas ejected from the binaries is greater than that of AGB stars and FRMS combined, and that if diluted with an equal amount of pristine gas from the first round of star formation, can provide enough mass to produce a second generation of low mass stars.

A key problem to all theories that rely on secondary epochs of star formation early in the life of a globular cluster are that after 3-8 Myr SNe events begin (Bastian and Lardo 2018). This disrupts all of the gas and dust which theoretically would be cooling and sinking to the core for star formation. If the material from the SN were kept within the system, large Fe spreads (like that of ω Cen) would be visible for all clusters that exhibit MPs. Since we do not see Fe spreads, we can assume the material is ejected. This, however, means that the dust and gas meant to form the secondary populations is also ejected, unless it is released after the period where SN occur.

Going back to binary systems; Wei et al. (2020) ran a model of a low mass (0.9 and 1.9 M_{\odot}) binary and found that the star that was accreting showed C and O depletion and N and Na enhancement while they were still “unevolved” stars which was significantly different

from their original abundances. This indicates that low mass binaries could also be a cause of stellar pollution giving the appearance of a secondary population. However more work on low mass binary evolution models is required to fully understand the contribution to GC and MP development.

2.3.4 Black Hole Accretion Disk Nucleosynthesis

Many globular clusters contain black holes. It is predicted that the MW globular cluster NGC 3201 has over 200 stellar mass black holes in its core (Kremer et al. 2018) (although it is not the present day number of black holes that matters, but the initial population a few Myr into GC formation). The accretion disks of black holes have long been known to possess regions hot and dense enough for nucleosynthesis (e.g. Mukhopadhyay and Chakrabarti 2000 & Hu and Peng 2008) and it is suggested that these regions could be key contributors to the metal enrichment of galaxies (Hu and Peng 2008).

It has been suggested recently that nucleosynthesis in the accretion disks of black holes can account for the abundance variations seen in globular clusters (Breen 2018). They assume, since the black holes needed for this theory formed after only a few Myr, the ICM is still gas rich, with the medium sinking (being “funnelled”) to the centre of the cluster. Their theory also relies on the black holes being clumped together near the core of the cluster where they can accrete this matter.

They state that young clusters becomes gas free at about ~ 7 Myr and the fraction of enriched stars relies on this timing (i.e. the longer this time the higher the fraction of enriched stars). The way it works in their theory is that gas is accreted onto the disk and exposed to high enough temperatures and densities for nucleosynthesis to occur enriching the inflow (Breen 2018). It is expected that most of the matter on the accretion disk is then ejected via outflows (King and Pounds 2003) and, according to Breen (2018), 70% of the inflow material which is enriched is ejected from the accretion disk. The material is ejected at speeds of $\sim 100 - 1000 \text{ km s}^{-1}$ (Kaaret, Feng and Roberts 2017), which is faster than the escape velocity of the GC, but Breen (2018) state that as long as the cluster is still embedded in its primordial cloud of pristine gas, the ejecta will lose its kinetic energy to the gas. Nucleosynthesis in accretion disks can produce the Na-O and N-C anti-correlation (Breen 2018) but does not account for the full spreads in some of the elements seen in observations. It does not satisfactorily explain enrichment of heavier elements (i.e. Mg and Al).

This theory relies heavily on gas remaining from the initial star formation period and Breen (2018) states that the gas does not clear the system until ~ 7 Myr. But in order to have a black hole a star must have exploded as a supernovae, which would clear the gas from the system. However they suggest that the black holes formed without supernovae events. It has been suggested that the most massive black holes (with progenitor mass of $\geq 40M_{\odot}$) are massive enough to form via direct collapse so there was no SN in their formation (or an explosion occurs but its energy is too small to significantly disrupt the stellar envelope) allowing the primordial gas to stay in the system (Fryer 1999 & Fryer and Kalogera 2001). The existence of massive black holes in globular clusters is possible (Kawakatu and Umemura 2005) as is the existence of massive stars for the formation of these black holes (Gieles et al. 2018) so this theory could potentially explain some of the abundance spread seen. However more research is needed in the topic and it is clear that all theories attempting to explain the presence of multiple populations in globular clusters have their flaws.

and analysis techniques which are used to measure the age or initial mass function of stellar populations. However there are many other uses for this data (Usher et al. 2017).

Most Milky Way globular clusters are very old with ages comparable to that of the Milky Way itself as stated in Section 1.1. However many LMC and SMC globular clusters have relatively young ages such as NGC 330 (SMC) and NGC 2136 (LMC) which have ages of 30 and 100 Myr, respectively (Sirianni et al. 2002 & Niederhofer et al. 2015). By including these younger clusters it is possible to compare globular clusters at different points of their evolution potentially leading to probes of their formation and how different populations of stars have evolved.

The advantages of integrated light spectra of globular clusters are that they can be used to study stellar systems at a much greater distance where the constituent stars do not need to be individually resolvable and good S/N is still achievable due to the high overall surface brightness of GCs. The WAGGS survey uses globular clusters whose constituent stars are individually observable. Because of this, through photometry of individual constituent stars, key parameters of the globular clusters can be obtained and used to verify the methods used with the integrated light spectra. Any methods using integrated light spectra could then potentially be used on extragalactic globular cluster candidates either verifying or refuting the presence of MPs.

3.1.1 Globular Cluster Selection

It is important to note how WAGGS selected the globular clusters for the sample as the number of local globular clusters and what defines a globular cluster are still up for debate.

The WAGGS team, instead of wanting to use a full sample of galactic globular clusters, wanted to get a representative sample of globular clusters (Usher et al. 2017). This was partly because not all GCs would be visible to their instrument. They first used the Advanced Camera for Surveys (ACS) Globular Cluster Treasury Survey (Sarajedini et al. 2007) which provided Hubble Space Telescope (HST) ACS images of 65 globular clusters. The WAGGS team then supplemented these images with 6 globular clusters from the Milky Ways halo observed with ACS in a similar method by Dotter, Sarajedini and Anderson (2011). In addition they observed several bright MW globular clusters that are not in the ACS Globular Cluster Treasury Survey with published chemical abundance values obtained from high-resolution spectroscopy. A number of bright globular clusters which were relatively poorly

studied in comparison were added to the sample to both increase the coverage of the galactic bulge and the halo as well as to increase the overall sample size (Usher et al. 2017).

Milky Way globular clusters are almost all old and very metal poor. In order to increase the range of ages and chemical compositions in the sample, the sample was supplemented with globular clusters from the Milky Ways satellites: LMC, SMC and the Fornax dwarf spheroidal (dSph) galaxy. They chose three old age (age > 10Gyr) globular clusters in Fornax, four in the LMC and one in the SMC. In the LMC they also selected six young (age < 1 Gyr) and four intermediate age (1 < age < 10 Gyr, although as was stated previously there is an age gap of intermediate age clusters in the LMC) globular clusters. While in the SMC they select one young and 3 intermediate age globular clusters (Usher et al. 2017), see Table 8.2 for the full list of GCs available for this project.

It should be noted that to get a value of mass for each GC they used luminosity based masses as dynamical masses are not available for all GCs in the sample. One problem with WAGGS is that the sample is biased towards more massive GCs. They “favoured GCs with a higher central surface brightness in order to maximise observation time [efficiency]” (Usher et al. 2017) i.e. they could get satisfactory signal to noise ratios for the brighter objects with shorter observations than would be needed for less bright GCs. But, more massive GCs are preferable anyway as the effects of stochastic sampling of the IMF are less severe.

3.1.2 Observations

The spectra were obtained using the Wide-Field Spectrograph (WiFeS) on the ANU (Australian National University) 2.3m telescope based in the Warrumbungle national park, Australia, observing a single central pointing for each globular cluster. This is different to other types of measurement such as drift scanning which typically allows an object to drift over the spectrograph slit taking much more of the full light of a cluster but having a lower signal to noise for the same exposure time (Kim et al. 2016) (although this is normally done on more massive objects than globular clusters e.g. Jansen and Kannappan 2001). The SNR for the WAGGS data is shown in Table 3.1

WiFeS has a field-of-view of 25×38 arcsec which covered only a small fraction of the full light for many of the globular clusters in the sample. The large variety of distances also led to the fraction of observed light varying considerably from cluster to cluster (see Figure 3.3). The effects of this are considerable when studying the ‘closer’ globular clusters with

Table 3.1: Signal to noise ratios of the WAGGS data.

Grating	λ_{min} Å	λ_{max} Å	S/N_{min} Å ⁻¹	S/N_{mid} Å ⁻¹	S/N_{max} Å ⁻¹
(1)	(2)	(3)	(4)	(5)	(6)
U7000	4000	4050	0.3	29	264
B7000	4800	4850	4.4	77	689
R7000	6400	6450	1.2	161	1145
I7000	8400	8450	7.9	157	911

Notes. (1): Grating. (2): Minimum wavelength for S/N calculation. (3): Maximum wavelength for S/N calculation. (4): Minimum S/N per Å. (5): Median S/N per Å. (6): Maximum S/N per Å. This table is from Usher et al. (2017) Table 3.

a larger angular size as the smaller observed light fraction would not adequately take into account stochastic effects of the stellar distribution inside globular clusters, i.e. the spectra may not fairly sample the stellar population present. This is a concern, as a poorly sampled field-of-view for a globular cluster may not include all stages of stellar evolution which could have dramatic effects on the integrated light spectra measured. The field-of-view of the WiFeS spectrograph is shown in Figure 3.2 where three globular clusters are shown with varying heliocentric distances. In the plot it is clear how the spectrograph only covers a small fraction of the globular cluster NGC 6121 whereas the opposite is true for Fornax 3. In globular clusters with large heliocentric distances such as Fornax 3, external objects to the globular cluster could have an effect on the integrated light spectra as they are still in the field-of-view. Although, it should be noted that the number of globular clusters whose half light radius would be within the field-of-view of the spectrograph (and thus potentially have a relatively large proportion of external objects) is very small. This is indicated in Figure 3.3 where the median fraction is 0.17 and 0.12 for only the Milky Way globular clusters (Usher et al. 2017).

The fraction of observed luminosity in the WiFeS field-of-view ranges from 0.81 for Fornax 4 to as little as 0.005 for NGC 5139 (Usher et al. 2017). These values are shown in Figure 3.3 where they have been separated into 11 separate bins. The total stellar mass in each cluster and the mass in the observed field-of-view is available in Table 8.2 with the literature values for mass coming from a variety of sources in the supplementary files of Usher et al. (2019) with all of the Milky Way globular cluster masses coming from the 2010 update of the Harris (1996) catalogue.

However in order to keep as large a sample size as possible, stochastic effects in the spectra have been assumed to be minimal. Stochastic effects may explain large data spreads

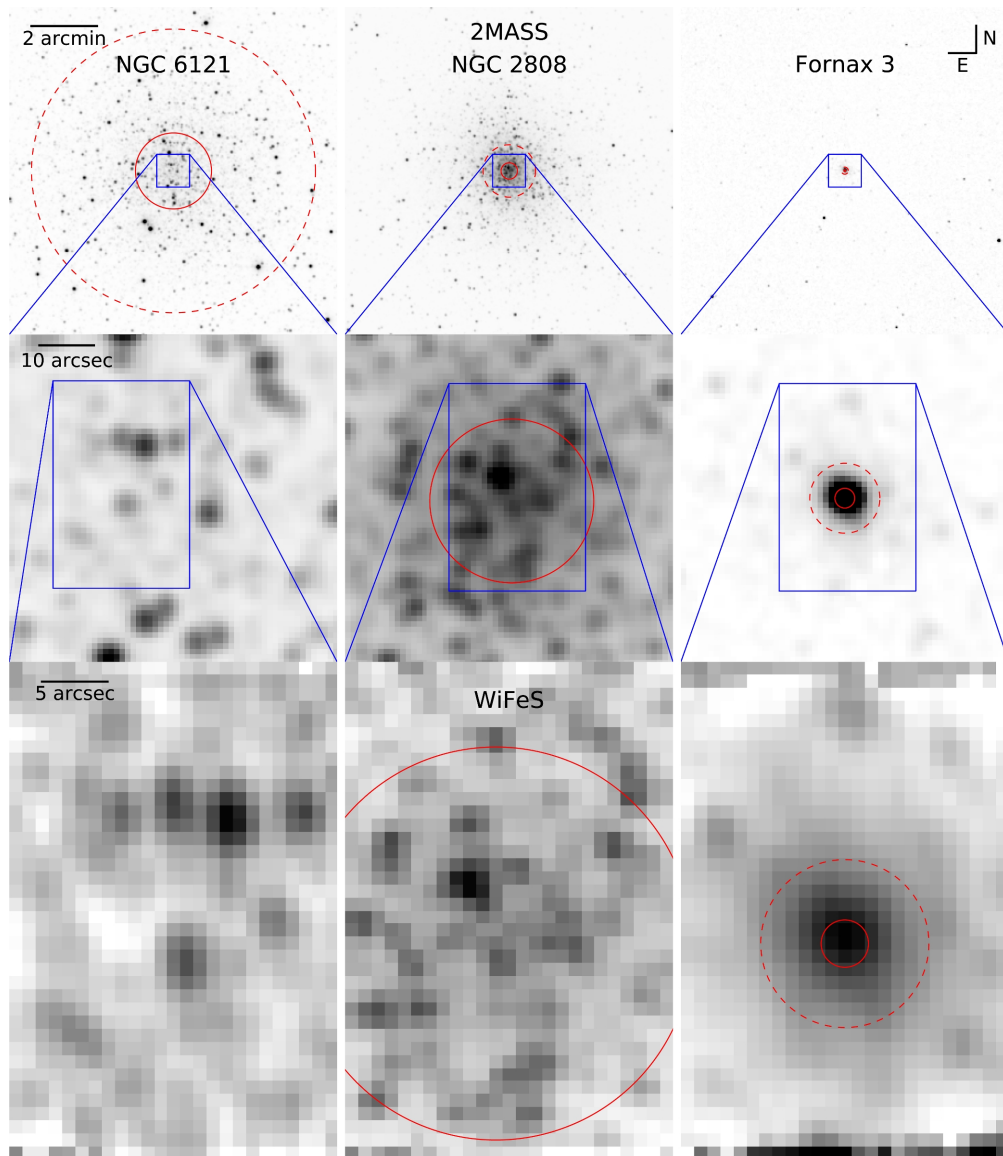


Figure 3.2: Field-of-view of the WAGGS observations for 3 GCs. Fornax 3 (right), NGC 2808 (middle) and NGC 6121 (left). This plot is Figure 2 from the first WAGGS paper (Usher et al. 2017) and shows the field-of-view of the WiFeS spectrograph in the bottom row of images. The dashed red line shows the half-light radius while the solid red line shows the core radius of the GC. The blue lines are the footprints of the preceding image.

seen in the comparison between some of the measurements of this project and those seen in other papers (e.g. Kim et al. 2016). A full description of this is given in Section 5.3.

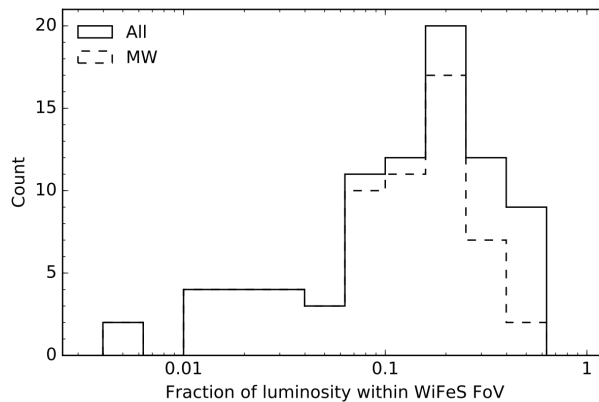


Figure 3.3: The fraction of the V-band luminosity in the WiFeS field-of-view compared to the full v-band luminosity of the GC. The dashed line represents Milky Way GCs while the solid line represents the full sample of GCs. This plot is part of Figure 3 from the first WAGGS publication (Usher et al. 2017).

3.1.3 Equipment & Data

The field-of-view of WiFeS (as stated previously) is 38×25 arcseconds which consists of 25 slitlets that are 1 arcsecond wide and 38 arcseconds long and covers a wavelength range of 3300 - 9000 Å.

The WiFeS Spectrograph works on a similar design to the ANU Duel-Beam Spectrograph (DBS) (Rodgers, Conroy and Bloxham 1988) and the Near-Infrared Integral-Field Spectrograph (NIFS) (McGregor et al. 1999) and is designed to simultaneously take as many spectra as possible. The process behind how spectrographs work is quite simple: by passing light through a small slit it is reflected across a diffraction grating which separates the light according to wavelength, this is then picked up on a photo-detector. The WiFeS Spectrograph has four high resolution gratings: U7000, B7000, R7000, I7000 and 2 low resolution gratings: B3000 & R3000. The WAGGS survey only uses the higher resolution ‘7000’ gratings. Shown in Figure 3.4, there is a good amount of overlap between the gratings allowing for zero loss of data in these transition areas and in the data reduction process these are good regions to calibrate flux between the spectra. The data itself is open source and can be found online at Usher (2017).

There are two resolutions of grating in the spectrograph $R = 3000$ & $R = 7000$. In the WAGGS survey only data taken in the $R = 7000$ was published. The WAGGS survey offers higher resolution spectra of a large range local globular clusters in the visible range than previous surveys (i.e. Schiavon et al. 2005 & Kim et al. 2016).

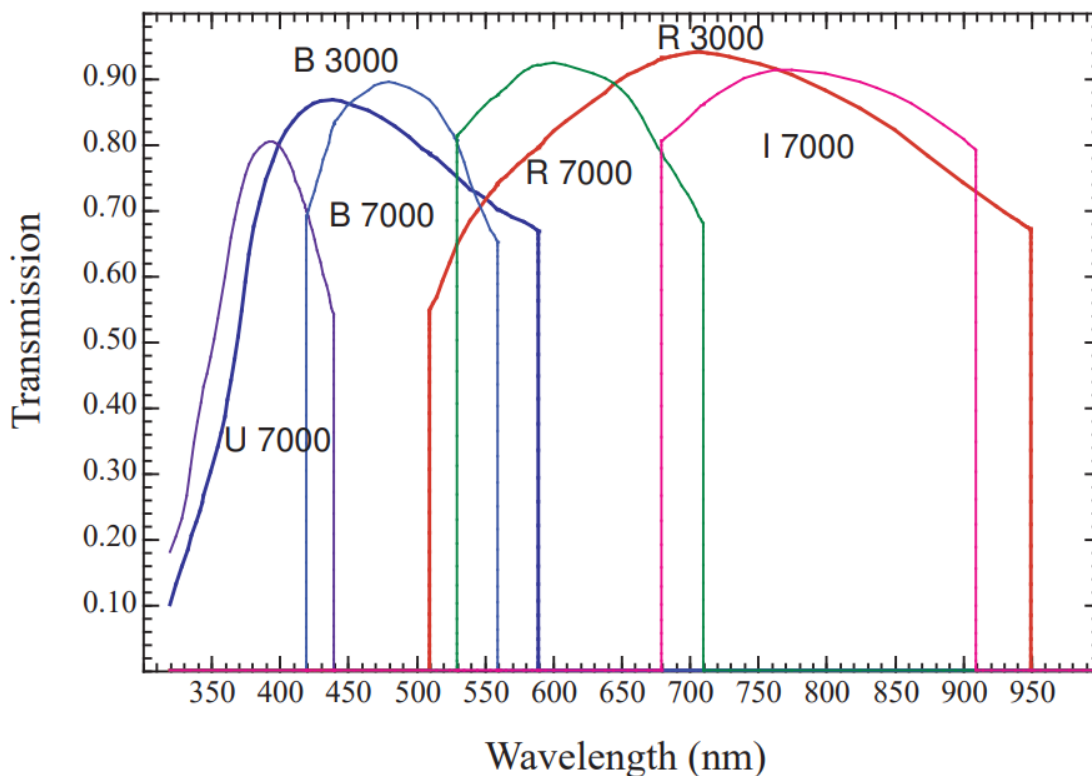


Figure 3.4: The Grating efficiencies of the WiFeS gratings at the most efficient angle of incidence. The plot includes the curves for both the low resolution $R = 3000$ and high resolution $R = 7000$ grating, and the efficiencies are only shown for the wavelengths at which the grating is used (this plot is Figure 10 of Dopita et al. 2007).

3.2 Reduction

The WAGGS survey published already flux calibrated and normalised spectra (e.g. Usher 2017 & Usher et al. 2017). Therefore the remaining reductions to the spectra that needed doing were the redshift adjustment and combination of the gratings for each globular cluster, to make one continuous spectrum for each (Figure 3.5 shows WAGGS redshift adjusted spectra for just the B7000 grating).

The WAGGS team used the WiFeS data reduction pipeline “PyWiFeS” to reduce the raw data into what is published in their survey. The PyWiFeS pipeline also produced 1σ error spectra for each globular cluster which is used in this project to measure all uncertainty on the data.

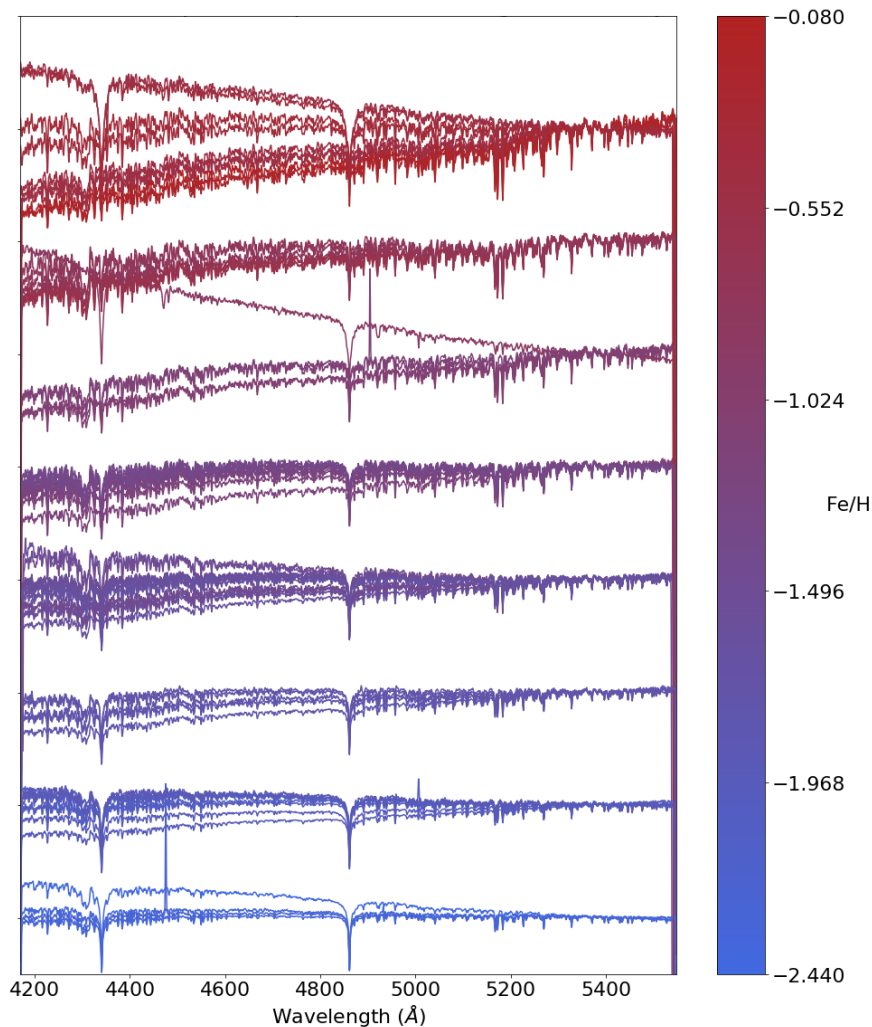


Figure 3.5: The redshift adjusted B7000 grating spectra for the majority of the globular clusters separated according to $[\text{Fe}/\text{H}]$ into 8 bins.

3.2.1 Redshift

In the second WAGGS data release (Usher et al. 2019), supplementary data was provided containing literature values of the globular clusters in the data set: host galaxy, half-light radius, stellar mass, $[\text{Fe}/\text{H}]$, and age for example. A full table set is available in the Appendix (Table 8.2). The key parameter for calculating the redshift of these globular clusters in the supplementary data was the radial velocity. Redshift is calculated via the equation:

$$z = \sqrt{\frac{1 + v_r/c}{1 - v_r/c}} - 1 \quad (3.1)$$

Where z is redshift, v_r is the radial velocity and c is the speed of light. As these globular clusters are gravitationally bound to the Milky Way, the redshift is due to the line of sight orbital motion velocities of each GC.

This is why the most consistent way of measuring radial velocity is by the reverse of the process stated above. First an initial spectrum is observed; the key absorption lines in the wavelength range are identified and a correction is made via the equation: $\lambda = \lambda_i/z$. If the alignment was correct the provided value of z should work for all wavelengths.

Shown in Figure [3.6](#), after redshift adjustment the total flux in each spectra may have been adjusted due to the original wavelength flux bins not aligning properly with the redshifted flux bins. Since the redshift adjustment is wavelength dependant, the pixel scale had changed respective to the original wavelength (λ_i). This was first fixed by writing a simple Python code using “numpy” and other base packages, regridding the wavelength array to have pixel width values of 0.4\AA . To get the correct flux value for each new regridded pixel, the flux values per pixel in the spectra had to be interpolated over the new wavelength range to align each data point with the correct wavelength. Then, by multiplying the regridded flux by the ratio of the sum of the original flux over the sum of the interpolated flux, the total flux value of the spectra was conserved. A simple safety check was to compare the sum flux of the original spectra and the sum flux of the redshifted and regridded spectra, verifying the process was correct if the two values were equal. This is an important step, when measuring line indices which cover a transitioning continuum, consistent continuum flux must be had between gratings.

In the regridding process instead of making the pixel scale the same as before, the pixel scale was made universal for each grating to a value of 0.4\AA . This was done because programs such as pPXF required consistent spacing between the pixels. Each grating had an individual pixel width: 0.27240, 0.34693, 0.43919, 0.56628\AA , respectively. 0.4\AA was chosen as an average of these. However one problem this caused in the process of conserving the flux was that the differences between the pixel widths and the new value was different for each grating, leading to the ratio needed for flux conservation being different for each grating. Thus smooth transitions between gratings was impossible. The solution for this was to incorporate a normalisation process similar to the one used in the WAGGS paper (Usher et al. [2017](#)). The spectra in the B and R gratings were normalised to unity by division of the flux by the average flux in the range $5300 - 5400\text{\AA}$. This would make the average flux in the overlapping regions for both gratings the same. The gratings U7000 and I7000 were then normalised to the average flux in the overlapping regions with B7000 and R7000 respectively.

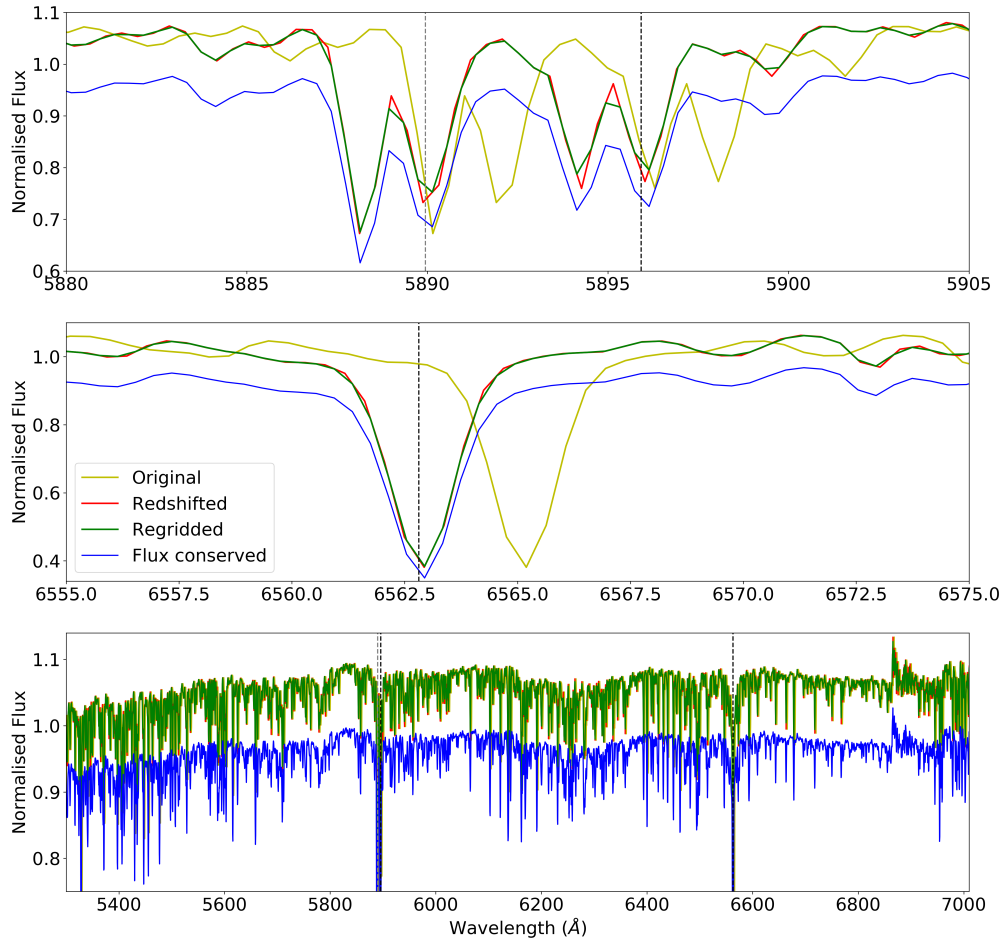


Figure 3.6: Plot showing the original spectrum for the GC NGC 2808, the redshifted spectra, regridded spectra, and flux conserved spectra at the NaD / H α regions and the full R7000 grating.

The normalised redshifted spectra could now be combined into single spectra covering the full WiFeS range.

Another method which could have been used was to first regrid the wavelength range to have the pixel width of the original and flux calibrate that. Then after combination of the gratings the new full spectrum would be regridded to have the pixel width of 0.4\AA . This would have been simpler for the original regridding but then another would have to be done to get a single pixel width for the full spectrum. It was decided that doing one regrid to a new pixel width before combination was a more efficient method and the differences in the data between the two methods were negligible.

3.2.2 Combination

As stated in Section 3.1.3, and shown in Figure 3.4, WiFeS made use of 4 gratings which covered the wavelength range 3300 – 9000Å: U7000, B7000, R7000, and I7000 with a large amount of overlap between the gratings. Individually, the gratings covered the wavelength ranges: 3270 – 4350, 4170 – 5540, 5280 – 7020 and 6800 – 9050Å, respectively.

In order for more efficient progress it was preferable to combine the gratings. A code for this was written in Python (again just using normal packages such as numpy and pandas) for all 86 globular clusters except for those stated in Section 3.2.4. Since there was overlap between each grating, it was important to decide how these regions were going to be handled. The efficiency of each grating is plotted in Figure 3.4 and it is shown that the blue side of each grating is more efficient than the red side of the previous grating in the overlapping regions. Because of this, in each overlapping region the data from the ‘redder’ grating would preferably be used. i.e. in the U-B overlap only the B data would be used in the combination and the U data removed.

However, features of known interest (i.e. the CN region) lay in a region where two gratings overlap. For these features it would be preferable to have continuous spectra from the same grating so slight differences in flux and signal to noise would not appear in the index region, either in the blue or red continuum or the measured section (See Figure 5.1). Because the data had previously been normalised the point where two regions aligned was seamless and, on well flux calibrated data such as this, the effects were not significant in the resulting measurements. However the reduced efficiency of transmission would lead to a lower signal to noise and result in larger uncertainties. The changes in uncertainties between the different combination methods, however, are negligible compared to the uncertainty values.

The regions of interest in which it was important not to have the transitions between were the CN₁ and CN₂ regions which were key to the identification of potential abundance enhancements, as well as the LICK/IDS region Fe5270 which is essential in the calculation of [MgFe]’ (Section 6.2.1). Since [MgFe]’ is the key value in which metallicity is valued in this thesis, it was essential Fe5270 was accurate. The regions are shown in Figure 3.7 b & c.

The full combination process is fairly simple and was completed by writing another simple Python code. First the last 10 pixels of each grating were removed to allow for the removal of zero values seen at the end of each grating in Figure 3.7a&b. Then, for the overlap of two consecutive gratings, the ‘redder’ grating’s overlapping region was removed (excluding

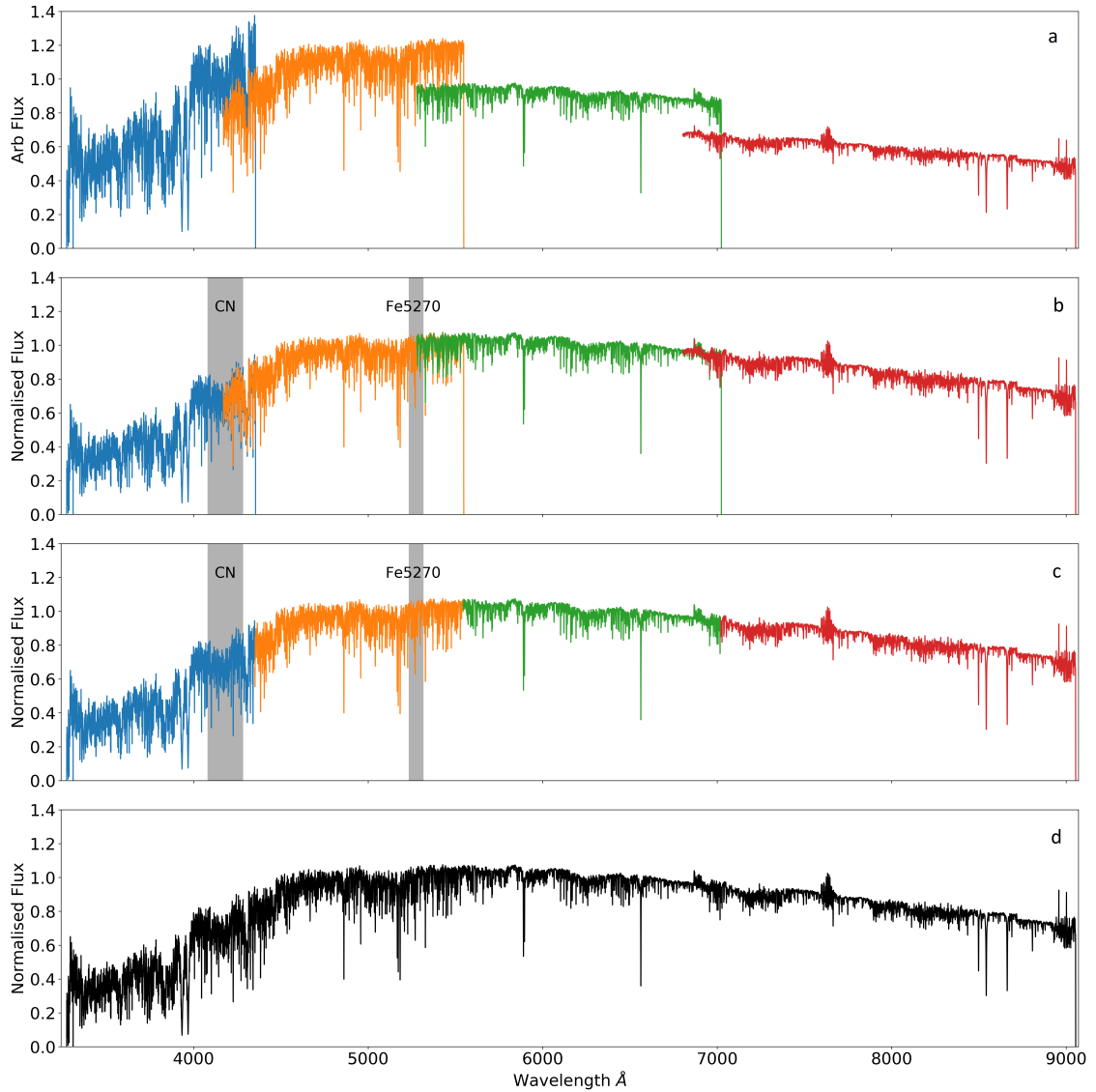


Figure 3.7: The four stages of combination of the gratings for NGC 104. First there is the flux conserved redshifted and regridded spectra for each grating (a). Then they are normalised (b), the overlaps are removed along with zero values (c) before full combination (d). Shown are the CN and Fe5270 indices and how they intercept some of the optional overlapping regions.

the 10 pixels removed from the other gratings spectra), this is then combined into one full spectrum ranging from $\sim 3273 - 9055\text{\AA}$ (Figure 3.7 d).

3.2.3 Error Spectra

Each file for each grating for all of the GCs had a 1σ uncertainty spectra attached to it which was calculated with the PyWiFeS pipeline (Usher et al. 2017). For more on the specifics of the PyWiFeS pipeline see Childress et al. (2014).

It was essential that for every action taken on the spectra, the exact same had to be performed on the error spectra as well. Therefore the error spectra were redshift adjusted and regridded to the same wavelength range and pixel width as the main spectra using the same method as stated in section 3.1. The error spectrum for each grating was then normalised so that the new values of uncertainty had the same proportion to the spectra as they did before the redshift adjustment and the regridding.

After this they were combined in the same way as before cutting off the last 10 pixels of each grating and removing the same overlap. Figure 3.8 shows the relationship between the uncertainty and the spectrum. At wavelengths lower than 4000\AA it is obvious the uncertainty increases rapidly, the data below this value is increasingly imprecise the lower one goes and this had to be factored in to the rest of the project.

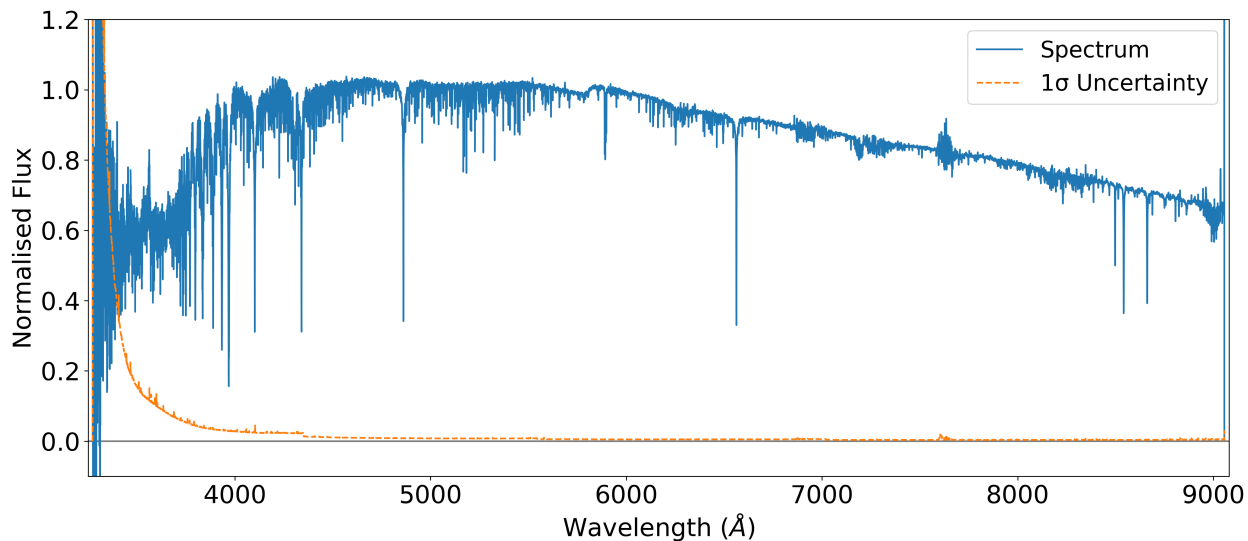


Figure 3.8: The fully combined spectrum of NGC 5694 along with its error spectrum. Note how at the lower wavelengths, uncertainty rapidly increases. The uncertainty increases in U7000 as is indicated by Table 3.1.

3.2.4 Omitted Globular Clusters

During initial analysis of the data it was decided that some globular cluster spectra were not suitable for the project. This was for multiple reasons described below.

The globular cluster Fornax 3 is a low metallicity ($[Fe/H] = -2.33$; Larsen, Brodie and Strader 2012), old (12 Gyr; de Boer and Fraser 2016), globular cluster located in the Fornax dwarf galaxy and has a mass of $10^{5.42} M_{\odot}$ (McLaughlin and van der Marel 2005). From the WAGGS sample Fornax 3 also has the largest heliocentric distance (137 Kpc; Usher et al. 2017) and would be a perfect candidate for the project, however the data from the WAGGS survey only had 3 of the 4 gratings needed for a full spectrum with the R7000 grating missing. The available gratings are enough to measure indices of particular interest such as the CN regions ($\sim 4100\text{\AA}$). But it was not appropriate for full spectral fitting, as the other spectra were measured between $3800 - 6000\text{\AA}$ which Fornax 3 data did not cover. It was for this reason it was omitted from this work.

Another globular cluster that has been omitted is NGC 2004 which is on the opposite scale to Fornax 3. NGC 2004 is a LMC GC which has a relatively high metallicity ($[Fe/H] = -0.58$; Niederhofer et al. 2015) for a globular cluster and is very young with an age of 20 Myr (Niederhofer et al. 2015). Its mass is also considerably smaller than that of most globular clusters but average for its extremely young age (McLaughlin and van der Marel 2005). At $10^{4.32} M_{\odot}$ (McLaughlin and van der Marel 2005) it is one of the lowest mass globular clusters in the sample. The problem for this globular cluster is the signal to noise ratio of the data is very small with the spectra having no discernible features. For this reason it has been omitted from the sample.

3.3 Additional Data

Additional stellar system data was obtained for comparison with the WAGGS globular cluster data presented in this thesis. The objective behind this was to find identifying features of globular clusters which could differentiate them from other stellar systems.

3.3.1 Galaxies -Trager

Absorption line strengths for 381 galaxy nuclei were obtained from the VizieR catalogue: Trager et al. (1998a). The galaxy spectra covered the range 4000-6400 Å and the spectra were observed at the LICK observatory using the Cassegrain Image Dissector Scanner spectrograph on the 3m Shane Telescope between 1972 and 1984. This galaxy data is relatively old and has a low resolution of about 9 Å FWHM, and a low signal to noise.

This data was in the LICK/IDS line indices, which needed to be converted to the LIS system (see Section 5.1). This was converted using the values for 8.4 Å resolution as these were galaxies (5 Å is used for smaller stellar systems i.e. globular clusters). The spectra are primarily of the centre of each galaxy and the low individual signal to noise caused a large spread in the data points and large uncertainties in the data which is shown in Figure 6.8.

3.3.2 M31 GCs -Schiavon

Over 300 globular clusters from Andromeda (M31) were obtained from Schiavon et al. (2012). The objective of this was to compare galactic GCs to the M31 ones looking to see similarities in the line indices which would indicate that globular clusters behave similarly regardless of parent galaxy.

The data came, much like the galaxy data from Trager et al. (1998b), as LICK indices. These were converted to the LIS system but using the 5 Å values for conversion because these were globular clusters. The data covered the wavelength range 3650-9200 Å and had a resolution of 5 Å (FWHM) with a median signal to noise of $\sim 75 \text{ pix}^{-1}$. The uncertainty values were less than the Trager galaxy data and equivalent to the WAGGS data. This data is plotted frequently in Section 6.2.

3.3.3 M87 GCs and UCDs

Using the Keck Cosmic Web Imager, Forbes et al. (2020) managed to observe the spectra of several globular clusters and Ultracompact Dwarf galaxies (UCDs) in the field of the elliptical galaxy M87.

The data came as a full spectrum not as line indices and it first needed to be de-

redshifted for which literature values of the redshift or recession velocity (from Forbes et al. 2020) were used following the same process outlined in Section 3.2.1. After this the LIS indices were measured (as in Section 5.1). The resolution of each spectrum was $\sim 5.06\text{\AA}$ which was equivalent to the 5\AA needed for the LIS system so no smoothing was needed. The uncertainty for each index was calculated in the same way as outlined in Section 5.2 via Monté Carlo simulations using a simple error spectrum created by calculating signal divided by the S/N value provided.

3.3.4 MODS Objects

Through Dr Mark Norris, spectra (and uncertainty per-pixel values) of five UCDs and ten compact elliptical galaxies (cEs) were obtained. These were mostly from MODS (The Multi-Object Double Spectrographs for the Large Binocular Telescope) and so had a resolution of 2.3\AA . The data came, much like the M87 GC data, as full flux calibrated spectra but in the range 2991-6698 \AA . The spectra needed redshift adjusting, the original plan was to use pPXF (see Section 4) to find the correct redshift value. However accurate fits were unable to be obtained due in part to incorrect alpha values and low signal to noise. Therefore redshift values had to be obtained from literature. Not all of the UCD candidates had published redshift values so estimates were used by aligning key absorption line features to their proper values (to within a threshold of $\pm 1\text{\AA}$). This is not a reliable method and was only used as a last resort. The LIS indices were then measured and uncertainties calculated by running Monté Carlo simulations in the same way as described in Section 5.2 using the provided uncertainty per-pixel spectrum.

3.3.5 SDSS Galaxy Bins

Thomas Davison provided binned galaxy spectra for several thousand galaxies produced from SDSS. He performed a linear binning on the galaxies according to a (unpublished) Voronoi diagram (Figure 3.9) of radius against mass where galaxies of similar size and mass were binned together. The binning creates a greater signal to noise ratio in the data (this caused less scatter in the results compared to the galaxy spectra from Trager et al. 1998b).

The spectra came already flux calibrated and redshift adjusted. There were two sets of data: one set had the central 12.5% of light of each galaxy in each bin contributing to the spectrum, the other used the inner 50% of light of each galaxy. The first sample came from

galaxies close enough that the inner 12.5% of the light was caught in the fibres, the second, much larger sample, was of more distant galaxies so 50% of their light was caught in the fibres. No uncertainty values were provided however. The SDSS spectra has a resolution of $\sim 2.95\text{\AA}$ FWHM, but since these were galaxies the velocity dispersion dictated the resolution for many of them. The velocity dispersions of each binned spectra were provided by Tom and any bin which had a velocity dispersion resulting in a resolution less than the SDSS resolution was smoothed to 8.4\AA from 2.95\AA . Bins which had velocity dispersions higher than 2.95\AA were smoothed to 8.4\AA from the resolution dictated by the velocity dispersion. 8.4\AA was chosen because the LIS system requires a resolution of 8.4 for small-mid mass galaxies which these were. The LIS indices were then measured (see Section 5.2).

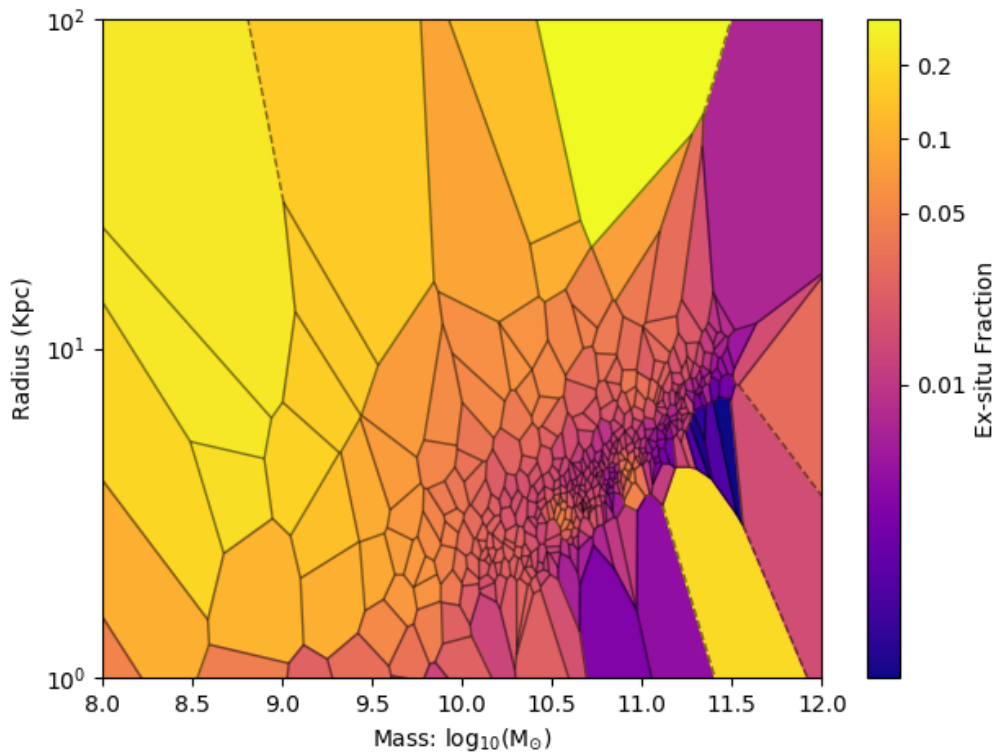


Figure 3.9: The Voronoi diagram showing the different bins used for the inner 12.5% of light galaxy sample and the fraction of ex-situ stars in the galaxies halo.

4|Fitting to SSP Models

As discussed earlier, globular clusters are not the pure single stellar populations (SSPs) originally thought. By comparison with single stellar population models it is the aim of this project to identify where the different populations of stars affect the integrated light of GCs. This is based on the assumption that the GC spectra consist of a combination of multiple single stellar populations each possessing a different single metallicity and age. In practice we expect the range of age and metallicity fit to a single GC to be limited as GCs do not display broad spreads in these properties. Each fit was performed via penalised pixel fitting of the integrated light spectra to SSP models via a package called pPXF (the method being undertaken in Python).

4.1 pPXF

The Penalised Pixel-Fitting (pPXF) method was first developed for IDL but has since been adapted for Python implementation. It was first created by Cappellari and Emsellem (2004) (but has been greatly improved upon since; Cappellari 2017) to extract the stellar or gas kinematics and stellar population information from galaxy spectra. It also has been successfully used for fitting to smaller stellar systems such as globular clusters (Boecker et al. 2020) as the fitting method is very general and robust.

pPXF can be used to extract galaxy kinematics such as radial velocity (V) and velocity dispersion (σ), it also produces a plot of the mass fraction in age-metallicity space (Figures 4.2, 4.3 & 4.4) which is based on the ratio of the weight of different SSP models used to produce an accurate fit. It should, however, be noted that due to the large number of input SSP files (often greater than 600 models) for each fit the solution may not be unique (ill-posed) and other SSP combinations may fit the spectra equally as well as the fit produced by

pPXF. pPXF uses regularisation to attempt to overcome this, details of which are in Section 4.3. Also only one set of models with the same $[\alpha/\text{Fe}]$ were used for each globular cluster to reduce the number of models being fit at any one time. This also had the effect of reducing the time it took pPXF to run.

The process adopts a maximum penalised likelihood approach to the fits based on an input noise spectrum. Galaxy spectra (of which pPXF was designed to operate on) generally fit well to Gaussian models (Cappellari and Emsellem 2004), pPXF automatically penalises non-Gaussian solutions which “reduces noise in the recovered kinematics” (Cappellari 2017). The maths behind which are quite complex and a full description of all the processes involved with accurately fitting the SSP models to spectra are presented in Cappellari (2017).

4.2 Single Stellar Population Models

Single Stellar Population Models are commonly based on a combination of stellar spectral and photometric libraries and theoretical isochrones and IMFs. Isochrones are curves on a Hertzsprung-Russell (HR) diagram which represent the stellar evolution of a population of stars based on parameters such as initial mass and chemical abundances. IMFs are the initial distribution of mass in a stellar system. In general IMFs follow a logarithmic power law where there are many low mass stars and fewer stars at higher masses (although some models such as Kroupa (2001) suggest that at very low masses [roughly $< 0.08 M_{\odot}$] the number of stars decreases again with a minimum mass of $0.01 M_{\odot}$).

4.2.1 MILES SSPs

Due to the large range in metallicity and age of the WAGGS GC sample and the wide wavelength range of the WiFeS spectra (3300 - 9050 Å), the SSP models chosen for the pPXF fitting were the MILES (Medium-resolution Isaac Newton Telescope Library of Empirical Spectra). This has a consistent resolution across its full wavelength range but does not cover the full WAGGS spectral range. This is not a problem, however, as the regions identified in Section 2.2.1 such as the CN region and the NaD line are covered in the MILES SSP range.

The MILES Spectral Library SSP models are based on code presented in Vazdekis et al. (2010) and the stellar libraries presented in Sánchez-Blázquez et al. (2006) & Cenarro

et al. (2007). They cover a wavelength range of $3540.5 - 7409.6 \text{ \AA}$ with a FWHM of 2.51 \AA . The pixel width ($\Delta\lambda$) is 0.9 (\AA) . The SSP models covered a wide range of metallicities (12 metallicity bins: $-2.27 \leq [M/H] \leq 0.4$) and ages (53 age bins: $00.03 - 14.00 \text{ Gyr}$) and has 3 options for $[\alpha/Fe]$ (“base”, $+0.00$ and $+0.40$). This meant that for each $[\alpha/Fe]$ value there were 636 separate SSP models. I used the BaSti Isochrone (Pietrinferni et al. 2004) and the IMF used is Kroupa universal (Kroupa 2001) which has a slope of 1.30.

As was stated in Section 2.2.1 globular clusters are mostly all enhanced in $[\alpha/Fe]$ (Brown and Wallerstein 1992). This α enhancement varies from cluster to cluster and in order to accurately fit observed spectra, pPXF needs models with age, $[M/H]$ and $[\alpha/Fe]$ values that cover the observational range. The MILES models, while they had a large range of ages and metallicities, only had two α abundances that could be used: 0.00 and 0.40. Through weighted linear combination of the 0.00 and 0.40 $[\alpha/Fe]$ models, three more sets of SSP models were created (Figure 4.1) with $[\alpha/Fe] = 0.10, 0.20,$ and 0.30 to help increase accuracy in the fits.

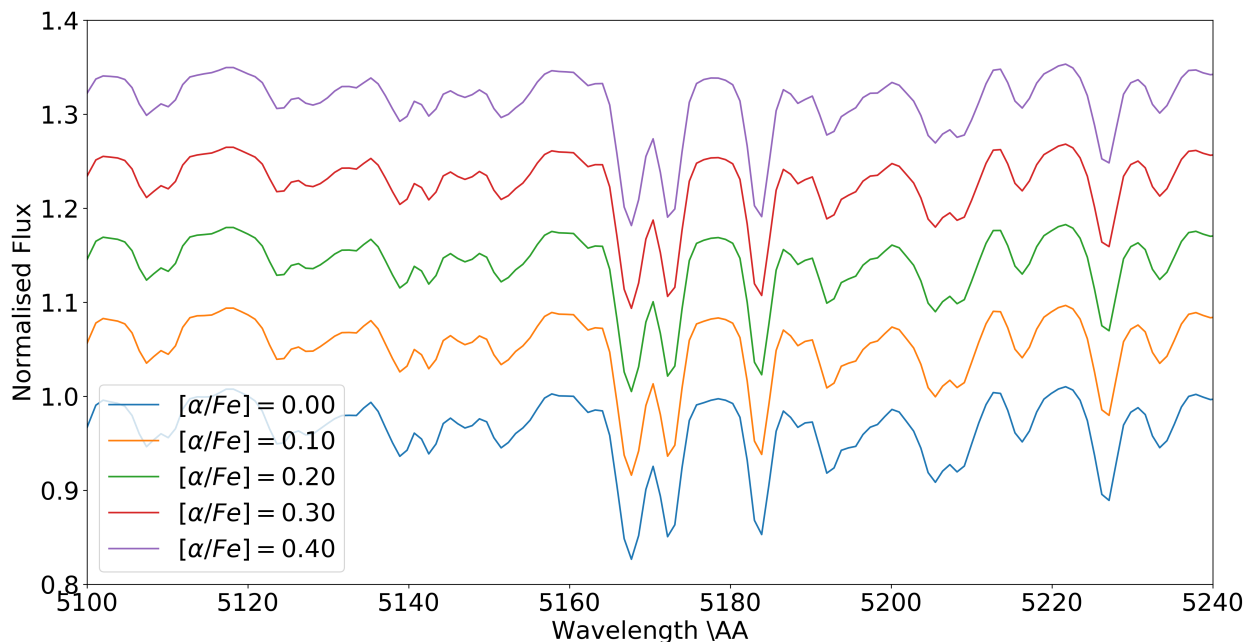


Figure 4.1: The new SSP models created from linear combination of the $[\alpha/Fe] = 0.00$ and 0.40 sets of MILES models with ranging $[\alpha/Fe]$ values, here covering Mg and Fe lines for a 10 Gyr model at $[M/H] = -1.49$. The models have been separated in the plot by addition of flux relative to their $[\alpha/Fe]$ value.

When fitting the models to the GC spectra only models with $[\alpha/Fe]$ values that were closest to the published values of each GC were used to reduce the effects of ill-posed fitting.

The values for each globular cluster fit are shown in Table 8.2 and only a handful of globular clusters have published $[\alpha/\text{Fe}]$ so truly reliable fits could only be done on those GCs.

4.2.2 Conroy

SSP spectra presented in Conroy et al. (2018) were acquired for comparison with the MILES models as well as for identifying potential regions to show elemental enhancements. This set of SSP models is considerably smaller with only 5 age bins (1, 3, 5, 9 and 13 Gyr) and 5 metallicity bins ($[\text{M}/\text{H}] = -1.5, -1.0, -0.5, 0.0$ and 0.2). However for each age and metallicity value there were spectra for eighteen differently chemically enhanced stellar populations (see Figure 6.2). Key amongst these enhancements, for this project, were C, N, and Na which were enhanced and depleted by ± 0.15 , ± 0.3 and ± 0.3 dex respectively.

These models showed exactly where the specific elements such as N and C affected a stellar spectrum and helped identify potential regions of interest and confirm already suspected absorption lines such as the CN region mentioned in Section 2.2.1. The Conroy models have a resolution of $\text{FWHM} = \sim 4.39\text{\AA}$ between 3700 and 7400 \AA . The full wavelength range of these models is 0.3500 to 24.9976 μm but after $\sim 7423\text{\AA}$ the resolution decreases.

4.3 Fitting Procedure

There are many input parameters for the pPXF package which effect how SSP models fit the spectra. The full list of which and examples of successful fitting procedures are available in the pPXF source files. In this section the processes and parameters used in the pPXF fits for this project are described.

The SSP models used had a resolution of $\text{FWHM} = 2.51\text{\AA}$ so the WAGGS spectra first had to be broadened to this resolution before fits could be attempted using the Python package “astropy”. Once this was complete the first fitting was set up. The SSP models and the spectra were cropped to an appropriate wavelength range. For the majority of fits the range selected was 3800 – 6000 \AA as this covered many of the regions discussed in Section 2 such as the CN region quoted to be an N sensitive region showing enhancements (e.g. Puzia et al. 2002 & Smolinski et al. 2011) and was within the wavelength range of the LICK/IDS system (see Section 5). It was found that larger regions increased running times considerably

(see below) and the area of focus was around the CN region, so having a larger region was not necessary. The region did need to have key lines which would obtain correct age and metallicity estimates such as the Fe5335 & Fe5270 lines and Mg_b , also, range selected covered the $H\beta$, $H\delta$ and $H\gamma$ lines which are strongly sensitive to age.

pPXF requires all input spectra and SSPs to be logarithmically re-binned before fitting. The 1σ error spectrum from the PyWiFeS pipeline (Childress et al. 2014) was used as a noise spectrum and the fitting process used this for a noise weighted fit. If data did not have an error spectrum pPXF did not use weighted bias while fitting. The input parameter “mdegree” represents a multiplicative Legendre polynomial which is used to correct the continuum shape during any fits. The correct degree of the multiplicative Legendre polynomial is determined by:

$$\lambda_{max} - \lambda_{min}/200\text{\AA} \quad (4.1)$$

The value of the denominator controls the minimum size of spectral features that are affected by the polynomial, in this case no spectral features narrower than 200\AA are affected, implementing this greatly increases run times for each fit. From Equation 4.1 the degree used for the wavelength range $3800 - 6000\text{\AA}$ was 11. If the wavelength range was increased to $3800 - 7400\text{\AA}$ (the max red end for MILES SSPs) the degree of the multiplicative Legendre polynomial increased to 19 which almost doubled the run time of each fit. There was also an additive Legendre polynomial which could be used to correct the template continuum shape during the fit but it was not used to reduce run times.

The fitting process relies heavily on the input noise. This, combined with the large sample size of SSP models means that getting an accurate model of the GC spectra is ill-posed and ill-conditioned. pPXF uses regularised least-squares minimisation to combat these effects. The fits presented in this thesis used second order regularisation where the regularisation parameter in the pPXF fit “regul” controls how much the weights of the models are smoothed out to find optimal fitting. This method is also able to produce age-metallicity distributions (such as Figure 4.4). Regularisation finds a compromise between the quality of the fit and the noise in the solution, with the ideal regularisation parameter (regul) being set to when $\Delta\chi^2 = \sqrt{2 \cdot N_{pix}}$ where $\Delta\chi^2$ is the change in the sum of the squared deviations and N_{pix} is the number of pixels that need to be fit (after the noise vector is re-scaled with an unregularised fit).

4.3.1 Example Fitting Procedure

For any GC spectrum, the process of fitting was the same. First, an unregularised fit is performed using the SSP models $[\alpha/\text{Fe}]$ interpolated to the value given in the literature (rounded to 0.0, 0.1, 0.2, 0.3 or 0.4) (Table 8.2). The noise vector needed too be re-scaled so that the reduced chi squared statistic (pp.chi2 in pPXF): $\chi^2/\text{DOF} \approx 1$ (where DOF is ‘degrees of freedom’ and is the number of pixels used in the fit) this is done by multiplying the noise spectrum by the square root of the current value for χ^2/DOF . After this the fits can be run until an optimal value for the regularisation parameter ‘regul’ is found where the output $\Delta\chi^2$ is within ~ 0.1 of the desired $\Delta\chi^2$ which is calculated by $\Delta\chi^2 = \sqrt{2 \cdot N_{\text{Pix}}}$ (with emission lines omitted from both the un-regularised and regularised fits). This then outputs a best fit spectrum plot and a mass fraction plot in age-metallicity space i.e. Figure 4.2

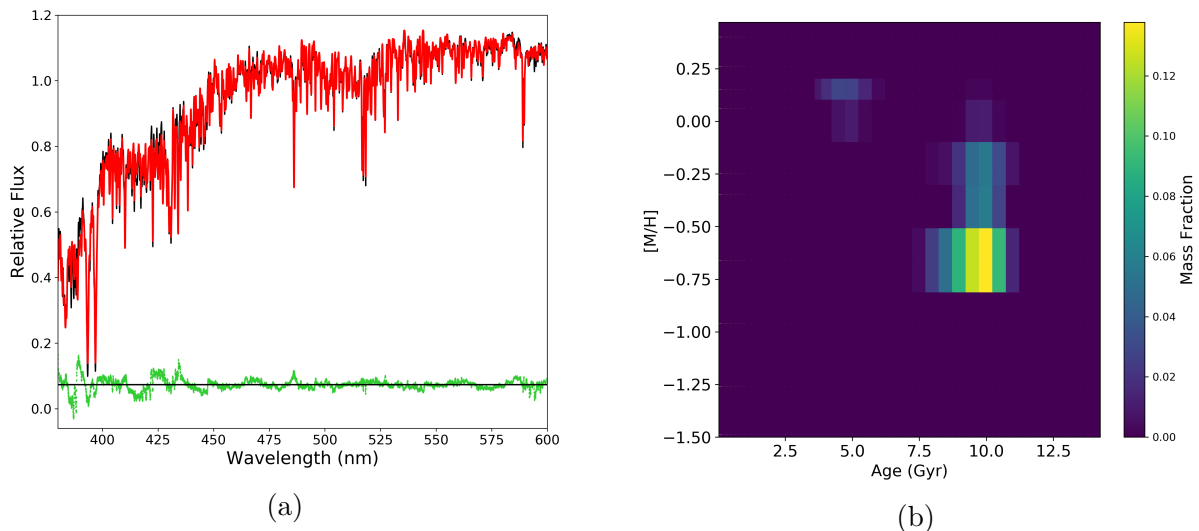


Figure 4.2: NGC 104 fit using 0.3 dex $[\alpha/\text{Fe}]$ enhanced MILES SSP models. In figure (a) the red line is the best fit spectrum, the black is the original spectrum and the green points are the residuals per pixel. Figure (b) is the mass fractions in age-metallicity space and shows 2 separate populations of stars one at 10 Gyr and $[\text{M}/\text{H}] \sim -0.6$ and a small younger and more metal rich population at 5 Gyr and $[\text{M}/\text{H}] \sim 0.15$.

4.3.2 Regions of interest

The procedure described in Section 4.3 was completed on all GCs with known $[\alpha/\text{Fe}]$ values looking for trends in poor fitting regions which were common in all of the globular clusters in the fit plots (i.e. Figure 4.2a). As was predicted, the CN region showed constantly poor fits

with the model continually underestimated the abundances of that region. The identified regions which showed consistently poor fits were then omitted and another fitting procedure was performed. This would then show the predicted abundances of that region based on the rest of the spectra and any differences seen would be purely because of enhancements. Figure 4.3a shows the omitted regions (grey areas) used for each fit and the ranges of which are in Table 8.1.

In Figure 4.3a going from lowest to highest wavelength (left to right) the first omitted region (R_1) covered the start of the spectrum to just past the Ca H&K lines, this region never fit well and is likely due to a combination of CN variations which have strong effects in the region (Smith and Norris 1993) and poor signal to noise in the U7000 grating data. The next region across (R_2) covered the CN region defined by the LIS system (Vazdekis et al. 2010) and a larger region outside the constraints of that system where the spectra were enhanced relative to the best fit SSP models. The last region (R_3) covered the last ~ 350 pixels and contained the NaD and He(5876Å) lines. Na is known to be enhanced in GCs with MPs and He spreads are known to be in the MS of some GCs (Bastian and Lardo 2018 & Milone 2014). After these regions were omitted, the mass fraction in age-metallicity space plot (Figure 4.3b) did not show the smaller young population of stellar mass that was present in Figure 4.2b, this is a good indicator that the signatures of multiple populations are in the omitted regions.

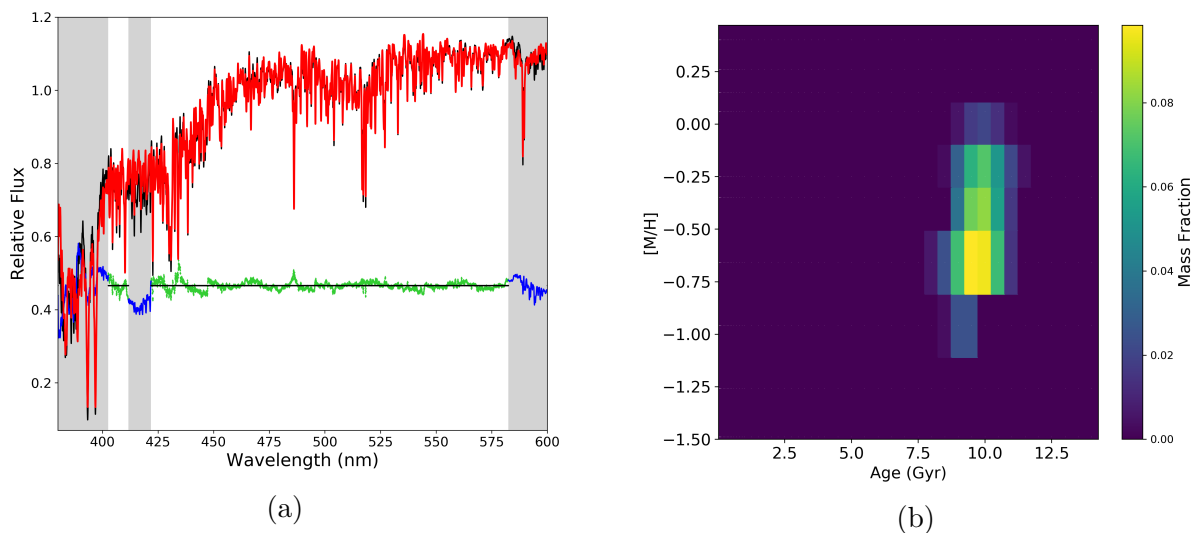


Figure 4.3: Similar to Figure 4.2 for NGC 104 but with the omitted regions of Table 8.1. Note how the mass fraction plot (b) now only has a single population compared to the apparent two in Figure 4.2b. From left to right, in plot (a), the omitted regions are R_1 , R_2 , R_3 in Table 8.1. R_2 & R_3 cover CN and NaD lines respectively.

4.3.3 Fit Comparison

Boecker et al. (2020) fit single stellar population models to the integrated MUSE spectrum of NGC 6715 (M54). They found a dominant old (8 - 14 Gyr) population and a smaller young metal rich population (see Figure 4.4a&b). For comparison they also fit the E-MILES SSP models to the WAGGS integrated light spectra for the same GC. WAGGS had a greater blue coverage than the MUSE data but the results as shown in Figure 4.4a&b, show good agreement with each other (except for an old and metal rich spread in the MUSE data which they say is due to the brightest stars in the GC, of which the origins are unsure).

By comparing the recovered fit in this project (Figure 4.4c) to the fit in their paper (Figure 4.4a) there is good agreement in age and metallicity and the mass distribution of the young, metal rich and older, metal poor populations. There is increased spread, however, in the mass weights of the fit shown in this thesis which could be due to slightly different wavelength ranges used and the different models used, MILES were used here, where they used E-MILES (an extended form of MILES).

4.3.4 Error calculations

To measure the accuracy of the fits, the error of the average age and metallicity values produced by the fit were measured. This was done by running Monté Carlo simulations. The PyWiFeS pipeline (Childress et al. 2014) produced a 1σ error spectrum for each GC spectrum. In the Monté Carlo simulation, each pixel of the error spectrum was multiplied by a random number drawn from a Gaussian curve distribution. The value of that pixel was then added to the corresponding pixel on the GC spectrum and a pPXF fit was run. This was repeated 100 times and the errors were calculated from the standard deviation of the outcomes. Due to the large amount of fits that needed to be done this took a very long time to run and so was only done for a few GCs where it was necessary to find accurate and precise age and metallicity values for comparison with literature values.

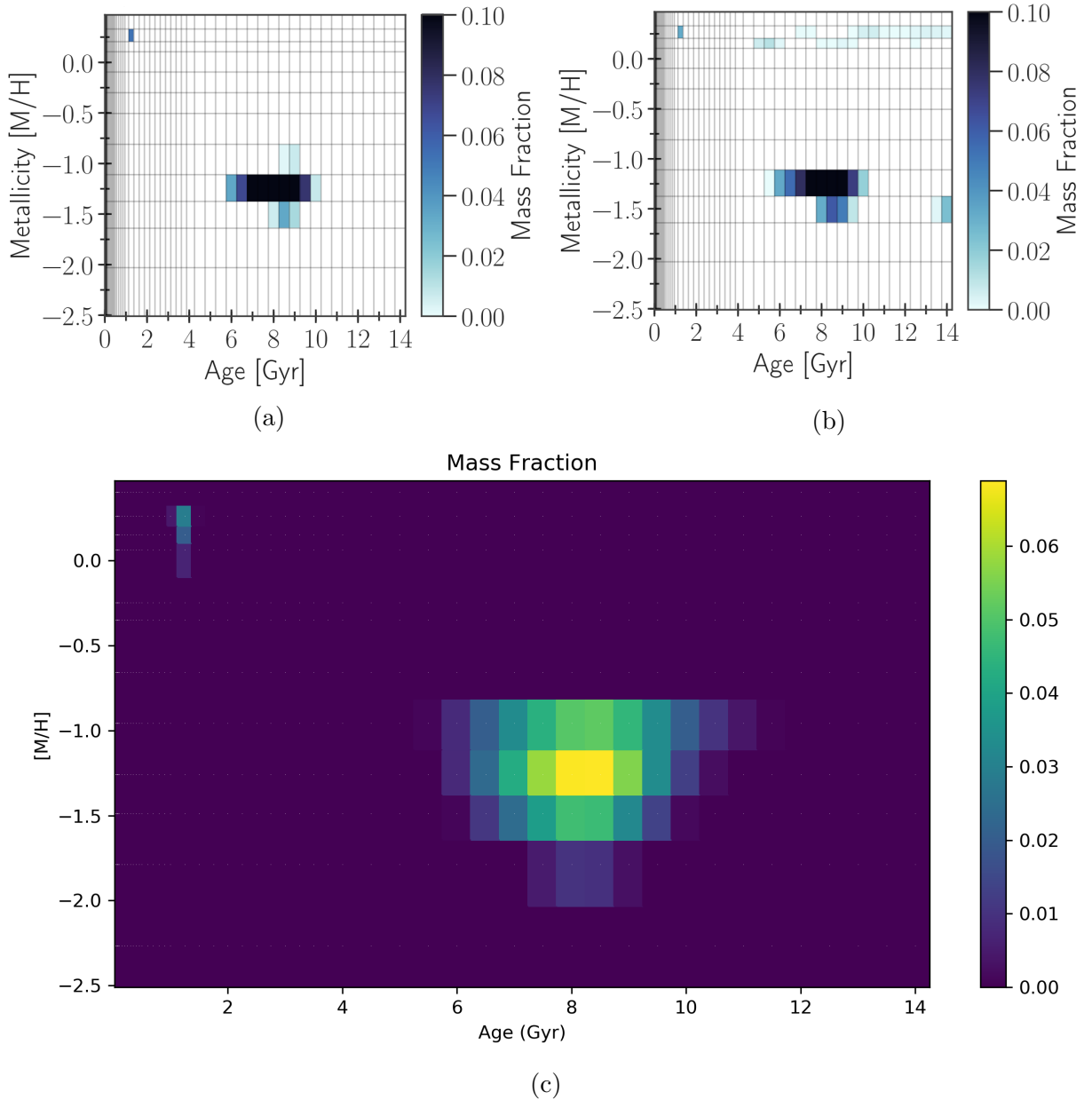


Figure 4.4: (a) and (b) are from Boecker et al. (2020) where (a) is the pPXF fit for the full WiFeS spectrum of NGC 6715 and (b) is the pPXF fit of the integrated MUSE spectrum (limited to the red WiFeS wavelength limit) using the E-MILES SSP models (Vazdekis et al. 2016) for both. (c) is the pPXF fit using the WiFeS data of NGC 6715 in this project fit to MILES SSPs (Vazdekis et al. 2010).

5|Measuring Indices

5.1 Line Index Systems

The next step was to quantify the abundance enhancements that had been detected using pPXF. This was done by measuring the strength of the absorption lines in the specific regions (indices) using the Python package PYPHOT which is a tool for computing synthetic photometry from spectra. It works by measuring the equivalent width or magnitude of a filter, which is a pre-defined region of a spectrum which corresponds to certain elemental absorption (or emission) lines.

A filter is defined by a blue and a red continuum either side of a central bandpass, a line representing the continuum is drawn between the central points of the blue and red bandpasses. The area between the continuum line and the line of the spectrum is measured and is presented as the size of the indices in either magnitudes or equivalent widths (EW). Figure 5.1 shows the blue, red and measured regions for the LICK/IDS index CN_1 and CN_2 .

5.1.1 LICK/IDS & LIS

For measuring the spectral indices in this project a line index system already in use was adopted. The LIS (Vazdekis et al. 2010) system was used, which is an updated version of the LICK/IDS system (Gorgas et al. 1993; Worthey et al. 1994; Worthey and Ottaviani 1997). Starting in 1993 Gorgas et al. derived “empirical fitting functions for 11 atomic and molecular features prominent in the spectra of G and K type stars”. This list of eleven absorption features was increased to 21 by Worthey et al. 1994 and again increased to include several hydrogen features in 1997 (Worthey and Ottaviani 1997). The LICK indices provided by the PYPHOT package number 49 and cover a wavelength range of 3696.3Å (in the blue

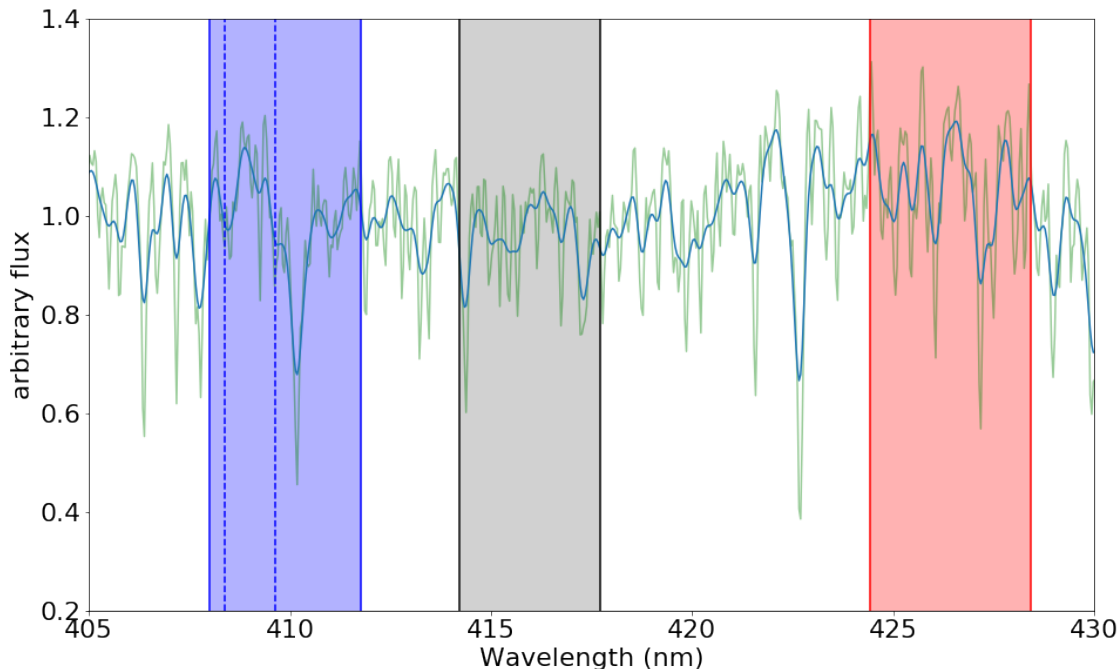


Figure 5.1: CN_1 and CN_2 LICK indices shown on $FWHM = 0.8$ (green) and smoothed $FWHM = 2.51$ (blue) WAGGS spectra for NGC 104. CN_2 is only different from CN_1 by the different blue continuum (blue shaded bar) which omits the $H\delta$ line making it potentially more useful for stellar populations with hot stars (Worthey et al. 1994). The red shaded bar marks the red continuum while the grey shaded area is the measured region.

continuum for the LICK indices “OII EW”) to 8725\AA (in the red continuum for LICK indices “ $Ca3_{LB13}$ ”).

The LIS system was proposed in 2010 by Vazdekis et al. 2010 which was designed to avoid intrinsic errors in the previous system but still used the same indices. The previous system had resolutions which varied with wavelength, where now the resolution could be constant across the full spectrum. The spectra can be measured at three different resolutions: 5, 8.4 and 14\AA (FWHM). 5\AA is most appropriate for stellar clusters and dwarf galaxies, 8.4\AA is for low to intermediate mass galaxies where the velocity dispersion starts to dominate the resolution of the spectra and 14\AA is reserved for only the most massive galaxies which have very large velocity dispersions. It should be noted that LIS does not have to be restricted strictly to the LICK indices and other index systems can be used, but the LICK indices were used in this project as they were already provided in the PYPHOT package and there was published conversion calculations for other LICK indices previously published such as the galaxy indices from Trager et al. 1998b (see Figure 6.8).

Vazdekis et al. 2010 also provided conversion tables which could convert indices pre-

viously measured on the LICK/IDS system to the new LIS system. The system used for the results presented in this thesis are from LIS and data that has been converted to LIS. For the full table of indices in the line index system used see Table [8.3](#).

5.2 Measurements

Each globular cluster in the sample provided by WAGGS (excluding NGC 2004 as mentioned in Section [3.2.4](#), Fornax 3 was used for this method as it had enough data for the regions that were being studied) had all available indices on the LIS system measured using PYPHOT. Because they were globular clusters they only needed to be reduced to a resolution of 5 Å after which a simple looping procedure in Python (that was written for this thesis) measured the indices for each globular cluster.

There were no up to date published errors for the measurement indices since the LIS system overwrote the errors of the old LICK/IDS system. The way uncertainties were calculated for the measured indices was via Monté Carlo simulations. The 1σ errors provided by the PyWiFeS pipeline (Childress et al. [2014](#)) were used in a similar method to that defined in Section [4.3.4](#).

5.3 Offsets from Literature

To make sure the results from this work were accurate relative to other published works an offset between the measurements from this work and those published in Kim et al. ([2016](#)) was created.

5.3.1 Current Published Works

Kim et al. ([2016](#)) combined LICK indices for the integrated light of 53 globular clusters from 3 separate works including their own (Puzia et al. [2002](#) & Schiavon et al. [2005](#)) which they also converted onto the LIS system. In their work they obtained spectra for 24 galactic GCs with a resolution of $\sim 2.0\text{\AA}$ FWHM using the drift scanning technique mentioned in Section [3.1.2](#). In the case of Kim et al. ([2016](#)), drift scanning caused lower signal to noise (than

WAGGS data) by having a shorter exposure time over the core of the GC meaning less light was captured. Schiavon et al. (2005) and Puzia et al. (2002) also used drift scanning.

The problem with combining three separate surveys of integrated GC light is that the area of light for each GC captured was not the same for each survey, meaning due to the stochasticity of the stellar distribution in the GCs the integrated light spectra for the same GC could vary significantly from survey to survey. Kim overcame this by only using their data to supplement the data of the previous studies. Kim, however, calibrated their data to the previous studies at which point the stochastic effects previously mentioned may have had an effect.

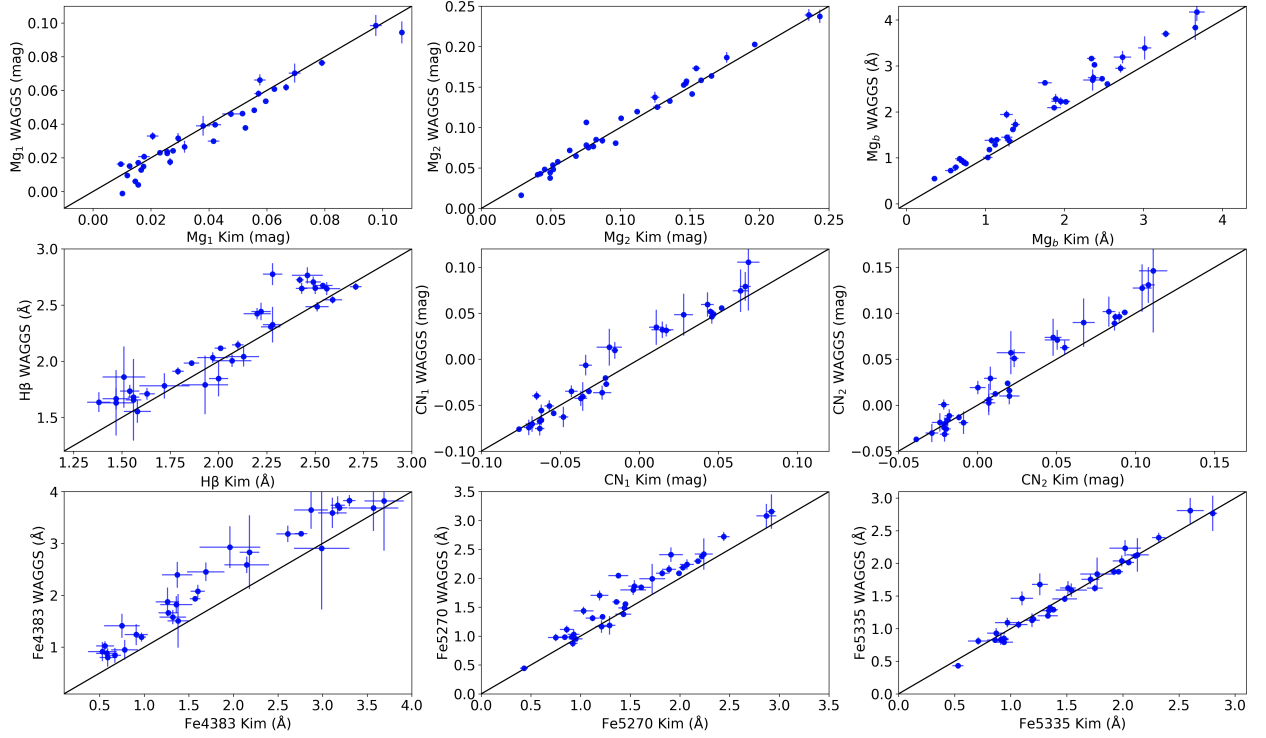
5.3.2 Offset Calculation

In this project, the indices are scaled by removing an offset calculated by the mean difference between the indices of this project to those published in Kim et al. (2016) (and therefore Puzia et al. 2002 & Schiavon et al. 2005). This is equivalent to applying the ‘‘LICK offsets’’ used to put measurements onto the LICK/IDS system (as Kim did).

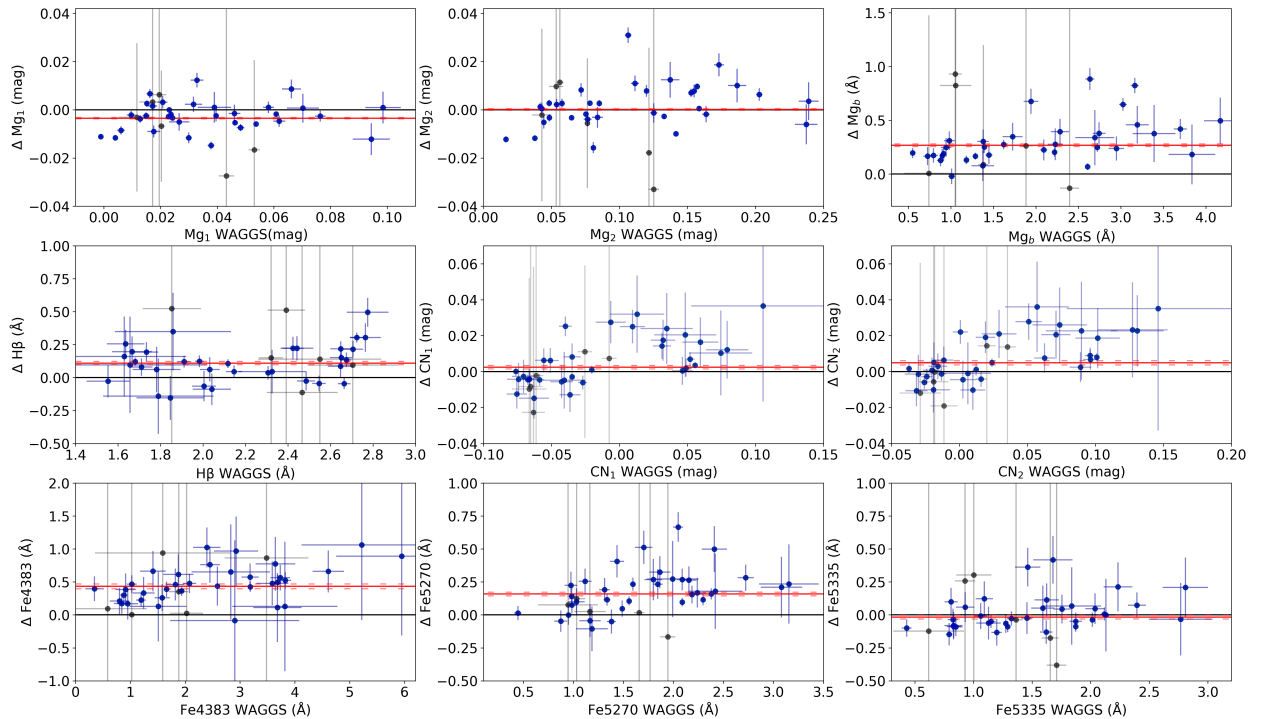
Kim et al. (2016) only released values for 20 indices, in this thesis offsets are calculated for nineteen (Table 5.1). The one that is missing is ‘C₂4668’ which is not in the LICK index library used by PYPHOT. Figure 5.2a shows the relation between 35 matching globular clusters between the WAGGS GCs presented in this project and those compiled by Kim. The plots show agreement between this project’s results and those of Kim et al. (2016) but with a considerable amount of scatter with some indices having significant offsets. To scale the indices the offsets were calculated (which would be added to the data for future plots such as in Figure 5.2b). This was done by first removing 3σ outliers from the residuals (residuals being the WAGGS value minus the Kim value). There was also Kim data which had large uncertainties for all indices, these were removed from the calculation (except for Fe5015 and Fe4531 where no data was available other than Kim’s). The error-weighted mean of the residuals for each index was calculated and is shown in Figure 5.2b as the red solid line via the equation:

$$\bar{x} = \frac{\sum_i w_i x_i}{\sum_i w_i} \quad (5.1)$$

5.3.2. Offset Calculation



(a)



(b)

Figure 5.2: (a) Is the plot of WAGGS against Kim (for 35 GCs in 9 of the LICK indices) which showed the initial offset between the two index libraries. (b) Is the residuals plot of WAGGS-Kim against WAGGS, the red line represents the mean offset and the red dashed lines are the calculated uncertainty.

\bar{x} is the mean residual offset, $\sum_i w_i x_i$ is the sum of the weighted residual values and $\sum_i w_i$ is the sum of the weights which are by design equal to 1. The uncertainties of the initial residuals were calculated by simple error propagation of the two values from the WAGGS and Kim indices errors. The uncertainty in the offsets was calculated by summation in quadrature of the uncertainties of the error-weighted residual values.

Table 5.1: Table of Indices Offsets.

Index	Unit	Mean	Uncertainty
CN ₁	mag	0.00242	0.00097
CN ₂	mag	0.00489	0.00117
Ca4227	EW	0.0814	0.0167
G4300	EW	0.4436	0.0314
Fe4383	EW	0.4329	0.0353
Ca4455	EW	0.1831	0.0161
Fe4531	EW	0.2468	0.8963
H β	EW	0.1102	0.0128
Fe5015	EW	0.2321	1.1429
Mg ₁	mag	-0.00349	0.00030
Mg ₂	mag	0.00016	0.00033
Mg _b	EW	0.2667	0.0125
Fe5270	EW	0.1586	0.0137
Fe5335	EW	-0.0163	0.0155
Fe5406	EW	-0.0528	0.0115
H δ_A	EW	0.2740	0.0350
H γ_A	EW	-0.0002	0.0324
H δ_F	EW	0.2356	0.0236
H γ_F	EW	0.0197	0.0203

5.3.3 Thomas SSP Models

Another set of single stellar population models, different to those listed in Section 4, were from Thomas, Maraston and Johansson (2011). These models are not in the form of a spectrum like the other SSPs but they came as absorption-line indices from the LICK system which first had to be converted to LIS absorption-line indices. These models have the same resolution of the MILES models (2.51 Å at FWHM) but were smoothed before measuring to the required resolution of the LICK index system. They have 20 age bins which cover a range of 0.1 - 15 Gyr and 6 metallicity bins in the range $[M/H] = -2.25 - 0.67$. These models also had variations in $[\alpha/Fe]$: -0.3, 0.0, 0.3 and 0.5.

The key importance of these models is that they also had chemical abundance variations

for C, N, Mg, Na, Si, Ca, Ti, Cr and Fe. Of which $N = +0.3$ dex has been used in this project to try to show N enhancement in the absorption line index of the GCs (Section 6.2) as Thomas et al. states the CN indices are very sensitive to N abundance (Thomas, Maraston and Johansson 2011). The models which had specific chemical enhancements did not have alpha enhancement equivalents as the solar abundance models did. The chemically enhanced models were enhanced relative to solar alone.

6|Signatures of Multiple Populations

6.1 Single Stellar Population Fitting

To get reliable accurate fits using the MILES SSP models, the $[\alpha/\text{Fe}]$ value for each GC needed to be known. This could be calculated from line index measurements but this is subject to scaling and flux calibration issues and would not be immediately comparable to literature values. Therefore only GCs with published values of $[\alpha/\text{Fe}]$ were used in the fits, other GCs had their α values estimated by the goodness of fit of the Mg $_{1,2,b}$ and Fe5270 absorption lines. Mg is an enhanced element in many secondary populations and there was also often poor fits and over estimation of the Mg lines for GCs with known α abundances, however, so this method was not overly reliable.

There was one region which, when omitted from the fit, showed poor fitting and also showed poor fitting in many GCs without the need for omitting the region from the fit beforehand. Defined in this thesis as R_2 it covers the CN LICK index and a broader area around it. The parameters of the omitted regions are in Table 8.1. R_2 is shown as the central grey area in Figure 6.1, the GC spectra is severely under-sampled by the best fit model showing that the elements in this region are enhanced compared to what a single stellar population predicts the spectra should look like.

This region is a known CN dominated region and looking at the residual spectra of Conroy enhanced to solar abundance models (i.e. Figure 6.2) shows that the full extent of R_2 is influenced by both C and N. As is mentioned multiple times in Section 2, Bastian and Lardo (2018) state that C and N are anti-correlated in multiple populations with the N being enhanced in the secondary population and C being relatively depleted.

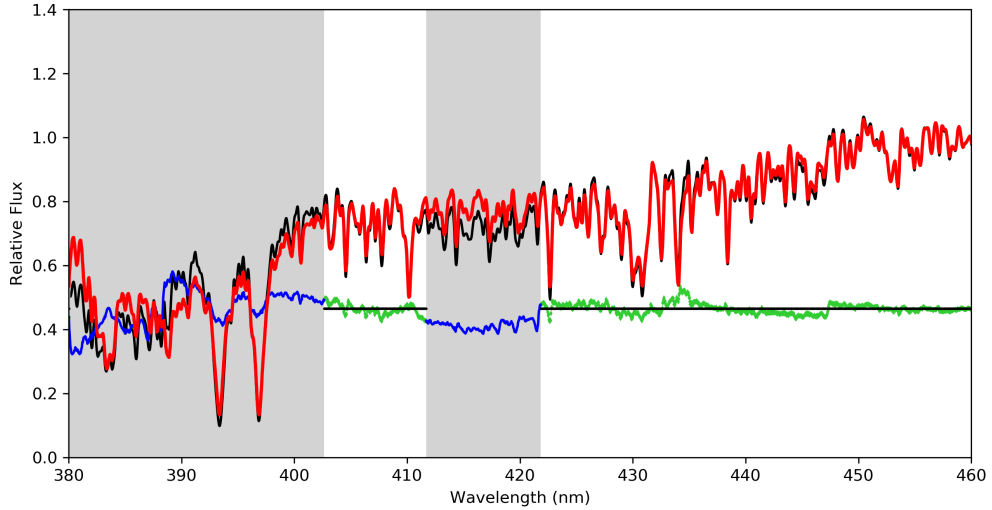


Figure 6.1: NGC 104 best fit with $[\alpha/\text{Fe}]=0.3$ dex MILES models (Vazdekis et al. 2010). The red line is the best fit model, the black is the WAGGS spectra (Usher et al. 2017), the green line is the residuals of the pixels which contributed to the fit, the grey areas are regions omitted from the fit (here R_1 [left] & R_2 [right] are shown from Table 8.1) with the blue line being the residuals of the unfit regions.

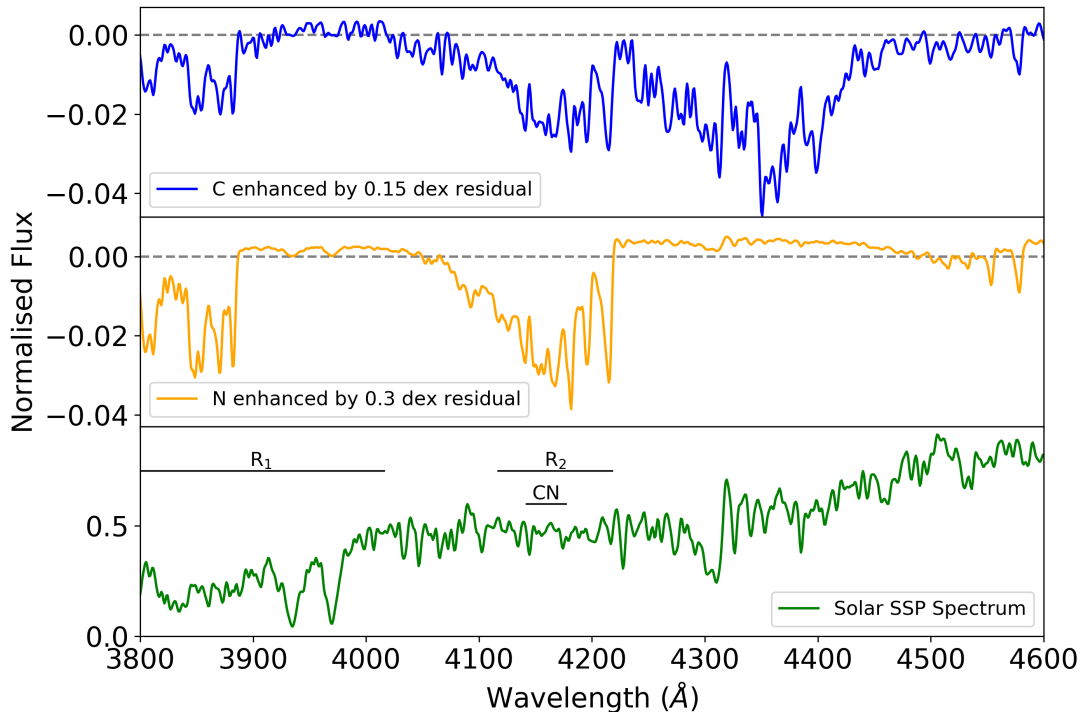


Figure 6.2: Conroy et al. (2018) SSP 13 Gyr & $[M/H] = -0.5$ models. From top to bottom: the residuals between the C enhanced model and the Solar model, the residuals between the N enhanced model and the Solar model, and lastly the Solar abundance level model for reference. Shown in the bottom plot are the R_1 & R_2 regions as well as the LICK CN region.

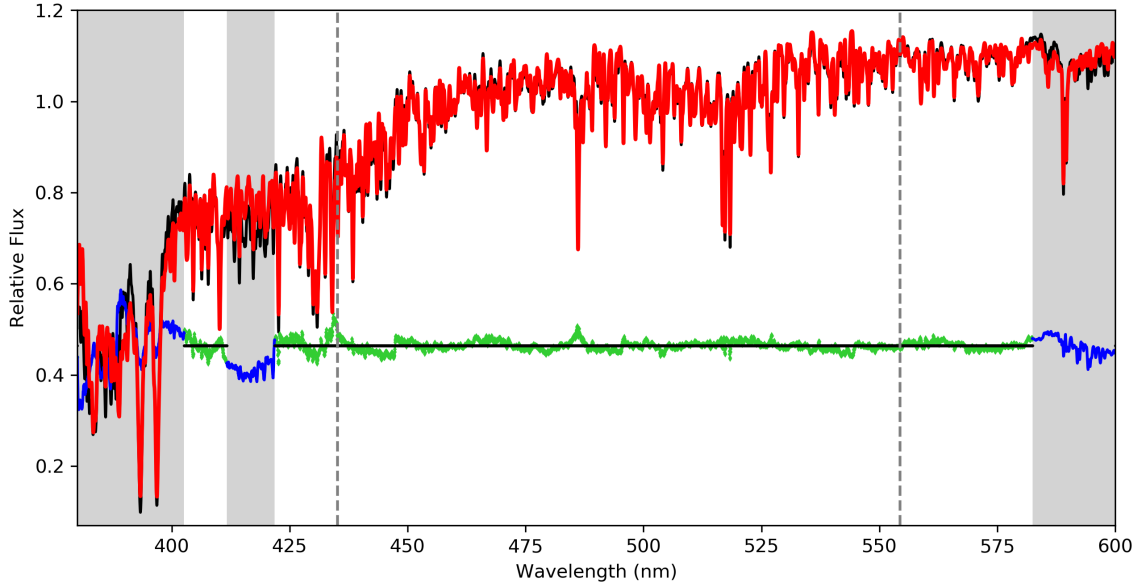
Figure 6.2 suggests that if C variations are causing an effect on the integrated spectra, continuous poor fitting should be seen between 4200 Å and 4450 Å. It was common to see some oversampling of the fit in this region (as is seen around the H γ line at 434 nm in Figure 6.1) hinting that there is C depletion here, but the effects of this were not always apparent in the spectra, whereas under-sampled fitting was consistent in R₂. In Figure 6.2 for R₂, both C and N are shown to effect the spectra. Since C is anti correlated to N in MPs and is relatively depleted (Bastian and Lardo 2018), the combined effect of both C and N variations would have opposing effects on each other. This is not the apparent case as there is clearly enhancement in the region. This supports the idea that the CN region (and the larger R₂ region) are dominated by N, and C plays very little part for the elemental variations observed in that region as is suggested by Thomas, Maraston and Johansson (2011) and by Bastian and Lardo (2018).

Fitting the Conroy SSP models to WAGGS GC spectra was not very beneficial. Due to the small number of models, the fitting process was not very accurate. One element fits with the Conroy data did show, is that when models enhanced in nitrogen are used instead of Solar the LICK CN region fits with a smaller total residual over the region. This is expected however as Figure 6.2 clearly shows that the N is enhanced in CN for Conroy et al. N+ models. The best fit model still shows under-sampling for many GCs which could indicate that the C also needs to be enhanced (unlikely due to the N-C anti-correlation) or that the model's N enhancement is not great enough. Also these models do not have variable α abundances (unlike MILES) so poor fits on the rest of the spectrum were very common (especially in magnesium).

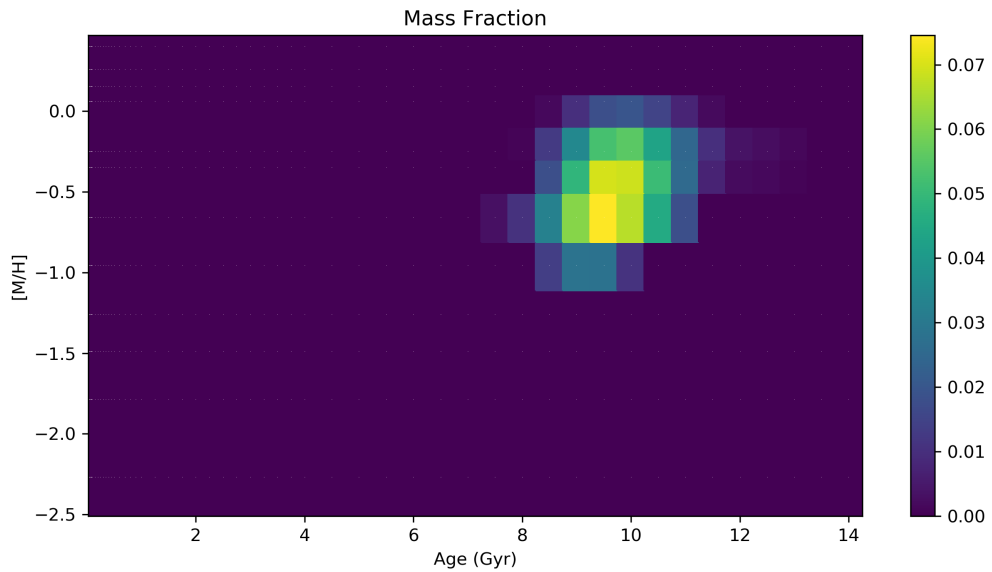
6.1.1 Other Poor Fitting Regions

It should be noted that both Boecker et al. (2020) and this project finds over-prediction of magnesium in the fit for NGC 6715 (~ 520 nm in Figure 6.3a). They suggest this is due to incorrect literature alpha values for NGC 6715. However, Mg is poorly fit in many of the GCs in the WAGGS sample when fit with SSP models but not always the same over-prediction as NGC 6715 exhibits, many GCs appear to be Mg-enriched while others are depleted. This may be due, as Boecker et al. (2020) state, to incorrect alpha abundance values being used in the models. But Bastian and Lardo (2018) state that Mg should be enhanced for some GCs with a possible anti-correlation to Al or Si. There are, however, no absorption lines or LICK indices in the wavelength range used which could measure Al or Si which would potentially

show that the poor Mg fitting is due to abundance variations in a secondary population (as would be the case if an anti correlation were detected) not just unreliable alpha abundance values, so the solution to this is still uncertain.



(a)



(b)

Figure 6.3: Same as Figure 4.3. Plot (a) is the pPXF fit of NGC 104 using $[\alpha/\text{Fe}] = 0.3$ dex MILES SSP models with the residuals plotted 0.47 (relative flux) above zero to keep more detail in the plot. The dashed lines represent where the spectrum transitions from one grating to another. Plot (b) is the weights of the SSPs used to make the best fit. The fit suggests an age of 9.46 ± 0.03 Gyr and a metallicity of $[\text{M}/\text{H}] = -0.449 \pm 0.001$ dex. Compared to the literature: 12.75 Gyr and -0.438 dex respectively (Table 8.2).

Smolinski et al. (2011) state there is a CN enhanced region at $\sim 3883\text{\AA}$ of which the Conroy models (Conroy et al. 2018) agree (see Figure 6.2). In some of the MILES GC fits this region does show significant enhancements (relative to the best fit SSP model). Unfortunately the WAGGS data has poor signal to noise at these low wavelengths which often cause the fit to be very poor in these regions. Figure 6.1 & 6.3a (for the full fit range) is an example of better than normal fitting of this region due to the signal to noise of U7000 being relatively large for NGC 104. The poor fitting may have affected the rest of the fit in unforeseen ways so it was decided to omit all data below 4016\AA (i.e. R_1). This did remove the Ca H&K lines from the fit however which are important for $[M/H]$ measurement but there were other key metallicity lines in the fit (such as Fe and Mg lines) which accounted for this.

Previous studies have recently investigated Na enhancement in secondary populations of globular clusters (e.g. Colucci, Bernstein and McWilliam 2017 & Larsen, Brodie and Strader 2017) and found evidence of Na spreads in the integrated light spectra. But, NaD can be quite problematic in spectra as it can be strongly influenced by ISM effects (Murga et al. 2015) and the IMF of the system (Boecker et al. 2020). The NaD line was in the wavelength range and was omitted from the fits (in the region: R_3). This region did not fit well to the best fit model for all of the globular clusters. Na is known to be an enhanced element in secondary populations (Bastian and Lardo 2018) so this poor fitting was expected and could be another key to signatures of MPs in globular clusters. This thesis, however, chose to focus on the CN absorption features due to the unpredictability of the NaD line.

The variation in the residuals for the WAGGS spectra (i.e. Figures 6.1 & 6.3a) is negligible to the thesis. This is due to the extremely high signal to noise of the data. The uncertainties for parameters like age were calculated via Monté Carlo simulations (i.e. Section 4.3.4). The same Monté Carlo simulations, however, lead to remarkably similar fits. Because of this, the uncertainty is too small to be presented in the plot. For example in Figure 6.3a for NGC 104, at 3800\AA the uncertainty in the residuals is 0.0059 (relative flux), but this rapidly drops so that at 4000\AA the uncertainty is 0.0018 (relative flux) and continues dropping so that at 4500 the residual uncertainty is 0.0010 (relative flux).

6.2 Line Index systems

6.2.1 Alpha Insensitive Metallicity Index

For all plots in this section which represent the LIS index values measured, the y-axis is the variable which is intended to show the chemical abundance variations of the multiple populations and the x-axis uses an index called $[MgFe]'$. $[MgFe]'$ is an estimator of stellar metallicity made from the LIS Indices Mg_b , $Fe5270$ & $Fe5335$ which are measured in angstroms (\AA). It is calculated by Equation 6.1:

$$[MgFe]' \equiv \sqrt{Mg_b(0.72 \cdot Fe5270 + 0.28 \cdot Fe5335)} \quad (6.1)$$

Globular clusters are known to be alpha enhanced to varying degrees (Bastian and Lardo 2018). In order to show metallicity, an alpha insensitive measure for metallicity was greatly needed for this project. González (1993) proposed the creation of such a measure which was refined by Thomas, Maraston and Bender (2003). This index is based on one assumption, that abundance patterns in stellar populations are described only by $[Fe/H]$ and $[\alpha/Fe]$ which is not strictly true as other element variations may influence the overall $[M/H]$. However for the case of globular clusters, where $[\alpha/Fe]$ varies from cluster to cluster, having an alpha insensitive metallicity scale allows comparison between GCs without worry of surreptitious effects on the metallicity values from different alpha enhancements.

6.2.2 Globular Clusters

Figure 6.4 shows that at higher metallicities the CN index, measured for our GC sample, is enhanced relative to the α enhanced model from Thomas, Maraston and Johansson (2011). This plot has had the residuals (calculated in Section 5.3) removed to make it on the same scale as other published indices, of which the Thomas models are also scaled. It is encouraging to see that the younger globular clusters lie where we expect them to be on the SSP models. This indicates that the models are correct for younger ages (except for 2 young metal rich GCs which appear to be older and more metal poor than they should be which could be due to age-metallicity degeneracy). Their positions on the plot also possibly show that the younger globular clusters do not possess CN enhancements, although from this plot it is difficult to show that younger GCs do not have CN enhancements.

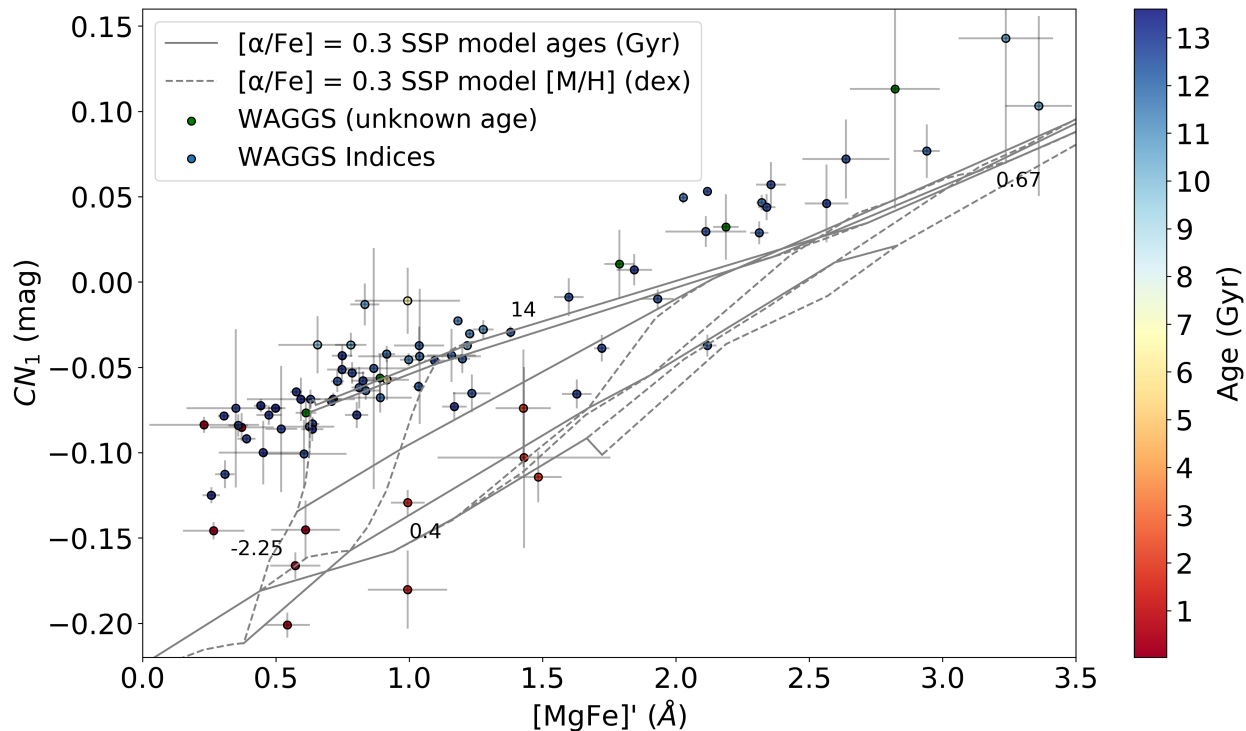


Figure 6.4: CN_1 against $[MgFe]'$ with an alpha enhanced SSP model from Thomas, Maraston and Johansson (2011) plotted with age represented in the colour chart. The metallicity values of the models are -2.25, -1.35, -0.33, 0, 0.35 & 0.67 (dex) and the age values are 0.4, 1, 4, 8 & 14 (Gyr).

The most promising GCs for multiple population signatures are the group with $[MgFe]'$ values larger than $\sim 1.7\text{\AA}$, which show clear enhancements over the model. Thomas, Maraston and Johansson (2011) state (and the findings of this work suggest) that the CN region is dominated more by N than C so the assumption is this is N enhancement. Scatter in the enhanced GC sequence may be due to different N enhancements in secondary populations of one GC to another, it may also be due to different mass fractions of secondary populations to the first population in any given GC. But the key finding here is that the integrated light of GCs appears to be enhanced in CN.

Figure 6.5 is much the same as Figure 6.4 but instead shows CN_2 (the difference being that CN_2 does not have the $H\delta$ absorption line in the blue continuum). The plot of CN_2 shows the same enhancements at higher metallicity as the CN_1 plot (Figure 6.4). This plot however also presents globular cluster indices from M31 published by Schiavon et al. (2012). There is strong agreement between the Milky Way GCs and those of Andromeda and they both show the enhancements at higher metallicities. M31 has more metal rich GCs than the Milky Way (Cezario et al. 2012). This can be seen in the figure, but these more metal rich

GCs still follow the same enhanced sequence over the model.

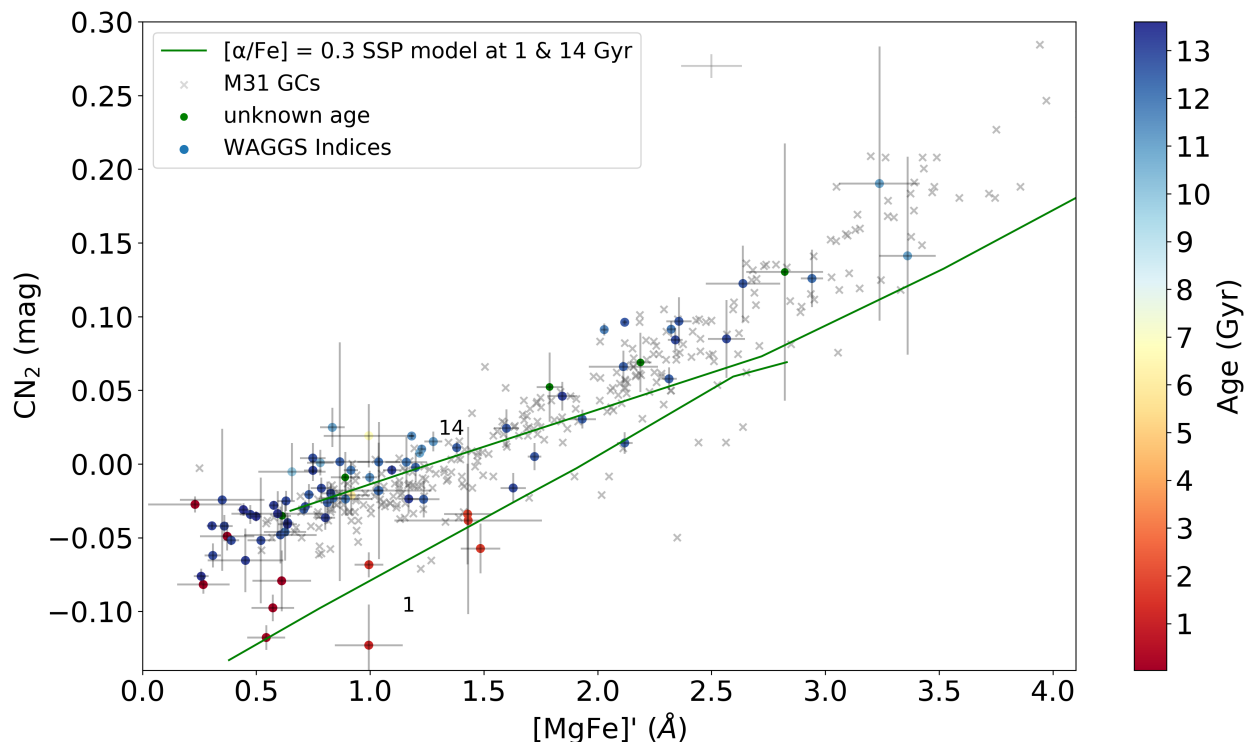


Figure 6.5: CN_2 against $[MgFe]'$ for 85 GCs with an alpha enhanced SSP model from Thomas, Maraston and Johansson (2011), with M31 globular cluster data from Schiavon et al. (2012) and plotted with age represented in the colour chart.

Using the Thomas, Maraston and Johansson (2011) LIS indices for SSPs enhanced in Nitrogen by +0.3 dex in the CN_1 plot we get Figure 6.6. This plot shows that the models with enhanced nitrogen match the globular cluster sequence much more closely compared to the models which only have +0.3 alpha enhancement. This is another strong indicator that there is evidence of the nitrogen enhancement present in multiple populations in the integrated light spectra of globular clusters.

At higher metallicities it is apparent the CN band shows more enhancement than even the N enhanced model suggests. This is likely due to the model not having sufficiently high enhancement even for high metallicities (i.e. +0.3 is too low of an enhancement for some high metallicity GCs).

The main problem with these plots is that it is impossible to distinguish N enhancement in lower metallicity GCs. This is because in lower metallicity GCs there are, by definition, fewer metals so there is less N to show enhancement. This is a potential issue

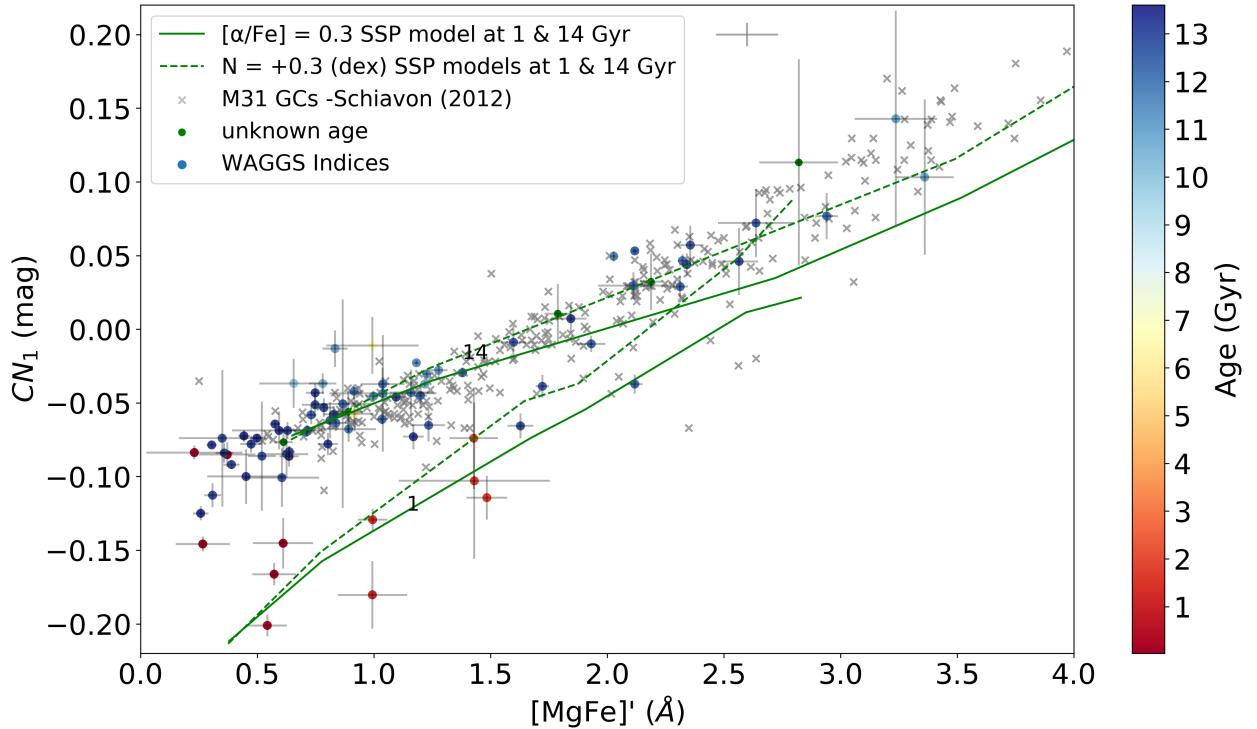


Figure 6.6: Same as Figure 6.4 (with CN_1) and 6.5 (with M31 GCs from Schiavon et al. 2012) but with the alpha enhanced model and nitrogen enhanced models of Thomas, Maraston and Johansson (2011).

of the spectroscopic indices method and only more sensitive, higher resolution spectra and stellar population models can help solve it.

6.2.3 Extragalactic Stellar Systems

Secondary data was found for other stellar systems (described in Section 3.3). This data was used to compare against globular clusters with the aim of finding a probe for differentiating extragalactic globular clusters from UCDs and other stellar systems.

In Figure 6.7 the measured LIS indices of several types of stellar system are added to Figure 6.6. Compact elliptical galaxies (cEs) and ultra-compact dwarf galaxies (UCDs) given by Dr Mark Norris as well as some GCs and UCDs from M87 (Forbes et al. 2020) are plotted.

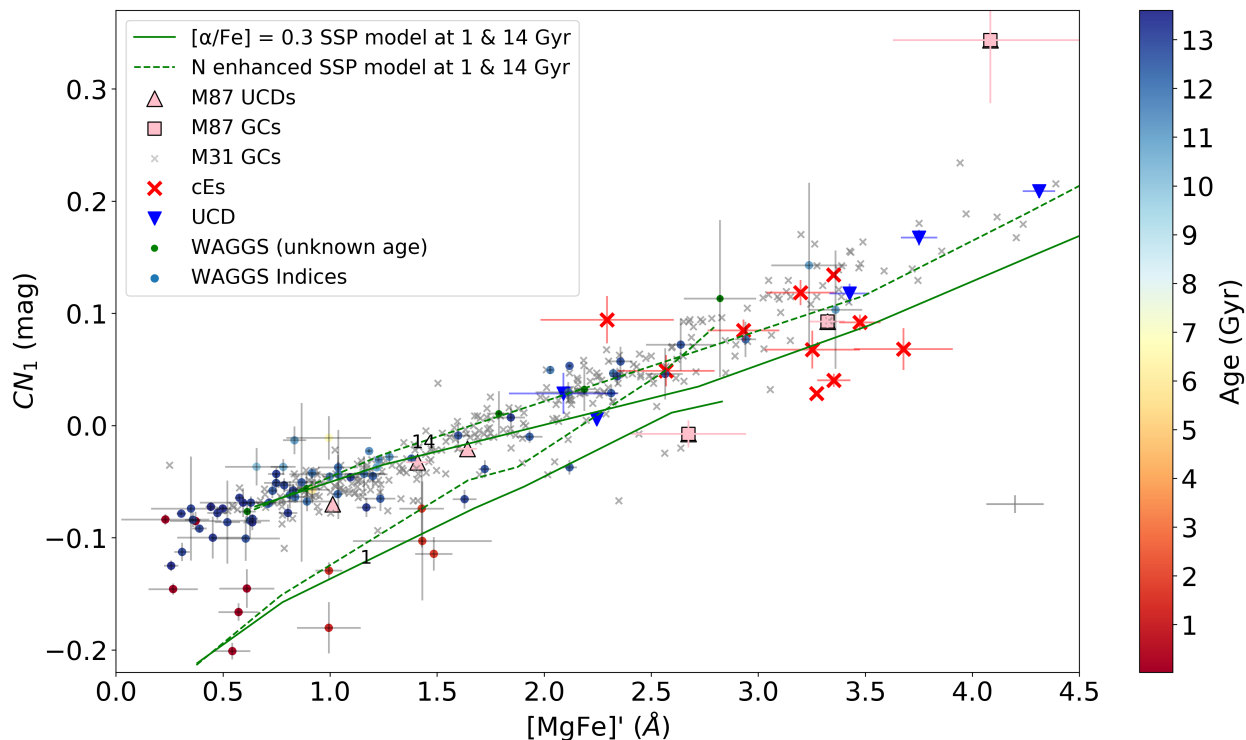


Figure 6.7: Plot of CN_1 against $[MgFe]'$. Also shown are the LIS indices for M87 UCDs and GCs (Forbes et al. 2020) as well as several other UCDs and cEs plotted on top of two plots for N enhanced and alpha enhanced SSP models from Thomas, Maraston and Johansson (2011).

The M87 UCDs are all relatively metal poor and in similar locations to the metal poor galactic globular clusters. Due to the low metallicity it is not possible to identify enhancements in these UCDs, although they do lie below both the N enhanced and alpha enhanced Thomas et al. models, they are within 1σ of the models so assumptions on their abundance enhancements are hard to obtain from these plots. The GCs from M87 are a different story, they appear to be metal rich GCs but only one of them agrees with the galactic and M31 GCs. The more metal poor clusters appear to be severely depleted in CN while the most metal rich GC is severely enhanced in CN relative to the models and galactic GC sequence. However, they both have very large errors and are $\sim 2\sigma$ from being in agreement with the other GCs. The ages and true metallicities of these GCs are unknown which could be a cause of the poor agreement, also due to globular clusters relatively small size and the distance to M87 the S/N of these clusters was quite low (with a mean of $\sim 13.7\text{\AA}^{-1}$ compared to the UCDs $\sim 31\text{\AA}^{-1}$).

The MODS UCDs in Figure 6.7 also show enhancements matching those of the enhanced

globular clusters, indicating that UCDs also possess a population with enhanced N values. This idea is somewhat supported by Taylor et al. (2010) where they also find N enhancement in some UCDs of their sample.

The compact ellipticals are interesting as they appear to be split into two groups. In Figure 6.7 one set is consistently enhanced to the same degree as the GCs while the others seem to not be enhanced and appear to act more like galaxies (in Figure 6.8). This may be expected if there are two types of cE that are present here. One type are intrinsically compact cEs, these formed much like globular clusters but were much bigger and possess a much larger N enhancement than is seen in the other type of cE. The second type of cE formed from the compact bulge of a larger galaxy that has been stripped of its stellar environment. The lower group of cEs support this theory as they match well with the galaxy spectra from Trager et al. (1998b) which consists of central measurements of galaxy nuclei which are metal rich (but have a low S/N and are thus quite scattered). The different cE types seen could potentially be due to poor S/N in the cE data causing scatter and large uncertainty values. However the uncertainties are fairly small and comparable to the galactic GC indices, also there are four cEs which agree very well with the enhanced GC sequence indicating an enhanced stellar population, supporting the theory that there are two different types of cE present in the data.

There is something to be said about the comparison of the binned SDSS galaxy spectra and the galaxy nuclei spectra from Trager et al. (1998b). The binned galaxies in Figure 6.8 are of the inner 12.5 % of light from each galaxy in each bin. Because the galaxies have been binned together it ensures that the S/N in each bin is far greater than in the Trager galaxies leading to a much smaller scatter in the data.

The binned SDSS data also has differential measurements, while one sample concentrates on the inner 12.5% of light the other covers the inner 50% which gives a much broader integrated spectrum containing a larger range of stellar abundances. Figure 6.9 shows that in the central regions; at higher metallicity the galaxies tend towards N enhancement. In the Trager galaxies however, due to the large scatter and uncertainties, it is unclear whether this effect is represented. The SDSS data suggests that there may be a process occurring at higher masses and hence higher central densities which causes nitrogen to be enhanced (such as the effect seen in GCs). The effect would also explain the N enhancement seen in UCDs and some of the cEs, as they both may have sufficient stellar densities for whatever process that causes the N enhancement to occur. The apparent N enhancement of UCDs, some cEs and some galaxy cores presented in this thesis is again discussed in Section 7.1.1.

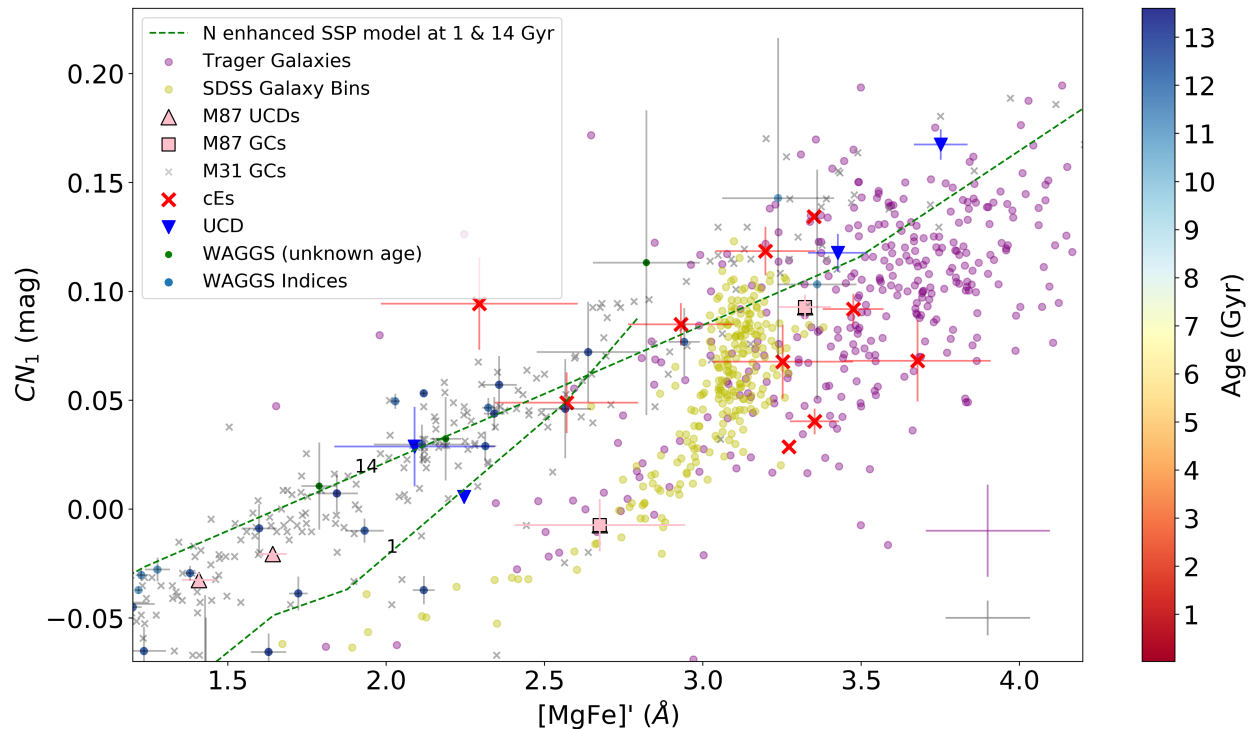


Figure 6.8: This is a similar plot to Figure 6.7 but at a greater detail in the higher metallicities and shows the indices for the inner 12.5% of light from SDSS galaxies binned together and the core light indices of galaxies from Trager et al. (1998b).

6.2.4 Uncertainty Calculations

The uncertainty in $[\text{MgFe}]'$ was completed by simple error propagation. Equation 6.1 is made up of 3 variables Mg_b , $\text{Fe}5270$ and $\text{Fe}5335$ the uncertainties of which were calculated by combining the Monté Carlo simulations with the offset uncertainty via summation in quadrature. Equation 6.1 can be described as $z = \sqrt{y}$ where $z = [\text{MgFe}]'$, $y = \text{Mg}_b \cdot x$ with $x = (0.72 \times \text{Fe}5270) + (0.28 \times \text{Fe}5335)$.

First the uncertainty in x is calculated by:

$$\sigma_x = \sqrt{(0.72 \times \sigma_{\text{Fe}5270})^2 + (0.28 \times \sigma_{\text{Fe}5335})^2} \quad (6.2)$$

The uncertainty in y is then calculated by:

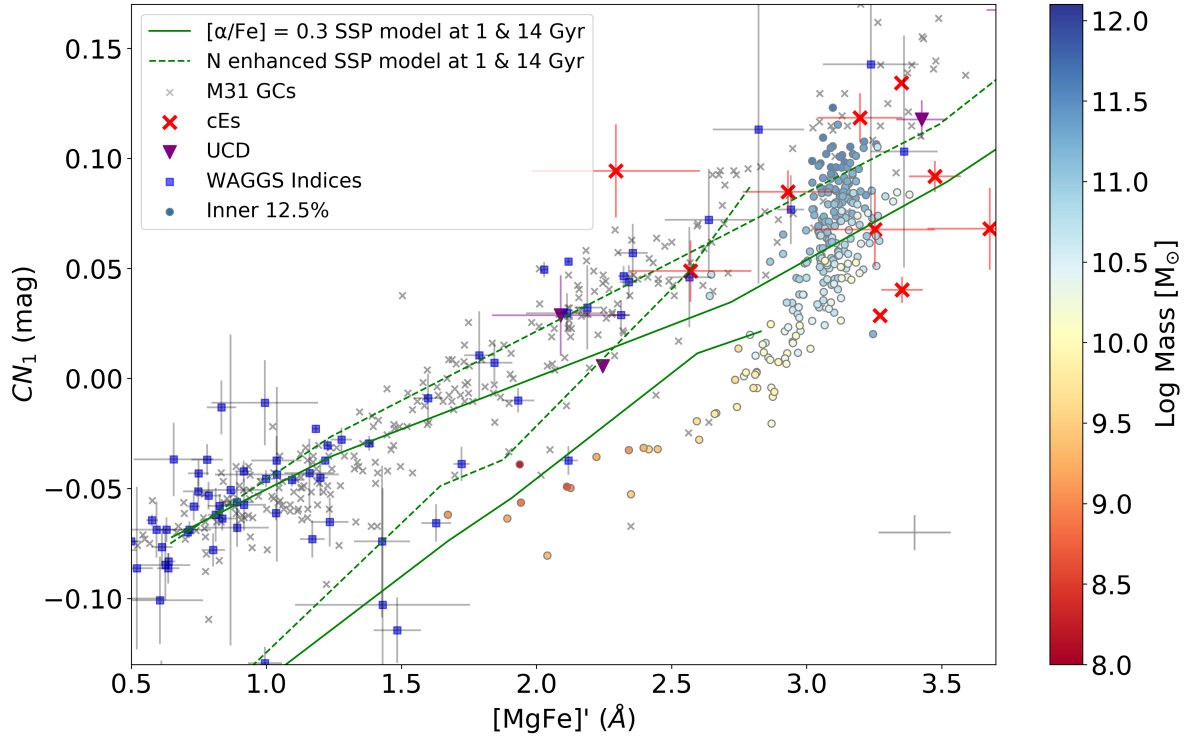
$$\sigma_y = (\text{Mg}_b \cdot x) \times \sqrt{\left(\frac{\sigma_{\text{Mg}_b}}{\text{Mg}_b}\right)^2 + \left(\frac{\sigma_x}{x}\right)^2} \quad (6.3)$$

From this the uncertainty in z (i.e. $[\text{MgFe}]'$) is:

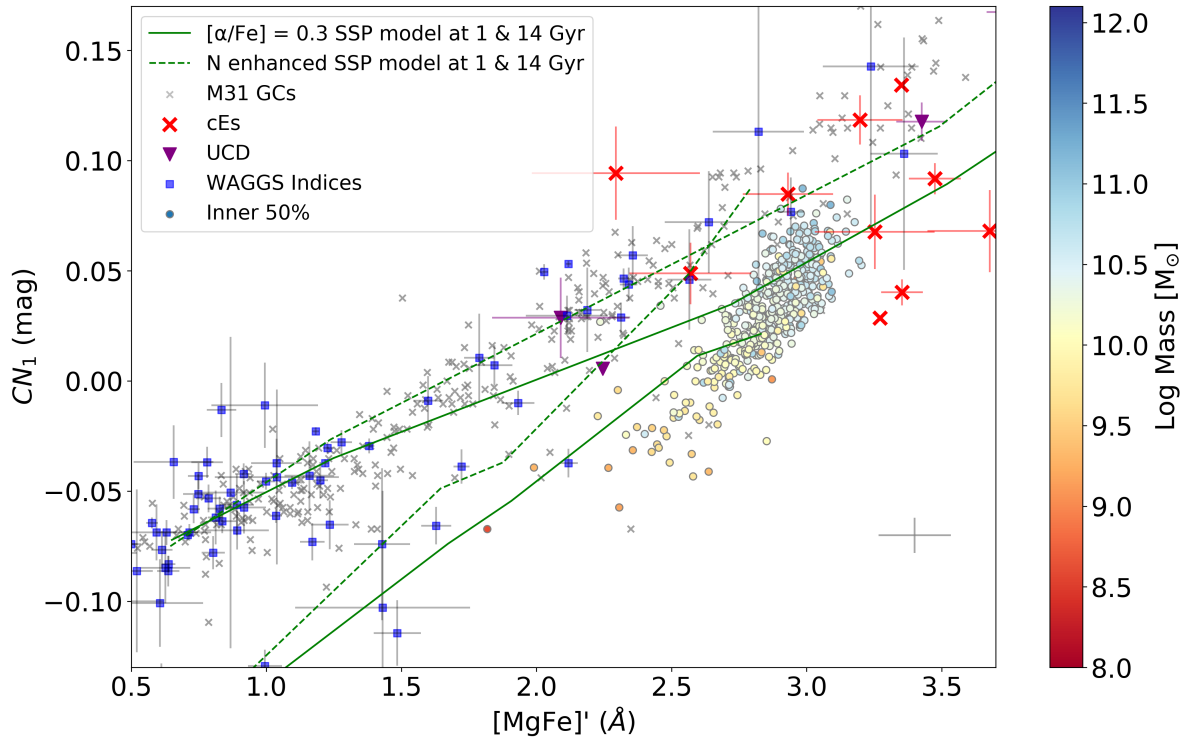
$$\sigma_z = \frac{\sigma_y}{2 \cdot \sqrt{y}} \quad (6.4)$$

All spectra with equivalent 1σ uncertainty-per-pixel values underwent Monté Carlo simulations in the same way as outlined in Section 5.2. Since the additional data did not have offset values for scaling, the uncertainty of the offsets did not need to be taken into account before the $[\text{MgFe}]'$ uncertainty was calculated. The method for calculating $[\text{MgFe}]'$ uncertainty for the additional data was the same as the method shown above.

The Trager galaxies and Schiavon M31 globular clusters all had uncertainties for each index value, the mean of these values was used as an assumed uncertainty value and is shown in the figures as a grey and purple cross for the globular clusters and galaxies respectively.



(a)



(b)

Figure 6.9: Similar to Figure [6.7](#) but with binned SDSS galaxy indices. Plot (a) shows the indices for binned spectra of the inner 12.5 % of light of galaxies, plot (b) shows the indices for the inner 50 % of light. The galaxy mass of each bin is represented in the colour bar.

7|Conclusions and Discussion of Future Work

7.1 Evidence of Multiple Populations

In this thesis I present strong evidence that the nitrogen enhancement present in the secondary populations of globular clusters is observable in the integrated light spectra of the clusters. Measurements of the stellar absorption lines (with comparison to SSP models) and penalised pixel fitting of SSP models to the GC spectra (to find best fit predictions of the GC and to identify chemically enhanced regions) show N enhancement. This thesis shows that these could be effective methods for detecting the chemical enhancements of the secondary populations of globular clusters. Although using line indices N enhancements were also found in other stellar systems which is discussed in Section [7.1.1](#).

A good confirmation that the omitted regions possess signatures of multiple populations is the mass fraction plots. Figure [4.2b](#) shows the mass fraction in age-metallicity space for the fit of NGC 104 where no regions of the spectra have been omitted. There are two clear populations one at around 10 Gyr and another at ~ 4 Gyr. After the regions in Table [8.1](#) are omitted from the fit, in Figure [4.3b](#), the younger ~ 4 Gyr population is no longer in the plot. This implies that whatever spectral features that are causing the younger SSP models to be applied in the best fit (indicating a secondary population), are in the omitted regions. This, combined with the enhancements in the omitted regions (compared to the best fit model) and enhancements of line indices over SSP model indices are a good confirmation indicator that the signatures of multiple populations are in the regions omitted in this thesis and that MPs are detectable in integrated light spectra of globular clusters.

The methods used however are not without their flaws. It is difficult to detect the

presence of N enhancement in the CN indices of globular clusters with a low metallicity ($[\text{MgFe}]' \leq \sim -1.2$). By definition, these globular clusters have fewer metals and therefore would show less of a nitrogen enhancement than GCs at higher metallicities. To overcome this problem the creation of a new line index is proposed. The current N sensitive region, CN_1 (and CN_2) only covers a small area of the region which shows enhancements detected in this thesis via SSP fitting and indicated by the nitrogen enhanced Conroy models (Conroy et al. 2018). A new index which covered the full R_2 region would likely be more sensitive to the enhancement, perhaps making the difference between low metallicity GCs and models such as those used here (i.e. Thomas, Maraston and Johansson 2011) more definable.

Another problem was large scatter in the offsets between the results presented in this thesis and those of Kim et al. (2016). It is believed that the scatter is most likely due to the stochastic stellar distribution in globular clusters combined with the different observation methods used. This is an intrinsic problem with integrated light spectra of local stellar systems as different surveys cover different regions which could drastically change the observed spectra for the same GC.

Using the mass fraction plots could be a good method of MP detection but requires further research into problems (such as the age problem described in Section 7.2). Many of the mass fraction plots show multiple groupings of SSP models which indicates several populations of stars are present, influencing the integrated spectrum. With higher resolution SSP models with more age and metallicity bins (i.e. making a higher resolution mass fraction plot) the smoothing of the weights caused by pPXF regularisation may diminish allowing for more precise prediction of separate populations and their properties via mass-fraction diagrams.

The use of penalised pixel fitting with SSP models to GC spectra has a promising future, but current limitations are holding the method back. Future work on globular clusters with this process would require SSP models with higher spectral resolution (matching that of the data), a range of enhancements and depletions of chemical elements (for the same element range as the Conroy models for example) and the same if not more age and metallicity bins as the MILES models. The amount of chemical enhancement would also preferably be in more detail, for example not just solar abundance and +0.3 dex (as with Thomas models). Having models at a higher resolution would remove the need for having to effectively blur the GC spectra losing information which may more strongly show evidence of multiple populations. The differently enhanced models would be able to show exactly how each GC is enhanced in each element leading, potentially, to more understanding of how globular clusters and

multiple populations are formed in extragalactic GCs. Nitrogen enhancement wasn't just found for globular clusters however.

7.1.1 N enhancement in Dense Stellar Systems

UCDs or Ultra Compact Dwarf galaxies are much larger than globular clusters but smaller than classical descriptions of early type dwarf galaxies. They have luminosity's in the range $-13.5 < M_V < -11$ mag and have sizes roughly $R_{eff} \leq 100$ pc (Faifer et al. 2017) although their mass is often comparable to dwarf galaxies. Due to their high mass and small size they can be described as dense stellar systems. The same can be said for compact elliptical galaxies. cEs are very compact galaxies and have high central stellar densities, their masses are large and they are thought to either be the stripped cores of massive progenitor galaxies or they may have simply formed to be incredibly dense, massive (but relatively small) stellar systems. It may be, in fact, that both of these cases are true and their are sub-types of cE.

The work presented in this thesis shows the N enhancement present in the secondary populations of globular clusters. One occurrence that was not expected however was the finding that some other compact stellar systems (i.e. UCDs, some cEs and maybe galaxy cores) also appear to show nitrogen enhancement, not just globular clusters.

This discovery leads to the suggestion that nitrogen abundance may be dependant on density. All of the UCDs and half of the cEs show N enhancement equivalent to the globular clusters. As UCDs and cEs are considered to be well mixed stellar systems with many stellar populations and a true age spread the N enhancement was not expected to be as extreme (if at all present). As is stated in Section 2.2.1 abundance variations (and the specific elemental correlations mentioned in Section 2.2.1) are only expected in GCs and are one of the defining features of GCs. elemental Correlations are not detected in this thesis for UCDs and cEs but the chemical enhancement present (equivalent to that of the GCs) suggests that this may be the case and more research is needed on this point. The fact that the N enhancement is also present in the central light of the binned SDSS galaxy spectra indicates that some dense galactic cores also show the enhanced nitrogen. Figure 7.1 shows how in the inner 12.5% of light sample, denser galaxies possess N enhancements. Although the trend is not perfect, it does show the densest galaxies appear to be N enhanced and Figure 6.9 shows that the mass of these galaxies indicate a definite correlation with nitrogen abundance. All of the evidence suggests that nitrogen abundance may be directly correlated to increasing stellar density in compact stellar systems.

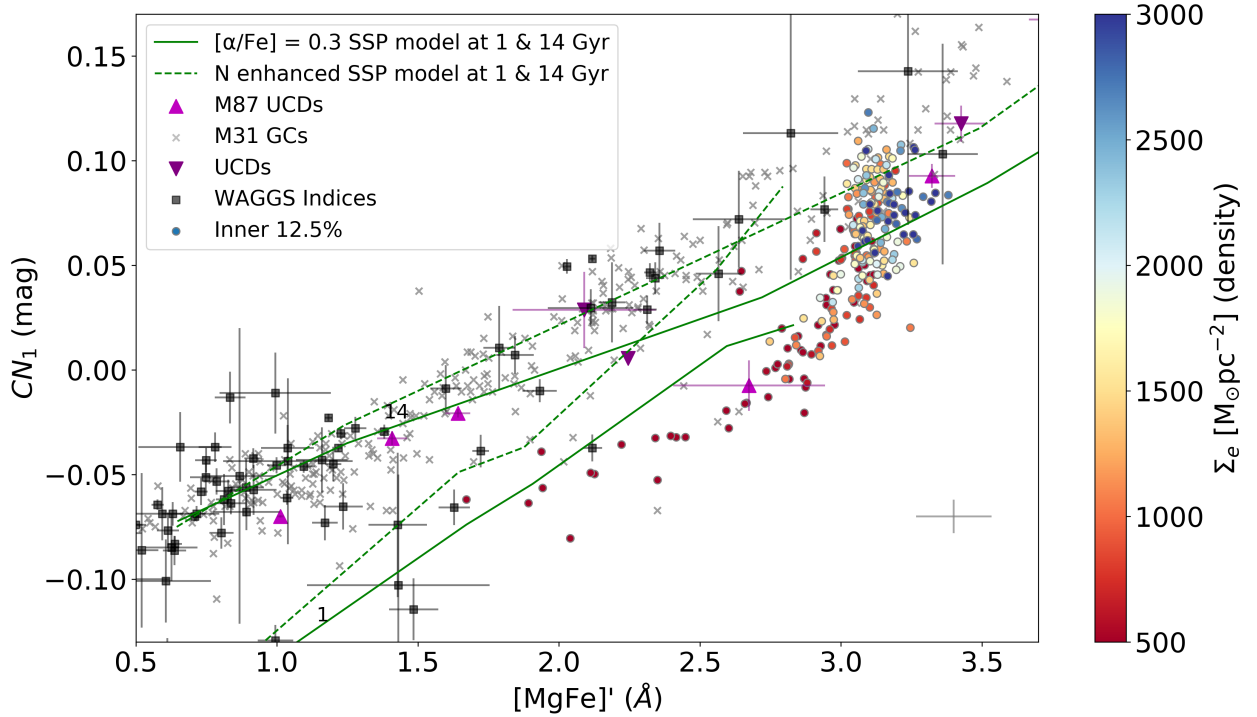


Figure 7.1: Same as Figure 6.9a but using stellar mass surface density (Σ_e) from Norris et al. (2014) in the colour bar for Thomas Davison's SDSS galaxy bins. Density was calculated using the radius and mass values of each bin from the Voronoi diagram: Figure 3.9. The cEs plotted in previous figures are not presented here for clarity of the SDSS data (see Figure 6.9 for more).

7.2 Age Estimation Problem

pPXF often found the ages for the globular clusters to be much younger than literature would suggest. Boecker et al. (2020) find agreements in age between WAGGS and individually resolved stellar spectra that were combined after observation, which indicates that this is a problem specific to integrated light spectra. This effect is possibly due to the penalised pixel fitting method used, as a correlation was found where the lower the literature metallicity, the more inaccurate the mean-age estimation was (compared to literature values). For example:

- NGC 6528 is a relatively very metal rich GC with $[\text{Fe}/\text{H}] = -0.11$ dex and has an age of 11 Gyrs, pPXF suggests a weighted mean age of the SSPs in the fit of 11.36 ± 0.91 Gyr (running pPXF with previously mentioned regions and any emission lines omitted) which is a satisfactory estimation of age. Although in the mass fraction plot

there are large spreads in the age which go as high as 13 Gyr, indicating that at the higher metallicity the age is actually over predicted.

- NGC 6121 has middling metallicity of $[\text{Fe}/\text{H}] = -1.16$ dex with an age of 12.5 Gyr, pPXF calculates its age to be 7.53 ± 0.24 Gyr. The data were fairly well grouped together with one small population at younger ages which were unable to be removed by omitting enhanced regions as has previously been done. This age however is younger than the predicted age.
- NGC 5634 is a metal poor GC, $[\text{Fe}/\text{H}] = -1.88$ and an age of 13 Gyr it is an example of a classic globular cluster, pPXF suggests its age to be 5.26 ± 0.13 Gyr. This is much lower than the expected age and this is the trend for all of the clusters with low metallicity.

The literature values for these globular clusters were obtained from the supplementary files of Usher et al. (2019) listed in Table 8.2. At the time of writing it is unclear what causes this age-discrepancy. While there appears to be an output age dependency on literature metallicity, the output metallicity does not appear to be affected. The Fe/H value output by pPXF was -0.145 ± 0.037 , -1.374 ± 0.031 and -1.758 ± 0.010 for NGC 6528, 6121 and 5634 respectively and there was no pattern detected ($[\text{Fe}/\text{H}]$ being calculated by $[\text{Fe}/\text{H}] = [\text{M}/\text{H}] - (0.94 \cdot [\alpha/\text{Fe}])$ as $[\text{M}/\text{H}]$ was the output of pPXF and $[\alpha/\text{Fe}]$ was the literature value).

It is possible that the literature ages are incorrect which is what Boecker et al. (2020) suggests for NGC 6715. But, due to the presence of the metallicity-age correlation shown in this project, incorrect literature age values are unlikely to be the cause of the poor age estimation.

Firstly, it was thought that this might be due to age-metallicity degeneracy where a single age, single metallicity population can undergo an age change which can be described by a metallicity change where almost all spectral indices remain the same and pPXF was tending towards the younger ages. However the expected relation is that $\delta \log \text{Age} / \delta \log Z \approx \frac{3}{2}$ (Worthey 1999) and the output metallicities do not correlate with the output age. There is often poor Mg fitting however (which Boecker et al. 2020 also find) and this would cause poor true metallicity estimates, so effects due to age-metallicity degeneracy cannot be fully disregarded as the source of this problem.

H line strength is heavily dependant on age and there was often poor fitting of these lines (see Figure 6.3) For NGC 6528 the best fit model underestimated the $H\beta$ and $H\gamma$ lines (but fit well for NGC 5634). This would have been a satisfactory explanation, however poor H fits are not apparent for every GC. More work researching this effect is needed. Boecker et al. (2020) states “it has been shown that SSP equivalent ages and metallicities are biased towards the youngest stellar population present in the integrated light” which may explain the age problem but with the omitted regions excluded from the fit, the signatures of ‘younger’ populations should not be present in the spectra for the fitting process to bias towards, although it may still be due to subtle effects from multiple populations. Also no mention of the relation of output age to cluster metallicity that is found in this thesis has been stated before.

7.3 Conclusion

In conclusion, nitrogen enhancements present in multiple populations can be detected in the integrated light spectra of globular clusters, but only reliably for higher metallicity clusters. The pPXF method shows promise for future work but requires refining and SSP models with more detailed chemical abundances at a higher resolution so as to not lose detail in the globular cluster spectra.

Evidence for a possible connection between stellar density and nitrogen abundance has been found, suggesting that at higher densities nitrogen becomes more enhanced regardless of stellar system. N enhancements have been found in several UCDs, cEs and potentially even the cores of massive dense galaxies. The reason for this may be that the mechanisms which causes N enhancement and create multiple populations in globular clusters only occur at sufficiently high densities but more work is now required in this new area of research. Not all cEs posses enhanced nitrogen, however. But without sufficient data and density values for compact ellipticals it cannot be proven that density is the cause of the presence of enhanced nitrogen in the cEs. cE variation may be due to different formation mechanisms indicating different types of cE.

7.4 Future Research

In terms of further research there are several avenues which can be taken:

Current visible band globular cluster spectra have very poor signal to noise at shorter wavelengths. There are regions at shorter wavelengths which may also show nitrogen abundances which had to be omitted from the fits and measurements of this thesis due to large uncertainties from low signal-to-noise. A dedicated survey of near ultra-violet to visible spectra of galactic globular clusters trying to obtain a large signal-to-noise at the short wavelengths would shine light on these hard to measure regions.

Although only the full WAGGS integrated light spectra is publicly available, the WAGGS team have the full 3D IFU (Integral Field Unit) data cube of all the globular clusters. Potentially, this could be used to identify which stars in the WAGGS field are enhanced secondary population stars and what percentage of the field is enhanced. This data could then be used to develop a new method which predicts the percentage of secondary population stars from the integrated light, allowing the size of secondary populations in extragalactic GCs to be measured.

As stated earlier a new sample of SSP models with higher spectral resolution and a range elemental abundance would potentially help to map out the exact chemical abundances of the multiple populations in the integrated light. Also, when the GC spectra are smoothed to the lower spectral resolution of the SSP models, details are potentially lost which could offer further insight and be stronger indicators of MPs.

In this thesis only nitrogen was used to investigate the signatures of multiple populations. There are other elements which could potentially show this however. Magnesium enhancements are said to be present in many (but not all) multiple populations. Further investigation into the poor fits of Mg that were found in this project may open another avenue of research into the signatures of MPs. The same goes with sodium as this element is also supposed to be enhanced in MPs. If these elements show similar behaviour to the CN region measured in this thesis that could indicate they are suitable signatures of MPs in integrated light spectra.

Another piece of further work is to obtain additional high S/N spectra of extragalactic GCs from a range of galaxies that covers the correct wavelength range. These could be used to probe evidence of multiple populations to see if the properties of galactic GCs' multiple

populations are universal. The method in this thesis was used specifically so as to define a way of measuring extragalactic GCs to detect multiple populations, so that is the logical next step.

Finally, a suggestion for further work would be to examine the galaxy spectra in greater detail, perhaps using dedicated spectroscopy of a sample of galaxies of different masses to search for signs that the N abundance varies with radius. The work in this thesis suggests that at higher masses, and potentially densities, the cores of galaxies are N enhanced. If this is the case, this would be a key discovery for galactic evolution theories.

Bibliography

- Abadi, Mario G., Julio F. Navarro and Matthias Steinmetz. 2006. *MNRAS* 365 (3): 747–758. doi:[10.1111/j.1365-2966.2005.09789.x](https://doi.org/10.1111/j.1365-2966.2005.09789.x).
- Anguiano, B., et al. 2015. *MNRAS* 451 (2): 1229–1246. doi:[10.1093/mnras/stv800](https://doi.org/10.1093/mnras/stv800).
- Arnould, M., S. Goriely and A. Jorissen. 1999. *A&A* 347:572–582. arXiv: [astro-ph/9904407](https://arxiv.org/abs/astro-ph/9904407) [[astro-ph](https://arxiv.org/abs/astro-ph)].
- Bastian, Nate, and Carmela Lardo. 2018. *ARA&A* 56 (1): 83–136. doi:[10.1146/annurev-astro-081817-051839](https://doi.org/10.1146/annurev-astro-081817-051839).
- Battaglia, G., et al. 2006. *A&A* 459 (2): 423–440. doi:[10.1051/0004-6361:20065720](https://doi.org/10.1051/0004-6361:20065720).
- Bekki, Kenji. 2017. *MNRAS* 467 (2): 1857–1873. doi:[10.1093/mnras/stx110](https://doi.org/10.1093/mnras/stx110).
- Bekki, Kenji, et al. 2004. *ApJ* 610 (2): L93–L96. doi:[10.1086/423372](https://doi.org/10.1086/423372).
- Bell, R. A., and R. J. Dickens. 1980. *ApJ* 242:657–672. doi:[10.1086/158502](https://doi.org/10.1086/158502).
- Bellazzini, M., et al. 2003. *A&A* 405 (2): 577–583. doi:[10.1051/0004-6361:20030649](https://doi.org/10.1051/0004-6361:20030649).
- Boecker, Alina, et al. 2020. *ApJ* 896 (1): 13. doi:[10.3847/1538-4357/ab919d](https://doi.org/10.3847/1538-4357/ab919d).
- Breen, Philip G. 2018. *MNRASL* 481 (1): L110–L114. doi:[10.1093/mnrasl/sly169](https://doi.org/10.1093/mnrasl/sly169).
- Brodie, Jean P., and Jay Strader. 2006. *ARA&A* 44 (1): 193–267. doi:[10.1146/annurev.astro.44.051905.092441](https://doi.org/10.1146/annurev.astro.44.051905.092441).
- Brodie, Jean P., et al. 2014. *ApJ* 796 (1): 52. doi:[10.1088/0004-637X/796/1/52](https://doi.org/10.1088/0004-637X/796/1/52).
- Brown, Jeffery A., and George Wallerstein. 1992. *AJ* 104:1818. doi:[10.1086/116360](https://doi.org/10.1086/116360).
- Burkert, Andreas, and Graeme H. Smith. 1997. *ApJ* 474 (1): L15–L18. doi:[10.1086/310421](https://doi.org/10.1086/310421).
- Caldwell, Nelson, and Aaron J. Romanowsky. 2016a. *ApJ* 824 (1): 42. doi:[10.3847/0004-637X/824/1/42](https://doi.org/10.3847/0004-637X/824/1/42).
- . 2016b. *ApJ* 824 (1): 42. doi:[10.3847/0004-637X/824/1/42](https://doi.org/10.3847/0004-637X/824/1/42).
- Cappellari, Michele. 2017. *MNRAS* 466 (1): 798–811. doi:[10.1093/mnras/stw3020](https://doi.org/10.1093/mnras/stw3020).
- Cappellari, Michele, and Eric Emsellem. 2004. *PASP* 116 (816): 138–147. doi:[10.1086/381875](https://doi.org/10.1086/381875).
- Carballo-Bello, Julio A., et al. 2020. *MNRAS*. doi:[10.1093/mnras/staa2655](https://doi.org/10.1093/mnras/staa2655).
- Carrera, R., et al. 2008. *AJ* 135 (3): 836–849. doi:[10.1088/0004-6256/135/3/836](https://doi.org/10.1088/0004-6256/135/3/836).
- Carretta, E., et al. 2010a. *A&A* 516:A55. doi:[10.1051/0004-6361/200913451](https://doi.org/10.1051/0004-6361/200913451).
- Carretta, E., et al. 2010b. *A&A* 520:A95. doi:[10.1051/0004-6361/201014924](https://doi.org/10.1051/0004-6361/201014924).
- Cenarro, A. J., et al. 2007. *MNRAS* 374 (2): 664–690. doi:[10.1111/j.1365-2966.2006.11196.x](https://doi.org/10.1111/j.1365-2966.2006.11196.x).
- Cezario, E., et al. 2012. *A&A* 549:A60. doi:[10.1051/0004-6361/201220336](https://doi.org/10.1051/0004-6361/201220336).
- Chantereau, W, et al. 2019. *MNRAS* 484 (4): 5236–5244. doi:[10.1093/mnras/stz378](https://doi.org/10.1093/mnras/stz378).
- Childress, Michael J, et al. 2014. *Astrophys. Space Sci.* 349 (2): 617–636. doi:[10.1007/s10509-013-1682-0](https://doi.org/10.1007/s10509-013-1682-0).

- Cohen, Judith G. 2004. *AJ* 127 (3): 1545–1554. doi:[10.1086/382104](https://doi.org/10.1086/382104).
- Colucci, Janet E., Rebecca A. Bernstein and Andrew McWilliam. 2017. *ApJ* 834 (2): 105. doi:[10.3847/1538-4357/834/2/105](https://doi.org/10.3847/1538-4357/834/2/105).
- Colucci, Janet E., et al. 2012. *ApJ* 746 (1): 29. doi:[10.1088/0004-637X/746/1/29](https://doi.org/10.1088/0004-637X/746/1/29).
- Conroy, Charlie, and David N. Spergel. 2011. *ApJ* 726 (1): 36. doi:[10.1088/0004-637X/726/1/36](https://doi.org/10.1088/0004-637X/726/1/36).
- Conroy, Charlie, et al. 2018. *ApJ* 854 (2): 139. doi:[10.3847/1538-4357/aaab49](https://doi.org/10.3847/1538-4357/aaab49).
- D’Ercole, A., F. D’Antona and E. Vesperini. 2016. *MNRAS* 461 (4): 4088–4098. doi:[10.1093/mnras/stw1583](https://doi.org/10.1093/mnras/stw1583).
- D’Ercole, Annibale, et al. 2008. *MNRAS* 391 (2): 825–843. doi:[10.1111/j.1365-2966.2008.13915.x](https://doi.org/10.1111/j.1365-2966.2008.13915.x).
- de Boer, T. J. L., and M. Fraser. 2016. *A&A* 590:A35. doi:[10.1051/0004-6361/201527580](https://doi.org/10.1051/0004-6361/201527580).
- de Mink, S. E., et al. 2009. *A&A* 507 (1): L1–L4. doi:[10.1051/0004-6361/200913205](https://doi.org/10.1051/0004-6361/200913205).
- Dias, B., et al. 2016. *A&A* 590 (1): A9. doi:[10.1051/0004-6361/201526765](https://doi.org/10.1051/0004-6361/201526765).
- Dopita, M. A., and G. H. Smith. 1986. *ApJ* 304:283. doi:[10.1086/164162](https://doi.org/10.1086/164162).
- Dopita, Michael, et al. 2007. *Astrophys. Space Sci.* 310 (3): 255–268. doi:[10.1007/s10509-007-9510-z](https://doi.org/10.1007/s10509-007-9510-z).
- Dotter, Aaron, Ata Sarajedini and Jay Anderson. 2011. *ApJ* 738 (1): 74. doi:[10.1088/0004-637X/738/1/74](https://doi.org/10.1088/0004-637X/738/1/74).
- Evans, N. W., and M. I. Wilkinson. 2000. *MNRAS* 316 (4): 929–942. doi:[10.1046/j.1365-8711.2000.03645.x](https://doi.org/10.1046/j.1365-8711.2000.03645.x).
- Faifer, Favio R., et al. 2017. *A&A* 599:L8. doi:[10.1051/0004-6361/201730493](https://doi.org/10.1051/0004-6361/201730493).
- Fernández-Trincado, José G., et al. 2019. *A&A* 631:A97. doi:[10.1051/0004-6361/201935369](https://doi.org/10.1051/0004-6361/201935369).
- Font, Andreea S., et al. 2006. *ApJ* 646 (2): 886–898. doi:[10.1086/505131](https://doi.org/10.1086/505131).
- Forbes, Duncan A., and Terry. Bridges. 2010. *MNRAS* 404 (3): 1203–1214. doi:[10.1111/j.1365-2966.2010.16373.x](https://doi.org/10.1111/j.1365-2966.2010.16373.x).
- Forbes, Duncan A., et al. 2018. *Proc. R. Soc. A.* 474 (2210). doi:[10.1098/rspa.2017.0616](https://doi.org/10.1098/rspa.2017.0616).
- Forbes, Duncan A., et al. 2020. *MNRAS* 497 (1): 765–775. doi:[10.1093/mnras/staa1924](https://doi.org/10.1093/mnras/staa1924).
- Fryer, Chris L. 1999. *ApJ* 522 (1): 413–418. doi:[10.1086/307647](https://doi.org/10.1086/307647).
- Fryer, Chris L., and Vassiliki Kalogera. 2001. *ApJ* 554 (1): 548–560. doi:[10.1086/321359](https://doi.org/10.1086/321359).
- Garro, E. R., et al. 2020. *A&A* 642:L19. doi:[10.1051/0004-6361/202039233](https://doi.org/10.1051/0004-6361/202039233).
- Gieles, Mark, et al. 2018. *MNRAS* 478 (2): 2461–2479. doi:[10.1093/mnras/sty1059](https://doi.org/10.1093/mnras/sty1059).
- Glatt, Katharina, et al. 2008. *AJ* 136 (4): 1703–1727. doi:[10.1088/0004-6256/136/4/1703](https://doi.org/10.1088/0004-6256/136/4/1703).
- González, J. J. 1993. “Line strength gradients and kinematic profiles in elliptical galaxies”. PhD thesis, UNIVERSITY OF CALIFORNIA.
- Gorgas, Javier, et al. 1993. *ApJS* 86:153. doi:[10.1086/191774](https://doi.org/10.1086/191774).
- Goudfrooij, Paul, et al. 2014. *ApJ* 797 (1): 35. doi:[10.1088/0004-637X/797/1/35](https://doi.org/10.1088/0004-637X/797/1/35).
- Graczyk, Dariusz, et al. 2013. *ApJ* 780 (1): 59. doi:[10.1088/0004-637x/780/1/59](https://doi.org/10.1088/0004-637x/780/1/59).
- Gratton, R. G. et al. 2011. *A&A* 534:A72. doi:[10.1051/0004-6361/201117093](https://doi.org/10.1051/0004-6361/201117093).
- Gratton, Raffaele G., Eugenio Carretta and Angela Bragaglia. 2012. *A&AR* 20:50. doi:[10.1007/s00159-012-0050-3](https://doi.org/10.1007/s00159-012-0050-3).
- Gratton, Raffaele, Christopher Sneden and Eugenio Carretta. 2004. *ARA&A* 42 (1): 385–440. doi:[10.1146/annurev.astro.42.053102.133945](https://doi.org/10.1146/annurev.astro.42.053102.133945).
- Gruyters, Pieter, et al. 2017. *A&A* 603:A37. doi:[10.1051/0004-6361/201630341](https://doi.org/10.1051/0004-6361/201630341).
- Harris, William E. 1996. *AJ* 112:1487. doi:[10.1086/118116](https://doi.org/10.1086/118116).

- Herschel, William. 1789. *Philosophical Transactions of the Royal Society of London* 79:212–255. doi:[10.1098/rstl.1789.0021](https://doi.org/10.1098/rstl.1789.0021).
- Höfner, Susanne, and Hans Olofsson. 2018. *A&AR* 26 (1): 1–92. doi:[10.1007/s00159-017-0106-5](https://doi.org/10.1007/s00159-017-0106-5).
- Hu, Tao, and Qiuhe Peng. 2008. *ApJ* 681 (1): 96–103. doi:[10.1086/588085](https://doi.org/10.1086/588085).
- Jansen, Rolf, and Sheila Kannappan. 2001. *Astrophys. Space Sci.* 276:1151–1159. doi:[10.1023/A:1011954916413](https://doi.org/10.1023/A:1011954916413).
- Johnson, Christian I., and Catherine A. Pilachowski. 2010. *ApJ* 722 (2): 1373–1410. doi:[10.1088/0004-637X/722/2/1373](https://doi.org/10.1088/0004-637X/722/2/1373).
- Kaaret, Philip, Hua Feng and Timothy P. Roberts. 2017. *ARA&A* 55 (1): 303–341. doi:[10.1146/annurev-astro-091916-055259](https://doi.org/10.1146/annurev-astro-091916-055259).
- Karczmarek, Paulina, et al. 2017. *AJ* 154 (6): 263. doi:[10.3847/1538-3881/aa9574](https://doi.org/10.3847/1538-3881/aa9574).
- Kawakatu, Nozomu, and Masayuki Umemura. 2005. *ApJ* 628 (2): 721–728. doi:[10.1086/430772](https://doi.org/10.1086/430772).
- Kim, Hak-Sub, et al. 2016. *ApJS* 227 (2): 24. doi:[10.3847/1538-4365/227/2/24](https://doi.org/10.3847/1538-4365/227/2/24).
- King, A. R., and K. A. Pounds. 2003. *MNRAS* 345 (2): 657–659. doi:[10.1046/j.1365-8711.2003.06980.x](https://doi.org/10.1046/j.1365-8711.2003.06980.x).
- King, I. R., et al. 2012. *AJ* 144 (1): 5. doi:[10.1088/0004-6256/144/1/5](https://doi.org/10.1088/0004-6256/144/1/5).
- Kirch, Gottfried. 1681. “Ephemeridum Motuum Coelestium ad Annum Æræ Christianæ MDCLXXXI”: 47–48.
- Kremer, Kyle, et al. 2018. *ApJ* 855 (2): L15. doi:[10.3847/2041-8213/aab26c](https://doi.org/10.3847/2041-8213/aab26c).
- Kronberg, Christine, and Hartmut Frommert. 2019. *Milky Way Globular Clusters*. First published in June 2011. last modified on 06/01/2019. Visited on 04/08/2020. https://www.messier.seds.org/xtra/supp/mw_gc.html.
- Kroupa, Pavel. 2001. *MNRAS* 322 (2): 231–246. doi:[10.1046/j.1365-8711.2001.04022.x](https://doi.org/10.1046/j.1365-8711.2001.04022.x).
- Kruijssen, J. M. Diederik, et al. 2020. *MNRAS* 498 (2): 2472–2491. doi:[10.1093/mnras/staa2452](https://doi.org/10.1093/mnras/staa2452).
- Larsen, S. S., J. P. Brodie and J. Strader. 2012. *A&A* 546:A53. doi:[10.1051/0004-6361/201219895](https://doi.org/10.1051/0004-6361/201219895).
- . 2017. *A&A* 601:A96. doi:[10.1051/0004-6361/201630130](https://doi.org/10.1051/0004-6361/201630130).
- Loup, C., et al. 1993. *A&AS* 99:291–377.
- Lynden-Bell, D., and R. M. Lynden-Bell. 1995. *MNRAS* 275 (2): 429–442. doi:[10.1093/mnras/275.2.429](https://doi.org/10.1093/mnras/275.2.429).
- Mackey, A. D. 2009. “The Star Clusters of the Magellanic Clouds”. In *The Ages of Stars*, ed. by Eric E. Mamajek, David R. Soderblom and Rosemary F. G. Wyse, 258:275–286. IAU Symposium. doi:[10.1017/S1743921309031925](https://doi.org/10.1017/S1743921309031925).
- Mackey, A. D., and G. F. Gilmore. 2003. *MNRAS* 338 (1): 85–119. doi:[10.1046/j.1365-8711.2003.06021](https://doi.org/10.1046/j.1365-8711.2003.06021).
- Majewski, Steven R., et al. 2003. *ApJ* 599 (2): 1082–1115. doi:[10.1086/379504](https://doi.org/10.1086/379504).
- Martell, Sarah L., Graeme H. Smith and Michael M. Briley. 2008. *PASP* 120 (863): 7–15. doi:[10.1086/525060](https://doi.org/10.1086/525060).
- Martell, Sarah. L., et al. 2011. *A&A* 534:A136. doi:[10.1051/0004-6361/201117644](https://doi.org/10.1051/0004-6361/201117644).
- Martocchia, S, et al. 2020. *MNRAS* 495 (4): 4518–4528. doi:[10.1093/mnras/staa1482](https://doi.org/10.1093/mnras/staa1482).
- McGregor, Peter J., et al. 1999. *PASA* 16 (3): 273–287. doi:[10.1071/AS99273](https://doi.org/10.1071/AS99273).
- McLaughlin, Dean E., and Roeland P. van der Marel. 2005. *ApJS* 161 (2): 304–360. doi:[10.1086/497429](https://doi.org/10.1086/497429).
- Messier, Charles. 1771. “Catalog of Nebulas and Star Clusters, that One Discovers Among the Fixed Stars on the Horizon of Paris; Observed at the Naval Observatory, with Various Instruments”. Translated version available at: <https://www.messier.seds.org/xtra/history/m-cat71.html>, *Memoirs of the French Academy of Sciences for 1771*: 435–461.
- Mészáros, Szabolcs, et al. 2015. *AJ* 149 (5): 153. doi:[10.1088/0004-6256/149/5/153](https://doi.org/10.1088/0004-6256/149/5/153).

- Milone, A P, et al. 2019. *MNRAS* 491 (1): 515–531. doi:[10.1093/mnras/stz2999](https://doi.org/10.1093/mnras/stz2999).
- Milone, A. P. 2014. *MNRAS* 446 (2): 1672–1684. doi:[10.1093/mnras/stu2198](https://doi.org/10.1093/mnras/stu2198).
- Milone, A. P., et al. 2014. *TApJ* 785 (1): 21. doi:[10.1088/0004-637X/785/1/21](https://doi.org/10.1088/0004-637X/785/1/21).
- Milone, A. P., et al. 2017. *MNRAS* 464 (3): 3636–3656. doi:[10.1093/mnras/stw2531](https://doi.org/10.1093/mnras/stw2531).
- Milone, A. P., et al. 2018a. *MNRAS* 477 (2): 2640–2663. doi:[10.1093/mnras/sty661](https://doi.org/10.1093/mnras/sty661).
- Milone, A. P., et al. 2018b. *MNRAS* 481 (4): 5098–5122. doi:[10.1093/mnras/sty2573](https://doi.org/10.1093/mnras/sty2573).
- Monelli, M., et al. 2013. *MNRAS* 431 (3): 2126–2149. doi:[10.1093/mnras/stt273](https://doi.org/10.1093/mnras/stt273).
- Mukhopadhyay, Banibrata, and Sandip K. Chakrabarti. 2000. *A&A* 353:1029–1043. arXiv: [astro-ph/9912568](https://arxiv.org/abs/astro-ph/9912568).
- Murga, Maria, et al. 2015. *MNRAS* 452 (1): 511–519. doi:[10.1093/mnras/stv1277](https://doi.org/10.1093/mnras/stv1277).
- Newberg, Heidi Jo, et al. 2002. *ApJ* 569 (1): 245–274. doi:[10.1086/338983](https://doi.org/10.1086/338983).
- Niederhofer, F., et al. 2015. *A&A* 575:A62. doi:[10.1051/0004-6361/201424455](https://doi.org/10.1051/0004-6361/201424455).
- Norris, Mark A., et al. 2014. *MMNRAS* 443 (2): 1151–1172. doi:[10.1093/mnras/stu1186](https://doi.org/10.1093/mnras/stu1186).
- Olsen, K. A. G., et al. 1998. *MNRAS* 300 (3): 665–685. doi:[10.1046/j.1365-8711.1998.01860.x](https://doi.org/10.1046/j.1365-8711.1998.01860.x).
- Osborn, W. 1971. *Obs* 91:223–224.
- Pagel, B. E. J., and G. Tautvaišienė. 1998. *MNRAS* 299 (2): 535–544. doi:[10.1046/j.1365-8711.1998.01792.x](https://doi.org/10.1046/j.1365-8711.1998.01792.x).
- Peebles, P. J. E., and R. H. Dicke. 1968. *ApJ* 154:891. doi:[10.1086/149811](https://doi.org/10.1086/149811).
- Pietrinferni, Adriano, et al. 2004. *ApJ* 612 (1): 168–190. doi:[10.1086/422498](https://doi.org/10.1086/422498).
- Pietrzyński, G., et al. 2019. *Nature* 567 (7747): 200–203. doi:[10.1038/s41586-019-0999-4](https://doi.org/10.1038/s41586-019-0999-4).
- Pillastrini, Giovanni C. Baiesi. 2009. *MNRAS* 397 (4): 1990–1994. doi:[10.1111/j.1365-2966.2009.15109.x](https://doi.org/10.1111/j.1365-2966.2009.15109.x).
- Puzia, T. H., et al. 2002. *A&A* 395 (1): 45–67. doi:[10.1051/0004-6361:20021283](https://doi.org/10.1051/0004-6361:20021283).
- Reid, M. J., et al. 2009. doi:[10.1088/0004-637x/700/1/137](https://doi.org/10.1088/0004-637x/700/1/137).
- Rich, R. M. 2003. “The M31 Globular Cluster System”. In *New Horizons in Globular Cluster Astronomy*, ed. by Giampaolo Piotto et al., 296:533. Astronomical Society of the Pacific Conference Series.
- Rodgers, A. W., P. Conroy and G. Bloxham. 1988. *PASP* 100:626. doi:[10.1086/132212](https://doi.org/10.1086/132212).
- Rolfs, Claus E., and William S. Rodney. 1988. *Cauldrons in the Cosmos*. Nuclear Astrophysics. Chicago: University of Chicago Press. ISBN: 9780226724577.
- Růžička, Adam, Christian Theis and Jan Palouš. 2009. *ApJ* 691 (2): 1807–1815. doi:[10.1088/0004-637x/691/2/1807](https://doi.org/10.1088/0004-637x/691/2/1807).
- Salinas, Ricardo, and Jay Strader. 2015. *ApJ* 809 (2): 169. doi:[10.1088/0004-637X/809/2/169](https://doi.org/10.1088/0004-637X/809/2/169).
- Sánchez-Blázquez, P., et al. 2006. *MNRAS* 371 (2): 703–718. doi:[10.1111/j.1365-2966.2006.10699.x](https://doi.org/10.1111/j.1365-2966.2006.10699.x).
- Sarajedini, Ata, et al. 2007. *AJ* 133 (4): 1658–1672. doi:[10.1086/511979](https://doi.org/10.1086/511979).
- Schiavon, Ricardo P., et al. 2005. *ApJS* 160 (1): 163–175. doi:[10.1086/431148](https://doi.org/10.1086/431148).
- Schiavon, Ricardo P., et al. 2012. *AJ* 143 (1): 14. doi:[10.1088/0004-6256/143/1/14](https://doi.org/10.1088/0004-6256/143/1/14).
- Shapley, H. 1918. *PASP* 30:42. doi:[10.1086/122686](https://doi.org/10.1086/122686).
- . 1938. *Nature* 135:715–716. doi:[10.1038/142715b0](https://doi.org/10.1038/142715b0).
- Sirianni, Marco, et al. 2002. *ApJ* 579 (1): 275–288. doi:[10.1086/342723](https://doi.org/10.1086/342723).
- Smecker-Hane, Tammy A., et al. 2002. *ApJ* 566 (1): 239–244. doi:[10.1086/337985](https://doi.org/10.1086/337985).

- Smith, Graeme H., and John E. Norris. 1993. *AJ* 105:173. doi:[10.1086/116418](https://doi.org/10.1086/116418).
- Smolinski, Jason P., et al. 2011. *AJ* 142 (4): 126. doi:[10.1088/0004-6256/142/4/126](https://doi.org/10.1088/0004-6256/142/4/126).
- Snedden, Christopher, et al. 1992. *AJ* 104:2121–2140. doi:[10.1086/116388](https://doi.org/10.1086/116388).
- Sosin, Craig, et al. 1997. *ApJL* 480 (1): L35–L38. doi:[10.1086/310606](https://doi.org/10.1086/310606).
- Surdin, V. G. 1994. *Astron. Lett.* 20 (3): 398–402.
- Tautvaišienė, Gražina, et al. 2004. *AJ* 127 (1): 373–379. doi:[10.1086/379561](https://doi.org/10.1086/379561).
- Taylor, Matthew A., et al. 2010. *ApJ* 712 (2): 1191–1208. doi:[10.1088/0004-637X/712/2/1191](https://doi.org/10.1088/0004-637X/712/2/1191).
- Tenorio-Tagle, Guillermo, et al. 2015. *ApJL* 814 (1): L8. doi:[10.1088/2041-8205/814/1/L8](https://doi.org/10.1088/2041-8205/814/1/L8).
- Thomas, Daniel, Claudia Maraston and Ralf Bender. 2003. *MNRAS* 339 (3): 897–911. doi:[10.1046/j.1365-8711.2003.06248.x](https://doi.org/10.1046/j.1365-8711.2003.06248.x).
- Thomas, Daniel, Claudia Maraston and Jonas Johansson. 2011. *MNRAS* 412 (4): 2183–2198. doi:[10.1111/j.1365-2966.2010.18049.x](https://doi.org/10.1111/j.1365-2966.2010.18049.x).
- Trager, S. C., et al. 1998a. *VizieR Online Data Catalog*: J/ApJS/116/1.
- Trager, S. C., et al. 1998b. *ApJS* 116 (1): 1–28. doi:[10.1086/313099](https://doi.org/10.1086/313099).
- Usher, Christopher. 2017. *WAGGS Data*. <https://www.astro.ljmu.ac.uk/~astcushe/waggs/data.html>.
- Usher, Christopher, et al. 2017. *MNRAS* 468 (4): 3828–3849. doi:[10.1093/mnras/stx713](https://doi.org/10.1093/mnras/stx713).
- Usher, Christopher, et al. 2019. *MNRAS* 482 (1): 1275–1303. doi:[10.1093/mnras/sty2611](https://doi.org/10.1093/mnras/sty2611).
- Vazdekis, A., et al. 2010. *MNRAS* 404 (4): 1639–1671. doi:[10.1111/j.1365-2966.2010.16407.x](https://doi.org/10.1111/j.1365-2966.2010.16407.x).
- Vazdekis, A., et al. 2016. *MNRAS* 463 (4): 3409–3436. doi:[10.1093/mnras/stw2231](https://doi.org/10.1093/mnras/stw2231).
- Villanova, S., et al. 2007. *ApJ* 663 (1): 296–314. doi:[10.1086/517905](https://doi.org/10.1086/517905).
- Wang, M. Y., et al. 2019. *ApJ* 875 (2): L13. doi:[10.3847/2041-8213/ab14f5](https://doi.org/10.3847/2041-8213/ab14f5).
- Wei, Dandan, et al. 2020. *MNRAS* 493 (4): 5479–5488. doi:[10.1093/mnras/staa613](https://doi.org/10.1093/mnras/staa613).
- Wise, John H., et al. 2012. *ApJ* 745 (1): 50. doi:[10.1088/0004-637X/745/1/50](https://doi.org/10.1088/0004-637X/745/1/50).
- Worthey, G. 1999. “The Age-Metallicity Degeneracy”. In *Spectrophotometric Dating of Stars and Galaxies*, ed. by Ivan Hubeny, Sally Heap and Robert Cornett, 192:283. Astronomical Society of the Pacific Conference Series.
- Worthey, Guy, and D. L. Ottaviani. 1997. *ApJS* 111 (2): 377–386. doi:[10.1086/313021](https://doi.org/10.1086/313021).
- Worthey, Guy, et al. 1994. *ApJS* 94:687. doi:[10.1086/192087](https://doi.org/10.1086/192087).
- Yong, D., et al. 2005. *A&A* 438 (3): 875–888. doi:[10.1051/0004-6361:20052916](https://doi.org/10.1051/0004-6361:20052916).
- Yong, David, et al. 2008. *ApJ* 684 (2): 1159–1169. doi:[10.1086/590658](https://doi.org/10.1086/590658).
- Zepf, Stephen E., and Keith M. Ashman. 1993. *MNRAS* 264 (3): 611–618. doi:[10.1093/mnras/264.3.611](https://doi.org/10.1093/mnras/264.3.611).
- Zijlstra, Albert A. 2004. *MNRAS* 348 (2): L23–L27. doi:[10.1111/j.1365-2966.2004.07552.x](https://doi.org/10.1111/j.1365-2966.2004.07552.x).

8 | APPENDIX

Table 8.1: Table of Omitted Regions.

ID	Range (Å)	N.Pix
R ₁	3800 - 4016	696
R ₂	4117 - 4218	292
R ₃	5825 - 6800	357

Notes. N.Pix is the number of pixels in the omitted range: ‘Range (Å)’ corresponding to the region ID: ‘R₁₋₃’.

Table 8.2: Table of the globular clusters used in this project.

Name	Galaxy	[Fe/H] dex	Age Gyr	Rad_h arcsec	A_V Mag	M(GC) M _⊙	M (field) M _⊙	[α/Fe]	MPs Y/N
Fornax 3	Fornax	-2.33	12	6.41	0.11	5.42	5.29	0.26 ^c ± 0.03	? ^a
Fornax 4	Fornax	-1.42	10	4.68	0.43	5.23	5.13		
Fornax 5	Fornax	-2.09	13	6.99	0.1	5.11	4.94		
NGC 0104	MW	-0.72	12.75	190.2	0.12	6	4.68		
NGC 0121	SMC	-1.28	10.5	19.02	0.45	5.61	5.2		
NGC 0330	SMC	-0.81	0.03	21	0.2	4.57	4.14	N ^b	
NGC 0361	SMC	-1.16	6.8	39.2	0.21	5.29	4.44		
NGC 0362	MW	-1.26	11.5	49.2	0.15	5.6	4.82		
NGC 0416	SMC	-1.22	6	15.43	0.39	5.22	4.85		
NGC 0419	SMC	-0.77	1.45	27.78	0.31	5.17	4.85		
NGC 1261	MW	-1.27	11.5	40.8	0.03	5.35	4.41		
NGC 1783	LMC	-0.35	1.7	60.6	0.02	4.95	3.84		
NGC 1786	LMC	-1.76	12.3	13.95	0.39	5.58	5.3		
NGC 1846	LMC	-0.5	1.7	34.5	0.08	4.86	4.08		
NGC 1850	LMC	-0.4	0.093	46.3	0.32	5.1	4.39		
NGC 1851	MW	-1.18	11	30.6	0.06	5.56	5.02	N ^f	
NGC 1856	LMC	-0.3	0.281	31.96	0.71	5.17	4.63		
NGC 1866	LMC	-0.43	0.177	42.91	0.4	5.07	4.39		
NGC 1868	LMC	-0.39	1.1	13.66	0.41	4.58	4.28		
NGC 1898	LMC	-1.23	11.8	25.74	0.26	5.36	4.83		
NGC 1904	MW	-1.6	13	39	0.03	5.37	4.63		
NGC 1916	LMC	-1.48	12.9	8.06	0.58	5.78	5.59		
NGC 1978	LMC	-0.38	1.9	39.53	0.21	5.12	4.62		
NGC 2004	LMC	-0.58	0.02	21.71	0.36	4.32	3.83		
NGC 2019	LMC	-1.37	12.5	9.72	0.43	5.49	5.29		

8. APPENDIX

Name	Galaxy	[Fe/H] dex	Age Gyr	Rad_h arcsec	A_V Mag	M(GC) M \odot	M (field) M \odot	[α /Fe]	MPs Y/N
NGC 2100	LMC	-0.42	0.021	18.14	0.65	4.4	4.03	-0.06 ^d	
NGC 2136	LMC	-0.4	0.1	14.08	0.59	4.36	4.04		
NGC 2808	MW	-1.14	11.5	48	0.67	5.99	5.18	0.24 ^c ± 0.03	
NGC 3201	MW	-1.59	12	186	0.73	5.21	3.6	0.22 ^c ± 0.03	
NGC 4147	MW	-1.8	12.75	28.8	0.06	4.7	4.16		
NGC 4590	MW	-2.23	13	90.6	0.15	5.18	3.69	0.19 ^c ± 0.05	
NGC 4833	MW	-1.85	13	144.6	0.98	5.5	3.82		
NGC 5024	MW	-2.1	13.25	78.6	0.06	5.71	4.65		
NGC 5139	MW	-1.53	11	300	0.37	6.33	4.05	~ 0.2 ^e	
NGC 5272	MW	-1.5	12.5	138.6	0.03	5.78	4.45		
NGC 5286	MW	-1.69	13	43.8	0.73	5.73	4.93		
NGC 5634	MW	-1.88	13	51.6	0.15	5.31	4.52	0.20 ^c ± 0.04	
NGC 5694	MW	-1.98	13.6	24	0.27	5.36	4.92	0.17 ^c ± 0.04	
NGC 5824	MW	-1.91	13	27	0.4	5.77	5.42	0.24 ^c ± 0.03	
NGC 5904	MW	-1.29	12.25	106.2	0.09	5.75	4.42	0.24 ^c ± 0.04	
NGC 5927	MW	-0.49	12.25	66	1.37	5.35	4.66	0.30 ^c ± 0.04	
NGC 5986	MW	-1.59	13.25	58.8	0.86	5.61	4.42		
NGC 6093	MW	-1.75	13.5	36.6	0.55	5.52	4.9		
NGC 6121	MW	-1.16	12.5	259.8	1.07	5.11	3.63	0.27 ^c ± 0.04	
NGC 6139	MW	-1.65		51	2.29	5.57	4.84		
NGC 6171	MW	-1.02	12.75	103.8	1.01	5.08	3.57	0.20 ^c ± 0.14	
NGC 6218	MW	-1.37	13.25	106.2	0.58	5.15	3.48		
NGC 6254	MW	-1.56	13	117	0.86	5.22	3.71	0.21 ^c ± 0.03	
NGC 6266	MW	-1.18	12.5	55.2	1.44	5.9	5.12		
NGC 6273	MW	-1.74	13.2	79.2	1.16	5.88	4.75		
NGC 6284	MW	-1.26	12	39.6	0.86	5.41	4.6	0.27 ^c ± 0.04	
NGC 6293	MW	-1.99	13	53.4	1.1	5.34	4.38		
NGC 6304	MW	-0.45	12.75	85.2	1.65	5.15	4.15		
NGC 6316	MW	-0.45		39	1.65	5.57	4.55	0.30 ^c ± 0.03	
NGC 6333	MW	-1.77		57.6	1.16	5.41	4.41		
NGC 6342	MW	-0.55	12.5	43.8	1.4	4.8	3.9		
NGC 6352	MW	-0.64	13	123	0.67	4.82	3.64	0.30 ^c ± 0.02	
NGC 6356	MW	-0.4	12.75	48.6	0.86	5.63	4.86	0.30 ^c ± 0.02	
NGC 6362	MW	-0.99	12.5	123	0.27	5.01	3.32		
NGC 6388	MW	-0.55	11.75	31.2	1.13	5.99	5.34		
NGC 6397	MW	-2.02	13.5	174	0.55	4.89	3.12	0.23 ^c ± 0.03	
NGC 6440	MW	-0.36		28.8	3.27	5.73	5.09	0.31 ^c ± 0.03	
NGC 6441	MW	-0.46	12	34.2	1.44	6.08	5.46	0.26 ^c ± 0.04	
NGC 6522	MW	-1.34	12.4	60	1.47	5.29	4.2		
NGC 6528	MW	-0.11	11	22.8	1.65	4.86	4.44	0.26 ^c ± 0.05	

Name	Galaxy	[Fe/H] dex	Age Gyr	Rad_h arcsec	A_V Mag	M(GC) M \odot	M (field) M \odot	$[\alpha/\text{Fe}]$	MPs Y/N
NGC 6541	MW	-1.81	13.25	63.6	0.43	5.64	4.56		
NGC 6553	MW	-0.18	11	61.8	1.92	5.34	4.18	0.30 ^c ± 0.02	
NGC 6569	MW	-0.76		48	1.62	5.54	4.49	0.29 ^c ± 0.03	
NGC 6584	MW	-1.5	12.25	43.8	0.31	5.31	4.31		
NGC 6624	MW	-0.44	13	49.2	0.86	5.23	4.38		
NGC 6637	MW	-0.64	12.5	50.4	0.55	5.29	4.43		
NGC 6652	MW	-0.81	13.25	28.8	0.27	4.89	4.26		
NGC 6656	MW	-1.7	13.5	201.6	1.04	5.63	3.64	0.22 ^c ± 0.02	
NGC 6681	MW	-1.62	13	42.6	0.21	5.08	4.29		
NGC 6715	MW	-1.49	13.25	49.2	0.46	6.22	5.67		
NGC 6717	MW	-1.26	13	40.8	0.67	4.49	3.76		
NGC 6723	MW	-1.1	12.75	91.8	0.15	5.36	3.86		
NGC 6752	MW	-1.54	12.5	114.6	0.12	5.32	4.11	0.22 ^c ± 0.05	
NGC 6809	MW	-1.94	13.5	169.8	0.24	5.26	3.02		
NGC 6838	MW	-0.78	12.5	100.2	0.76	4.47	2.69	0.29 ^c ± 0.03	
NGC 6864	MW	-1.29	11.25	27.6	0.49	5.66	5.16	0.22 ^c ± 0.03	
NGC 6934	MW	-1.47	12	41.4	0.31	5.21	4.5		
NGC 7006	MW	-1.52	12.25	26.4	0.15	5.3	4.67	0.25 ^c ± 0.05	
NGC 7078	MW	-2.37	13.25	60	0.31	5.91	5.24	0.24 ^c ± 0.03	
NGC 7089	MW	-1.65	12.5	63.6	0.18	5.84	4.91		
NGC 7099	MW	-2.27	13.25	61.8	0.09	5.21	4.05		

End of Table

Table 8.2 is a table of the globular clusters used from the WAGGS database. Metallicity, age and other structural parameters have been obtained from the supplementary files of Usher et al. (2019). $[\alpha/\text{Fe}]$ information has also been collected for many of the clusters and all of the clusters are assumed to possess multiple populations except for those listed as “N” or “?” (for no multiple populations or unclear respectively). Other sources are $a =$ de Boer and Fraser (2016), $b =$ Milone et al. (2019), $c =$ Dias et al. (2016), $d =$ Colucci et al. (2012), $e =$ Anguiano et al. (2015), $f =$ Milone et al. (2018a). Errors are provided when available. In the Table each GC has its name, host galaxy, its metallicity (in ‘[Fe/H]’), its age and its effective radius in arcseconds ‘Rad_h’, its V band extinction ‘A_V’, the mass of the cluster ‘M (GC)’ and the mass of the cluster in the field of the WiFeS spectrograph ‘M (field)’. It should be noted as long as any of the clusters had a paper suggesting the presence of multiple populations (be it a split main sequence or multiple MSTOs) it was classified as possessing multiple populations.

Table 8.3: Table of LICK Indices.

Name	Index units	Min Å	Max Å	Min blue Å	Max blue Å	Min red Å	Max red Å
CN ₁	Mag	4142.125	4177.125	4080.125	4117.625	4244.125	4284.125
CN ₂	Mag	4142.125	4177.125	4083.875	4096.375	4244.125	4284.125
Ca1 _{LB13}	EW	8484.000	8513.000	8474.000	8484.000	8563.000	8577.000
Ca2 _{LB13}	EW	8522.000	8562.000	8474.000	8484.000	8563.000	8577.000
Ca3 _{LB13}	EW	8642.000	8682.000	8619.000	8642.000	8700.000	8725.000
Ca4227	EW	4222.250	4234.750	4211.000	4219.750	4241.000	4251.000
Ca4455	EW	4452.125	4474.625	4445.875	4454.625	4477.125	4492.125
CaH	EW	6775.000	6817.000	6520.000	6545.000	7035.000	7050.000
CaHK _{LB13}	EW	3899.470	4003.470	3806.500	3833.820	4020.690	4052.360
CaH ₁	Mag	6357.500	6401.750	6342.125	6356.500	6408.500	6429.750
CaH ₂	Mag	6775.000	6900.000	6510.000	6539.250	7017.000	7064.000
Fe4383	EW	4369.125	4420.375	4359.125	4370.375	4442.875	4455.375
Fe4531	EW	4514.250	4559.250	4504.250	4514.250	4560.500	4579.250
Fe4668	EW	4634.000	4720.250	4611.500	4630.250	4742.750	4756.500
Fe5015	EW	4977.750	5054.000	4946.500	4977.750	5054.000	5065.250
Fe5270	EW	5245.650	5285.650	5233.150	5248.150	5285.650	5318.150
Fe5335	EW	5312.125	5352.125	5304.625	5315.875	5353.375	5363.375
Fe5406	EW	5387.500	5415.000	5376.250	5387.500	5415.000	5425.000
Fe5709	EW	5696.625	5720.375	5672.875	5696.625	5722.875	5736.625
Fe5782	EW	5776.625	5796.625	5765.375	5775.375	5797.875	5811.625
G4300	EW	4281.375	4316.375	4266.375	4282.625	4318.875	4335.125
H β	EW	4847.875	4876.625	4827.875	4847.875	4876.625	4891.625
H β 0	EW	4839.275	4877.097	4821.175	4838.404	4897.445	4915.845
H β EW	EW	4847.875	4876.625	4799.000	4839.000	4886.000	4926.000
H δ EW	EW	4083.500	4122.250	4017.000	4057.000	4153.000	4193.000
H δ _A	EW	4083.500	4122.250	4041.600	4079.750	4128.500	4161.000
H δ _F	EW	4091.000	4112.250	4057.250	4088.500	4114.750	4137.250
H γ EW	EW	4319.750	4363.500	4242.000	4282.000	4404.000	4444.000
H γ _A	EW	4319.750	4363.500	4283.500	4319.750	4367.250	4419.750
H γ _F	EW	4331.250	4352.250	4283.500	4319.750	4354.750	4384.750
Mg4780	EW	4760.780	4798.800	4738.910	4757.310	4819.780	4835.510
Mg ₁	Mag	5069.125	5134.125	4895.125	4957.625	5301.125	5366.125
Mg ₂	Mag	5154.125	5196.625	4895.125	4957.625	5301.125	5366.125
Mg _b	EW	5160.125	5192.625	5142.625	5161.375	5191.375	5206.375
NaI	EW	8163.500	8229.125	8140.000	8163.500	8230.250	8250.000
NaI _{F13}	EW	8180.000	8200.000	8137.000	8147.000	8233.000	8244.000
NaI _{LB13}	EW	8180.000	8200.000	8143.000	8153.000	8233.000	8244.000
NaI _{V12}	EW	8180.000	8200.000	8164.000	8173.000	8233.000	8244.000
NaD	EW	5876.875	5909.375	5860.625	5875.625	5922.125	5948.125
OII EW	EW	3716.300	3738.300	3696.300	3716.300	3738.300	3758.300
TiO2SDSS _{LB13}	Mag	6189.625	6272.125	6066.625	6141.625	6442.000	6455.000
TiO3	EW	6600.000	6723.000	6520.000	6545.000	7035.000	7050.000
TiOCaH	EW	6600.000	6817.000	6520.000	6545.000	7035.000	7050.000
TiO ₁	Mag	5936.625	5994.125	5816.625	5849.125	6038.625	6103.625
TiO ₂	Mag	6189.625	6272.125	6066.625	6141.625	6372.625	6415.125
TiO ₃	Mag	7123.750	7162.500	7017.000	7064.000	7234.000	7269.000
TiO ₄	Mag	7643.250	7717.250	7527.000	7577.750	7735.500	7782.750
aTiO	Mag	5445.000	5600.000	5420.000	5442.000	5630.000	5655.000
bTiO	EW	4758.500	4800.000	4742.750	4756.500	4827.875	4847.875